



**THESIS APPROVAL**  
**GRADUATE SCHOOL, KASETSART UNIVERSITY**

\_\_\_\_\_  
Doctor of Engineering (Chemical Engineering)

**DEGREE**

\_\_\_\_\_  
Chemical Engineering

\_\_\_\_\_  
Chemical Engineering

**FIELD**

**DEPARTMENT**

**TITLE:** Synthesis of Carbon Nanotube-mesoporous Silica Composites for  
Hydrocarbon Conversion

**NAME:** Miss Waleeporn Donphai

**THIS THESIS HAS BEEN ACCEPTED BY**

\_\_\_\_\_  
**THESIS ADVISOR**

( Associate Professor Metta Chareonpanich, D.Eng. )

\_\_\_\_\_  
**THESIS CO-ADVISOR**

( Associate Professor Paisan Kongkachuichay, Ph.D. )

\_\_\_\_\_  
**DEPARTMENT HEAD**

( Associate Professor Apinya Duangchan, Ph.D. )

**APPROVED BY THE GRADUATE SCHOOL ON** \_\_\_\_\_

\_\_\_\_\_  
**DEAN**

( Associate Professor Gunjana Theeragool, D.Agr. )

THESIS

SYNTHESIS OF CARBON NANOTUBE-MESOPOROUS SILICA  
COMPOSITES FOR HYDROCARBON CONVERSION



WALEEPORN DONPHAI

A Thesis Submitted in Partial Fulfillment of  
the Requirements for the Degree of  
Doctor of Engineering (Chemical Engineering)  
Graduate School, Kasetsart University  
2014

Waleeporn Donphai 2014: Synthesis of Carbon Nanotube-mesoporous Silica Composites for Hydrocarbon Conversion. Doctor of Engineering (Chemical Engineering), Major Field: Chemical Engineering, Department of Chemical Engineering. Thesis Advisor: Associate Professor Metta Chareonpanich, D.Eng. 134 pages.

In this research, the novel composite catalysts of nickel-carbon nanotubes (CNTs) over mesocellular silica (MS) support (Ni-CNTs/MS) and nickel-carbon nanofibers (CNFs) over mesocellular silica (MS) support (Ni-CNFs/MS) were synthesized and tested in dry reforming reaction and phenylacetylene hydrogenation reaction, respectively. Consequently, MS support was primarily prepared based on the synthesis of SBA-15 mesoporous silica with 1,3,5-trimethylbenzene (TMB) as a swelling agent. After that, nickel metal was loaded onto MS support by using an incipient-wetness impregnation method, followed by CNTs and CNFs synthesis via catalytic chemical vapor deposition (CCVD) technique through tip-growth mechanism. In dry reforming reaction, it was found that the existence of CNTs composite catalysts with nickel metal clusters on the tips of CNTs (Ni-CNTs/MS catalysts) could significantly improve the catalyst stability compared to that of Ni/MS catalyst. After 24 h time-on-stream, CO<sub>2</sub> and CH<sub>4</sub> conversions of Ni/MS catalyst were approximately 10% decreased, while those of Ni-CNTs/MS catalyst were 3% increased. This outstanding performance could be attributed to selective formation of carbon by-products as the tube-length extension of the existing CNTs. In phenylacetylene hydrogenation, Ni-CNFs/MS composite catalyst exhibited the highest TOF of which was approximately 3.2 times higher than that of Ni/MS due to the hydrophobic surface property of CNFs and unique composite structure of Ni-CNFs/MS catalyst. Moreover, the enhancement of photocatalytic performance of the composite catalyst of TiO<sub>2</sub> over different carbons types in the degradation of methylene blue was investigated. It was found that TiO<sub>2</sub>-zeolite templated carbon was more efficient photocatalyst for degradation of methylene blue than that of TiO<sub>2</sub>-activated carbon due to its large surface area, pore volume and hydrophobic surface property.

---

Student's signature

Thesis Advisor's signature

## ACKNOWLEDGEMENTS

I would like to take this opportunity to acknowledge many people who help me complete this work. My sincere gratitude first goes to my thesis advisor Associate Professor Dr. Metta Chareonpanich, for her consistent and thoughtful advice, continuous encouragement and help during the course of this work. I am grateful to my graduate committees; Associate Professor Dr. Paisan Kongkachuichay and Assistant Professor Dr. Thongthai Witoon for their kindly giving the time to advice, revise and approve my thesis.

I would like to thank Professor Dr. Hiromi Yamashita and Assistant Professor Dr. Takashi Kamegawa who gave me a warm welcome at Division of Materials and Manufacturing Science, Graduate School of Engineering, Osaka University. Their suggestions on research work are sincerely acknowledged.

I gratefully acknowledge the financial support from the Thailand Research Fund (TRF) under the Royal Golden Jubilee Ph.D. Program (Grant No. PHD/0063/2551) cooperated with Kasetsart University. This work was supported in part by grants from the 2009 NSTDA Chair Professor funded by the Crown Property Bureau under the management of the National Science and Technology Development Agency (NSTDA), the Commission of Higher Education, Ministry of Education under Postgraduate Education and Research Programs in Petroleum, Petrochemicals and Advanced Materials, the National Nanotechnology Center under NSTDA, and the Kasetsart University Research and Development Institute (KURDI).

Finally, I would like to thank my family for their love, support, encouragement, and their understanding during the whole period of my education. My family has been my greatest source of strength and inspiration. My gratefulness devotes to my family who wholeheartedly support me away.

Waleeporn Donphai

April 2014

**TABLE OF CONTENTS**

	<b>Page</b>
TABLE OF CONTENTS	i
LIST OF TABLES	ii
LIST OF FIGURES	iv
INTRODUCTION	1
OBJECTIVES	6
LITERATURE REVIEW	8
MATERIALS AND METHODS	38
RESULTS AND DISCUSSION	56
CONCLUSION AND RECOMMENDATIONS	105
Conclusion	105
Recommendations	107
LITERATURE CITED	108
APPENDICES	124
Appendix A Qualitative and quantitative results from gas chromatography	125
Appendix B Conversion results	129
Appendix C CO chemisorption	131
CIRRICULUM VITAE	133

## LIST OF TABLES

<b>Table</b>		<b>Page</b>
1	Various mesoporous silica products based on 2D hexagonal structure	12
2	Physicochemical properties of mesoporous silica synthesized with different pH values of mixture	14
3	Physicochemical properties of mesoporous silica synthesized with different TEOS and TMOS molar ratios	15
4	Pore characteristics of mesoporous silica prepared with different aromatic swelling agents	16
5	Carbon deposit, average outer and inner diameters, and wall thickness of different carbon samples	21
6	Methane conversions with different non-noble metals loaded on silica support	28
7	CH <sub>4</sub> conversions with different supports.	29
8	Sequences of TMB addition in SBA-15 synthesis	41
9	Physical properties of SBA-15 mesoporous silica and mesocellular silica with different Pluronic P123 to TMB ratios	58
10	Physical properties of SBA-15 mesoporous silica and mesocellular silica with different sequences of TMB addition	62
11	Textural properties of catalysts without and with CNTs composite, and amount of carbon on fresh catalysts	67
12	Nickel metal size of catalyst after dry reforming reaction	78
13	BET surface area, pore volume and average nickel metal size of catalysts	88
14	Amount of carbon, hydrophobicity, product selectivities, and turnover frequency (TOF) of catalysts in phenylacetylene hydrogenation	92

**LIST OF TABLES (Continued)**

<b>Table</b>		<b>Page</b>
15	Physical properties of TiO <sub>2</sub> composite catalysts with different carbon supports	99
<b>Appendix Table</b>		
A1	Equation of calibration curves for standard gas	128

## LIST OF FIGURES

Figure		Page
1	Scheme of micelle formed (a) oil-in-water micelle and (b) water-in-oil micelle	10
2	Schematic of micelle structures (a) sphere, (b) rod and cylindrical, and (c) lamellar	10
3	Three initial stages of SBA-15 synthesis.	13
4	Aromatic molecules used as swelling agents	16
5	Schematic of the pore size modification by using TMB	17
6	High-resolution transmission electron microscopy and schematic representative showing the structural relationship between the catalyst particle and precipitated graphite platelets formed of (a) carbon nanotube and (b) carbon nanofibers	18
7	Schematic of tip-growth mechanism	19
8	Schematic of base-growth mechanism	19
9	TEM images of CNTs with different synthesis temperatures: (a) 550°C, (b) 650°C, (c) 900°C and (d) SWCNTs at 990°C.	22
10	Schematic of the formation of (a) full carbon nanofiber and (b) hollow carbon nanofiber.	23
11	TEM images of SBA-15– 2 % CNTs composites with different CNTs addition times	24
12	Pathway of phenylacetylene hydrogenation	32
13	Schematic representation of the mechanism of photocatalytic activity (photochemical activation and electron-hole formation)	35
14	Chemical structure of methylene blue dye	36
15	Proposed organic compound decomposition pathway by photocatalytic reaction system	37

## LIST OF FIGURES (Continued)

Figure		Page
16	Schematic diagram of SBA-15 synthesis process	40
17	Catalytic reaction testing unit: (a) a feed flow measuring and controlling system, (b) a furnace-equipped stainless steel tube reactor and (c) a sampling system	48
18	Mass flow controller: (a) Aalborg GFC thermal mass flow controller and (b) KOFLOC mass flow controller and mass flow meter with indicator	49
19	Tube reactor equipped with the electric heater (Carbolite tube furnace)	49
20	Schematic setup of pack-bed reactor	50
21	(A) Nitrogen adsorption-desorption isotherm and (B) pore size distribution of MS support and catalysts	58
22	TEM images of SBA-15 mesoporous silica and mesocellular silica with different Pluronic P123 to TMB ratios	59
23	Expansion of Pluronic P123 micelle with TMB as a swelling agent	59
24	Nitrogen adsorption-desorption isotherm of mesocellular silica with different sequences of TMB addition	60
25	Pore size distribution of mesocellular silica with different sequences of TMB addition	61
26	TEM images of mesocellular silica with different sequences of TMB addition	64
27	(A) Nitrogen adsorption-desorption isotherm and (B) pore size distribution of MS support and catalysts	66

## LIST OF FIGURES (Continued)

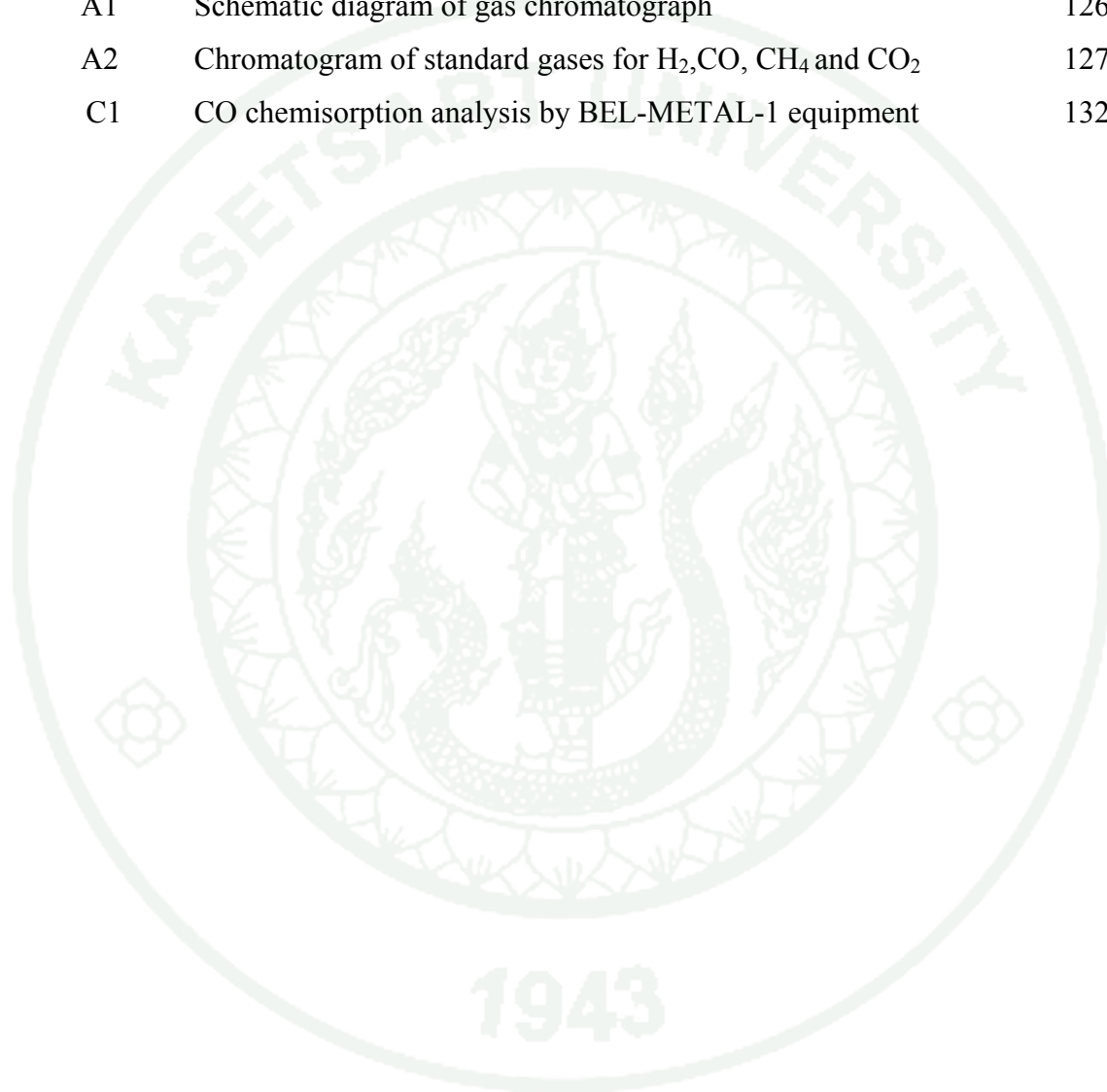
Figure		Page
28	XRD patterns of fresh catalysts	68
29	FE-SEM images of fresh CNTs composite catalysts	68
30	TGA-DTA curves of fresh CNTs composite catalysts	70
31	Raman spectra of fresh CNTs composite catalysts	70
32	Performances of catalysts without and with CNTs composite with time on stream in dry reforming reaction at 650°C for 24 h.(a) CH <sub>4</sub> conversion, (b) CO <sub>2</sub> conversion, (c) H <sub>2</sub> /CO mole ratio	73
33	(A) TGA-DTA curves of unreduced (dashed line) and reduced (solid line) catalysts and (B) FE-SEM images of reduced CNTs composite catalysts	74
34	Performances of unreduced and reduced CNTs composite catalysts with time on stream in dry reforming reaction at 650°C for 24 h.(a) CH <sub>4</sub> conversion, (b) CO <sub>2</sub> conversion, (c) H <sub>2</sub> /CO mole ratio	76
35	XRD patterns of catalysts after dry reforming reaction at 650°C for 24 h	77
36	TGA-DTA curves of catalysts after dry reforming at 650°C for 24 h	79
37	Raman spectra of catalysts after dry reforming at 650°C for 24 h	81
38	FE-SEM images of catalysts after dry reforming at 650°C for 24h	82
39	TEM images of catalysts before and after dry reforming at 650°C for 24 h	84
40	Proposed schemes of different carbon formation mechanisms during dry reforming reaction leading to (a) deactivation of Ni/MS catalysts by coke deposition (b) prolonging stability of Ni-CNTs/MS catalysts by selective extension of CNT tube length	86

**LIST OF FIGURES (Continued)**

<b>Figure</b>		<b>Page</b>
41	(A) Nitrogen adsorption-desorption isotherm and (B) pore size distribution of mesoporous silica support and catalysts	88
42	XRD patterns of fresh catalysts after reduced with H <sub>2</sub> gas at 500°C	89
43	Weight loss of fresh catalysts	90
44	Raman spectra of fresh catalysts	90
45	TEM images of fresh catalysts	91
46	The reaction-time profiles of phenylacetylene hydrogenation over different catalysts	94
47	(A) TEM images (a, b) and (B) proposed schemes of surface reaction of phenylacetylene hydrogenation (c, d) over Ni/MS and Ni-CNFs/MS catalysts	97
48	(A) Nitrogen adsorption-desorption isotherm and (B) pore size distribution of catalysts	99
49	TEM images of TiO <sub>2</sub> composite catalysts	100
50	Adsorption isotherm of MB over different carbon supports after 30 min under dark condition	101
51	Photographs of MB adsorption of different carbon supports under dark condition after 30 min	101
52	Photocatalytic activities of TiO <sub>2</sub> composite catalysts with different carbon supports for photodegradation of methylene blue at 24-h reaction time	103
53	XRD patterns of catalysts	103

**LIST OF FIGURES (Continued)**

<b>Appendix Figure</b>		<b>Page</b>
A1	Schematic diagram of gas chromatograph	126
A2	Chromatogram of standard gases for H <sub>2</sub> , CO, CH <sub>4</sub> and CO <sub>2</sub>	127
C1	CO chemisorption analysis by BEL-METAL-1 equipment	132



# **SYNTHESIS OF CARBON NANOTUBE-MESOPOROUS SILICA COMPOSITES FOR HYDROCARBON CONVERSION**

## **INTRODUCTION**

Mesoporous silica is an outstanding material among porous silica because of its excellent properties, i.e., high specific surface area, high thermal stability and high mechanical stiffness. Therefore, mesoporous silica has been applied in many industrial processes as adsorbents, catalysts and catalyst supports. SBA-15 mesoporous silica is an excellent example of mesoporous silica that can be concisely controlled the pore size and pore characteristics. As the pore shape and size of catalysts directly affect the diffusion of reactant gas and the product selectivities, it is therefore necessary in the catalytic application to precisely control pore shape and pore size of catalysts. Accordingly, several techniques have been used to control the pore size of the catalysts, especially for SBA-15 mesoporous silica. One of the frequently used technique is the use of swelling agents including 1,3,5-trimethylbenzene (TMB), 2,3,4-trimethylpentane (TMP), tetrahexylammonium bromide (THB) and N,N-dimethyldecylamine (DMD) to expand the pore size of this support (Schmidt-Winkel *et al.*, 1999; Lettow *et al.*, 2000; Luechinger *et al.*, 2005).

Carbon nanotubes (CNTs) and carbon nanofibers (CNFs) also have excellent properties as catalyst supports. Their unique structural properties and interaction between support and metal particle, uniform pore-size distribution, large surface area (Fidalgo *et al.*, 2011; Li *et al.*, 2012), and high surface hydrophobicity (He *et al.*, 2013) are of interest. Due to these unique properties, they are therefore attractive for the use as catalyst supports (Tavasoli *et al.*, 2009). CNTs and CNFs are graphitic filaments but with different filament structures. The structure of CNTs is tubular graphene walls aligned parallel to the filament axis, whereas that of CNFs is the stacked and herring bone forms of graphitic filaments. CNTs and CNFs can be synthesized by using different techniques including arc-discharge, laser ablation, and catalytic chemical vapor deposition (CCVD) (Harris 2009). Among these techniques,

CCVD technique is the most common method for CNTs and CNFs productions, which can synthesize CNTs and CNFs on support contained metal on the tip of nanotubes or nanofibers (Jong *et al.*, 2000; Harris 2009). However, CNTs are synthesized at higher temperature than that of CNFs, consequently the higher thermal stability compared to that of CNFs is obtained. Accordingly, in this research the combination of metal and CNTs or CNFs over mesoporous silica as the composite material are applied as the catalysts in various hydrocarbon reactions. Based on the appropriate carbon types to the reaction temperature; metal-CNTs composite catalyst is used in reforming (high temperature), while metal-CNFs composite catalyst is used in hydrogenation (low temperature) reactions.

Over the past two decade, dry reforming reaction has been an increasing interest reaction because it can reduce carbon dioxide (CO<sub>2</sub>) and methane (CH<sub>4</sub>) played a major role in global warming effect. Nowadays, CO<sub>2</sub> and CH<sub>4</sub> continuously release to atmosphere by the result of industrial processes and man-made activities (Wang *et al.*, 1996; Bradford *et al.*, 2007; Fan *et al.*, 2009). In this reaction, CO<sub>2</sub> and CH<sub>4</sub> are primarily converted to carbon monoxide and hydrogen (synthesis gas) of which are further converted to alcohols (methanol and ethanol) and hydrocarbon feedstock for petrochemical industries through Fischer-Tropsch synthesis reaction (Castro *et al.*, 2013; Chen *et al.*, 2013). However, several problems such as highly endothermic nature of dry reforming reaction, competitiveness among many side reactions, sintering of catalysts, and carbon deposition are significantly observed (Guo *et al.*, 2007; San-Jose-Alonso *et al.*, 2009). Among these, carbon deposition is concerned as a major problem because of its direct and immediate effect on the activity and selectivity of catalysts (Fan *et al.*, 2009; Prasad *et al.*, 2012).

Many researchers have attempted to diminish carbon formation and enhance catalyst activity in dry reforming reaction by means of oxide supports and promoters. Consequently, the use of oxide catalyst support (MgO, ZrO<sub>2</sub>, and CeO<sub>2</sub>) is also one alternative for carbon mitigation (Takeguchi *et al.*, 2003; Kambolis *et al.*, 2010). The oxide catalyst support can improve CO<sub>2</sub> adsorption on oxygen-containing surfaces and reduce the amount of carbon formation through reversed Boudouard reaction to

form carbon monoxide. Moreover, the lanthanide-group metals (La, Ce, Pr and Sm) have been widely used as the catalyst promoter to increase the resistance to carbon deposition because of their highly stable oxidation states. However, the availability and cost are the main limitation of the lanthanide-group metals (Lima *et al.*, 2006; Gallego *et al.*, 2009). In this research, the use of composite catalysts with a unique structure between nickel (Ni) and carbon nanotubes (CNTs) on mesocellular silica (MS) support in dry reforming reaction were proposed with an attempt to improve the catalyst stability in dry reforming reaction.

Due to the fact that hydrogenation reaction is one of important reactions in petrochemical industry since it can eliminate a hazardous chemical impurity such as phenylacetylene in styrene feedstock. Phenylacetylene plays role as the poisoning on polymerization catalysts, therefore its maximum acceptable limit of not more than 10 ppm is required (Wilhite *et al.*, 2002; Dominguez-Dominguez *et al.*, 2008; Duraczynska *et al.*, 2009). Accordingly, phenylacetylene hydrogenation is an important process in petrochemical industry as it can eliminate the certain amounts of phenylacetylene in styrene production. Phenylacetylene can be converted to styrene through the selective hydrogenation of alkyne to alkene process. Generally, hydrogenation of phenylacetylene is used as a model reaction for evaluating the performance of hydrogenation catalysts since this reaction can be operated under mild conditions (Wilhite *et al.*, 2002; Dominguez-Dominguez *et al.*, 2006; Li *et al.*, 2012).

Since hydrogenation of phenylacetylene is carried out in liquid phase system, the limitation of reactant diffusion is therefore a major problem in the conventional catalysts (Wilhite *et al.*, 2002; Na-Chiangmai *et al.*, 2011). With an attempt to overcome the diffusion limitation of phenylacetylene, the catalysts with a unique composite structure between nickel (Ni) and carbon nanofibers (CNFs) on mesocellular silica (MS) support have been applied. As MS support provided large surface area and high metal dispersion, while Ni metal was a promising active catalyst due to its low cost, availability and high performance in this reaction (Bautista *et al.*, 1998; Relvas *et al.*, 2008), nickel metal over silica support was consequently applied as the main catalyst in this study. In addition, carbon nanofibers (CNFs) are attractive

for the use as the dual support due to their unique surface properties, i.e., resistance to strong acid and base, hydrophobic surface property and better hydrogen diffusion on carbon-grain boundary, leading to better catalyst performance (Nhut *et al.*, 2003; Jahjah *et al.*, 2010). In this work, nickel-carbon nanofibers composites prepared by CCVD method via tip-growth mechanism on mesocellular silica (Ni-CNFs/MS) were used as the catalyst for liquid-phase phenylacetylene hydrogenation. Their performances were examined and compared to the conventional nickel over mesocellular silica (Ni/ MS) catalyst.

Moreover, carbon composite materials can also apply as the catalyst in photocatalytic reaction. This reaction has been interested for removal of organic compound and dye molecules under light condition as the pollutant-cleaning process. TiO<sub>2</sub> nanoparticles are a well-known semiconductor material used as catalysts in photocatalytic reaction due to their advantage properties including suitable band gap energy, high stability, nontoxicity, and availability (Kamat 1993; Fujishima *et al.*, 2000; Nakata *et al.*, 2012). The photocatalysis reaction almost operates under higher concentration environments of dilute organic compounds or dyes molecules. Therefore, the limitation of organic compound adsorption and recombination of electron-hole pairs are drawback factors of TiO<sub>2</sub>-based photocatalysts in photodegradation of organic compounds (Xu *et al.*, 2010; Chen *et al.*, 2012). In order to overcome these problems, carbon-based materials are concerned as the potential candidate for enhancement of photocatalytic efficiency due to their multifunctional properties such as large surface area, better electron transfer property on carbon surface, and greater surface hydrophobicity (Kamegawa 2010; Xu *et al.*, 2010). Various types of carbon materials such as activated carbon (AC), carbon nanotubes (CNTs), and graphene have been incorporated into TiO<sub>2</sub> for the use as the composite catalyst in photocatalytic reaction. However, the weakening of light intensity arriving at catalyst surface still hinders further promotion of efficiency of TiO<sub>2</sub>-carbon catalysts (Zhang *et al.*, 2010). In this research, a new-structure carbon material, zeolite templated carbon (ZTC) prepared by using zeolite Y as a template for a tailored micropore structure, resulting in ordered microporous carbon with sp<sup>2</sup>-carbon hybridization and very high surface area (~4,000 m<sup>2</sup>/g) has been examined in

photocatalytic reaction. Additionally, ZTC structure composes of buckyowl-like nanographenes of 3-dimensional carbon network and oxygen-containing functional groups (Ma *et al.*, 2000; Nishihara *et al.*, 2009). According to these unique properties, ZTC is of excellence for the use as photocatalyst supports.



## OBJECTIVES

1. To prepare mesocellular silica by expanding the pore sizes of SBA-15 mesoporous silica using 1,3,5- trimethylbenzene as the swelling agent.
2. To synthesize nickel-carbon nanotubes and nickel-carbon nanofibers composites over mesoporous silica via catalytic chemical vapor deposition (CCVD) method.
3. To examine the effect of nickel-carbon nanotubes composites over mesoporous silica on dry reforming reaction.
4. To examine the effect of nickel-carbon nanofibers composites over mesoporous silica on phenylacetylene hydrogenation reaction.
5. To synthesis  $\text{TiO}_2$ -carbon composite catalysts and tested in photocatalytic reaction.

## Benefits

1. Nickel-carbon nanotubes and nickel-carbon nanofibers composites over mesoporous silica could be successfully synthesized with the unique structure of nickel on the tip of nanotubes or nanofibers by catalytic chemical vapor deposition (CCVD) method.
2. Better catalytic stability of nickel-carbon nanotubes over mesocellular silica composite catalyst than that of conventional nickel over mesocellular silica catalyst were achieved in dry reforming reaction.
3. High catalytic performance of nickel-carbon nanofibers composites over mesoporous silica in phenylacetylene hydrogenation was obtained.

4. Photocatalytic performance of TiO<sub>2</sub>-carbon composite catalyst in the degradation of methylene blue could be accomplished.



## LITERATURE REVIEW

In this research, we focused on the synthesis of novel materials having mesoporous structure as the main skeleton, and microporous structure (carbon nanotubes (CNTs) and carbon nanofibers (CNFs)) on the main skeleton via the catalytic chemical vapor deposition (CCVD) method. This composite material was applied as the catalysts in C1 conversion and liquid-phase hydrogenation reaction. Moreover, the other composite materials between carbon and titanium dioxide (TiO<sub>2</sub>) was synthesized and tested in photocatalytic reaction. The background of this research has categorized into three parts including (1) the synthesis of mesoporous silica and CNT composite, (2) the related catalytic reactions including carbon dioxide reforming of methane and liquid-phase hydrogenation reaction, and (3) photocatalysis of dye degradation. The details of research background were explained below.

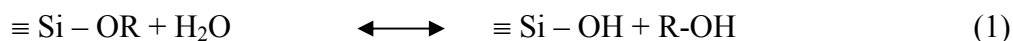
### 1. Synthesis of mesoporous silica-CNTs composites

#### 1.1 Synthesis of mesoporous silica

##### 1.1.1 Chemistry of sol-gel process

The sol-gel process is a useful process for porous silica synthesis. By using this technique, water and low molecular weight alkoxide was used as the precursors. Several kinds of low molecular weight alkoxides such as sodium silicate or tetraethoxysilane (Si(OC<sub>2</sub>H<sub>5</sub>)<sub>4</sub>; TEOS) can be used as the silica precursors. The alkoxide can be hydrolyzed with water and formed silanol groups ( $\equiv\text{Si}-\text{OH}$ ), where either acid or base is used as the catalyst. This process normally occurs through a two-step mechanism, involving hydrolysis of an alkoxide precursor (formation of the sol) and the subsequent condensation of hydroxyl or alkoxy groups (formation of the gel), as shown in Equations 1-3, respectively.

Hydrolysis reaction



Alcohol condensation (silanol-ester condensation)



Water condensation (silanol-silanol condensation)



The formation of porous silica can be consecutively taken place in three steps: (1) polymerization of monomer ( $\text{Si}(\text{OH})_4$ ) to form particles, (2) growth of particles, and (3) linking of particles into branched chains, networks, extending throughout the liquid medium, and then thickening to a gel (Iler, 1979).

### 1.1.2 Micelle mesostructure

A micelle is an aggregation of surfactant molecules dispersed in liquid colloid. A typical micelle in aqueous solution can form an aggregation with the hydrophilic head regions in contact with surrounding solvent and the hydrophobic tail regions in the micelle center. Generally micelle phase is oil-in-water micelle as shown in Figure 1a. In some case, micelle phase is changed to the form of water-in-oil (reverse micelle) which has the head groups at the center and the tails extending out, as shown in Figure 1b. Micelle structures strongly depend on the molecular geometry of their surfactant, surfactant concentration, temperature, pH, and ionic strength. There are normally three structures of micelle including sphere, cylindrical and lamellar, as shown in Figure 2.

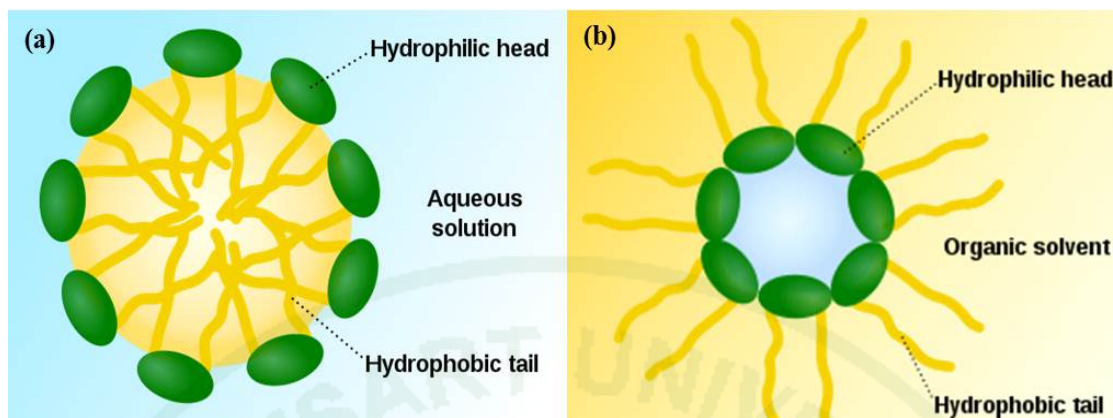


**Figure 1** Scheme of micelle formed (a) oil-in-water micelle and (b) water-in-oil micelle.

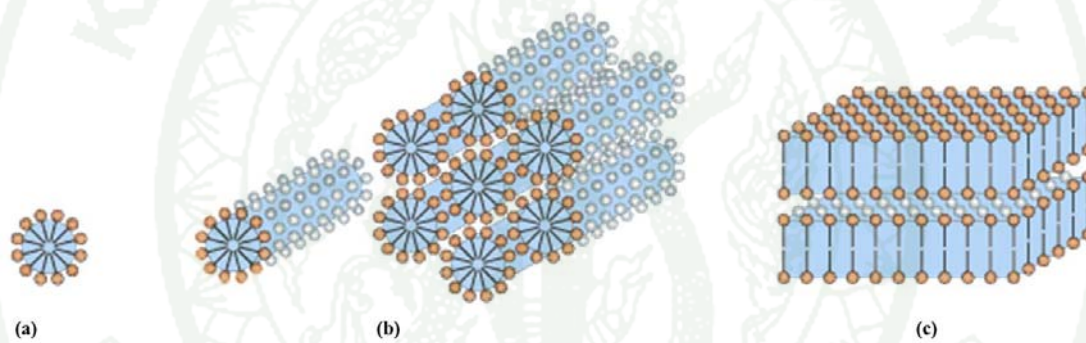


**Figure 2** Schematic of micelle structures (a) sphere, (b) rod and cylindrical, and (c) lamellar.

### 1.1.3 Mesoporous silica

Mesoporous silica is frequently used as adsorbents, catalysts and catalyst supports because of their high surface area, thermal stability and mechanical stiffness (Lee *et al.*, 2008). These mesoporous structure can be modified by manipulating types of templates, silica sources and synthesis conditions (Selvam *et al.*, 2001). The most common structure is the two-dimensional hexagonal with the P6mm symmetry, consisting of close-packed hexagonal arrays of cylindrical surfactant micelles. Table 1 shows the detail of mesoporous silica products obtained with various synthesis conditions.

For the synthesis of periodic mesoporous silica, a homogeneous solution is obtained by dissolving the surfactant in a solvent. Water is the most common solvent and medium. Silica precursor is then added into the solution under acidic or basic condition, after that the solution is transformed to sols of silicate oligomers. This step is called hydrolysis and condensation. These cooperative assembly and aggregation between oligomers and surfactant micelles lead to the polymerization and precipitation to form gel. Normally, mesoporous silica is rapidly formed within only 3-5 min in cationic surfactant solutions by simple precipitation. The formation of mesostructures is slow if nonionic surfactants are used as templates. It normally takes place within 30 min or even longer. In addition, types of silica sources also have effect on the mesoporous silica synthesis. In the case that tetramethoxysilane (TMOS) was used as the silica source, a faster formation of mesoporous silica structures than TEOS was observed. In comparison to TMOS and TEOS, with tetrabutoxysilane (TBOS) precursor the slower formation was obtained. This phenomenon can be attributed to their hydrolysis rates. The silica solution was after that transferred to autoclave heated in the temperature ranging between 80-150°C for hydrothermal aging, in this stage the complete formation of mesoporous silica structure was obtained. Then, the obtained product was cooled down to room temperature. The final product was filtered and washed by using deionized water, dried and calcined to remove the organic template (Ying *et al.*, 2007).

**Table 1** Various mesoporous silica products based on 2D hexagonal structure

Name	Silica source	Template	Reaction condition	References
MCM-41	Sodium silicates	Alkyltrimethyl ammonium	Hydrothermal synthesis at 100°C for 144 h	Beck <i>et al.</i>
MMS	TEOS	EO <sub>106</sub> PO <sub>70</sub> EO <sub>106</sub>	Silica/surfactant/butanol/water mixture; hydrothermal synthesis at 100°C for 24 h	Feng <i>et al.</i>
SBA-3	TEOS	Cetyltrimethyl ammonium bromide and HBr	Silica/surfactant/acid/water mixture stirrer at RT for ≥ 30 min	Huo <i>et al.</i>
SBA-15	TEOS	C <sub>16</sub> EO <sub>10</sub>	Silica/surfactant/water mixture heated at 100°C for 24 h	Huo <i>et al.</i>
FEM-16	Sodium kanemite	Cetyltrimethylamm onium chloride	Silica/surfactant/water mixture heated at 70°C with stirring; after 3 h, pH adjusted to 8.5, and mixture again heated at 70°C for 3 h	Inagaki <i>et al</i>
SBA-15	TEOS	EO <sub>20</sub> PO <sub>70</sub> EO <sub>20</sub>	Silica/surfactant/water mixture heated at 40°C for 24 h	Zhao <i>et al.</i>

**Source:** Selvam *et al.* (2001)

#### 1.1.4 SBA-15 mesoporous silica

SBA-15 has a well-ordered 2-dimensional hexagonal structure, having high surface area (600-1,000 m<sup>2</sup>/g), narrow pore size distribution, large pore volume (1-2 cm<sup>3</sup>/g) and high thermal stability. The pore diameters of SBA-15 can be

controlled in the range of 2-30 nm by simple modification using surfactants, additives and synthetic conditions (Zhao *et al.*, 2000). SBA-15 mesoporous silica became more popular material than hexagonal mesoporous silica (HMS) and MCM-41 because of its unique characteristics, i.e., thicker pore walls and higher thermal stability (Linessen *et al.*, 2003).

For the synthesis of SBA-15 mesoporous silica, the silica solution (sodium silicate, TEOS, TMOS) was added to aqueous acidic solution of the micelle surfactant (Pluronic P123, EO<sub>20</sub>PO<sub>70</sub>EO<sub>20</sub>) under stirring condition at 30-80°C. This step was considered as the hydrolysis-condensation step. After that the obtained solution was transferred to autoclave and heated at 70-140°C for 11-72 h in the polymerization step. After complete crystallization, the solid products were filtered, washed with deionized water or ethanol, dried at 140°C for 3 h, and calcined at 500°C for 6 h. Figure 3 shows the mechanistic pathways for the formation of SBA-15.

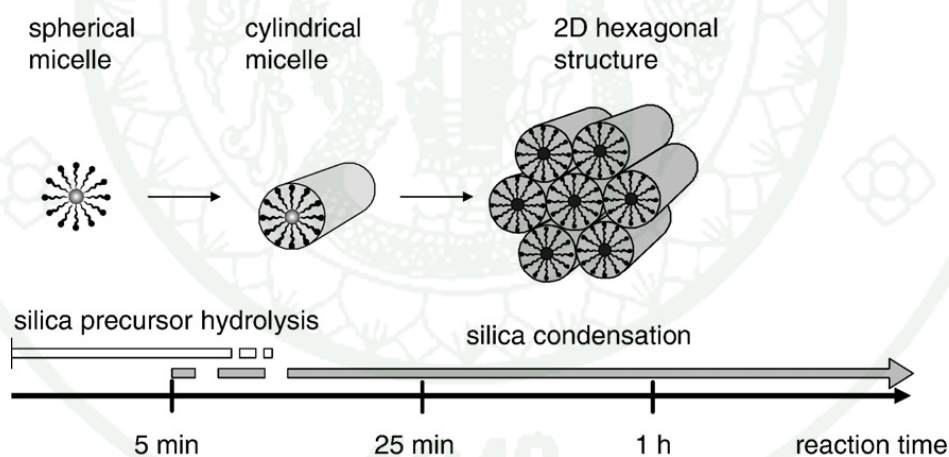


**Figure 3** Three initial stages of SBA-15 synthesis.

**Source:** Zholobenko *et al.* (2008)

### 1.2 Modification SBA-15 pore size

The modification of pore size of SBA-15 mesoporous silica can be done by tuning the synthesis variables including pH, silica source, and swelling agent.

### 1.2.1 pH

Liu *et al.* (2008) studied the influence of pH on mesoporous synthesis. They synthesized mesoporous silica by using TEOS as a silica precursor at different pH values in the range of 3.2–5.1. The results are shown in Table 2. From the result, the pore diameter of mesoporous silica strongly depended on pH values of mixture. When pH was increased, the pore diameter gradually increased.

**Table 2** Physicochemical properties of mesoporous silica synthesized with different pH values of mixture

Sample	pH	BET surface area (m <sup>2</sup> /g)	Pore diameter (nm)	Pore volume (cm <sup>3</sup> /g)
1	3.2	1004	7.1	1.7
2	3.6	924	8.1	1.5
3	4.1	767	11.3	1.6
4	4.4	576	16.0	1.6
5	5.1	336	46.0	1.9

**Source:** Liu *et al.* (2008)

### 1.2.2 Silica source

The different silica sources were applied in the synthesis of mesoporous material, resulting in different pore diameters. In this case, tetraethyl orthosilicate (TEOS) and tetramethyl orthosilicate (TMOS) were used as silica sources and the ratio of TEOS and TMOS were varied in order to modify the structure of mesoporous material (Liu *et al.*, 2008). Table 3 shows properties of mesoporous silica with different ratios of TEOS and TMOS.

**Table 3** Physicochemical properties of mesoporous silica synthesized with different TEOS and TMOS molar ratios

Sample	TEOS (mol %)	TMOS (mol %)	BET surface area (m <sup>2</sup> /g)	Pore diameter (nm)	Pore volume (cm <sup>3</sup> /g)
S1	0	100	760	9	1.17
S4	30	70	626	31	1.82
S5	50	50	666	28	1.76
S6	70	30	567	49	1.94
S7	100	0	576	16	1.62

**Source:** Liu *et al.* (2008)

### 1.2.3 Swelling agent

Many types of aromatic compounds such as benzene, 1,3,5 triisopropylbenzene (TiPB), 1,3,5-triethylbenzene (TEB), 1,3,5-tri-tert-butylbenzene (TtBB), and 1,3,5- trimethylbenzene (TMB) (Figure 4) were used as a swelling agent in order to modify the pore structure of mesoporous silica (Luechinger *et al.*, 2005). It was found that types of swelling agents have a significant effect on the structure of mesoporous material, as the result shown in Table 4. Among of aromatic compounds, 1,3,5- trimethylbenzene (TMB) was widely used to modify the pore structure of mesoporous silica (Schmidt-Winkel *et al.*, 1999; Lettow *et al.*; 2000 Zhang *et al.*, 2008).

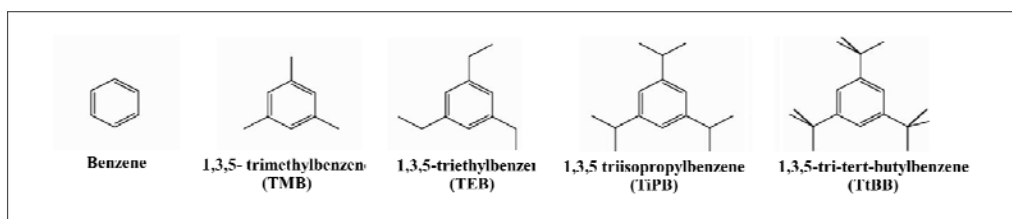


**Figure 4** Aromatic molecules used as swelling agents

**Source:** Luechinger *et al.* (2005)

**Table 4** Pore characteristics of mesoporous silica prepared with different aromatic swelling agents

Swelling agent	Average pore diameter (nm)		Total Pore volume (cm <sup>3</sup> /g)	BET surface (m <sup>2</sup> /g)
	Adsorption	Desorption		
TMB	10.0	9.7	2.65	1180
TEB	6.7	3.7	1.58	1051
TiPB	6.7	5.5	1.43	986
TtBB	4.2	4.5	1.06	995

**Source:** Luechinger *et al.* (2005)

In the process of pore size modification, TMB molecule with hydrophobic property is the preferable and selective agent for the hydrophobic poly(propylene oxide) blocks and thus swells the micelle cores, while the hydrophilic poly-(ethylene oxide) blocks are preferentially solvated by water. This phenomenon leads to the growth of the oil in water microemulsion droplets. The scheme of pore-size modification by using TMB is shown in Figure 5.



**Figure 5** Schematic of the pore size modification by using TMB

**Source:** Zhang *et al.* (2008)

### 1.3 Carbon formation

Carbon nanotubes (CNTs) and carbon nanofibers (CNFs) are graphitic filament but with different filament structures. The structure of CNTs is tubular graphene walls alligned parallel to the filament axis, whereas that of CNFs is the stacked and herring bone forms of graphitic filaments. The structures of CNTs and CNFs are shown in Figure 6 (a) and (b), respectively.

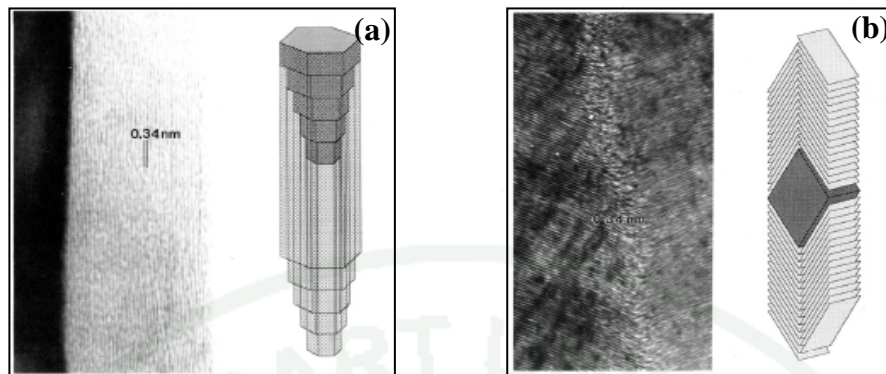


**Figure 6** High-resolution transmission electron microscopy and schematic representative showing the structural relationship between the catalyst particle and precipitated graphite platelets formed of (a) carbon nanotube and (b) carbon nanofibers

**Source:** Rodriguez *et al.* (1995)

It should be noted that, CNTs and CNFs can be synthesized via the same method as catalytic chemical vapor deposition (CCVD). In CCVD method, CNTs and CNFs are grown by carbon diffusion through metals on the support and its subsequent precipitation as graphitic filament. Moreover, it was reported that there are two mechanisms including tip-growth and base-growth mechanisms normally used to explain the formation of CNTs and CNFs due to the different interaction between metal and support, as explained below.

#### Tip-growth mechanism

The growth mechanism of metal and support with weak interaction is shown in Figure 7. Hydrocarbon was firstly decomposed on the surface of metal, while carbon radicals were simultaneously diffused through the metal, and the graphitic filament was precipitated out across at the bottom of metal and lifted up the metal, as explained in the first step. Next step, graphitic filament continuously grew longer and longer due to carbon diffusion. The growth of CNTs or CNFs was stopped when the active metal was covered by carbon.

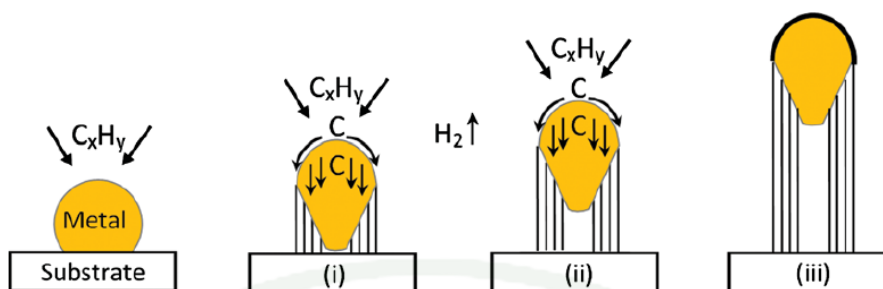


**Figure 7** Schematic of tip-growth mechanism

**Source:** Kumar and Ando (2010)

#### Based-growth mechanism

The growth mechanism of metal and support with strong interaction is shown in Figure 8. In this case, hydrocarbon decomposition and carbon radical diffusion occur similar to that of the tip-growth mechanism. However, carbon radical could not diffuse through the interface of metal and support, therefore the graphitic filament was formed on metal. CNTs or CNFs were grown up with the catalyst particle rooted individually on the metal.



**Figure 8** Schematic of base-growth mechanism

**Source:** Kumar and Ando (2010)

It should be noted that, tip-growth mechanism was more interesting for the preparation of composite catalyst than that of based-growth due to the fact that with

this structure the catalyst has active metal on the tip of carbon nanotube or carbon nanofibers, leading to the unique structural characteristics of which has a resistance to deactivation caused by coking during the reaction with hydrocarbons.

Moreover, the selective formation of CNTs and CNFs depends on carbon source, and synthesis temperature as the detail shown below.

### 1. Carbon source

CNTs and CNFs can be synthesized from the catalytic decomposition reaction of different carbon sources. These carbon sources also play important roles in the growth characteristics and properties of carbon because of their own binding energy, type, and role of reactive species, and thermodynamic properties (Lee *et al.*, 2003). Many researchers have investigated the suitable carbon sources to synthesize CNTs and CNFs. In case of CNTs synthesis, acetylene, ethylene, propylene, acetone and n-pentane are frequently used as carbon sources in the CCVD method (Hernadi *et al.*, 2000; Perez-Cabero *et al.*, 2003), as the detail shown in Table 5. It was found that the different carbon source has an effect on physical properties of carbon nanofibers such as diameter and wall thickness. Considering CNFs synthesis, methane, ethylene, acetylene and carbon monoxide are widely used as the carbon sources (Perez-Cabero *et al.*, 2003). Ji and his co-worker (2013) reported that the different carbon sources could lead to the different growth mechanisms; tip-growth and base-growth. With the use of methane and carbon monoxide, CNFs were grown through tip-growth mechanism, but CNFs were grown through base-growth with the use of ethylene as the carbon source.

**Table 5** Carbon deposit, average outer and inner diameters, and wall thickness of different carbon samples

Reactants	Carbon deposit (%)	Inner diameter (nm)	Outer diameter (nm)	Wall thickness (nm)
Acetylene	83	8	22	14
Ethylene	43	5	12	12
Propylene	20	7	16	9
n-pentane	29	5	18	13
Acetone	75	6	18	12

Synthesis condition: catalyst, 2.5 wt.% Co/silica; temperature 700-800 °C; reaction time 30 min

**Source:** Hernadi *et al.* (2000)

## 2. Synthesis temperature

Many researchers have investigated the effect of synthesis temperature on the characteristics of CNTs and CNFs. In order to clearly understand this effect, CNTs and CNFs synthesis were explained separately, as the detail shown below.

### 1. Effect of synthesis temperature on CNTs growth

Generally the decomposition of carbon did not occur below 500°C. In the case of low temperature as 550°C, carbon was formed with the short length tube via the base-growth mechanism because the energy of carbon diffusion through metal was not strong enough to lift up the metal cluster, as shown in Figure 9a. Moreover, amorphous carbon was also formed as the competitive reaction at low temperature. At the moderated temperature in the range of 650-750°C, the diameter and length of CNTs were increased with increasing synthesis temperature, and the tip-growth and base-growth mechanism were found in this range of temperature (Figure 9b). At

temperature higher more than 750°C, CNTs with wide ranges of diameters were formed because some metal particles were possibly agglomerated to larger metal cluster size. Simultaneously, high temperature promoted the more carbon decomposition, leading to the more CNTs formation. At 850°C, single-walled carbon nanotubes (SWCNTs) and multi-walled carbon nanotubes (MWCNTs) were mainly observed as shown in Figure 9c and d (Kumar and Ando, 2010).

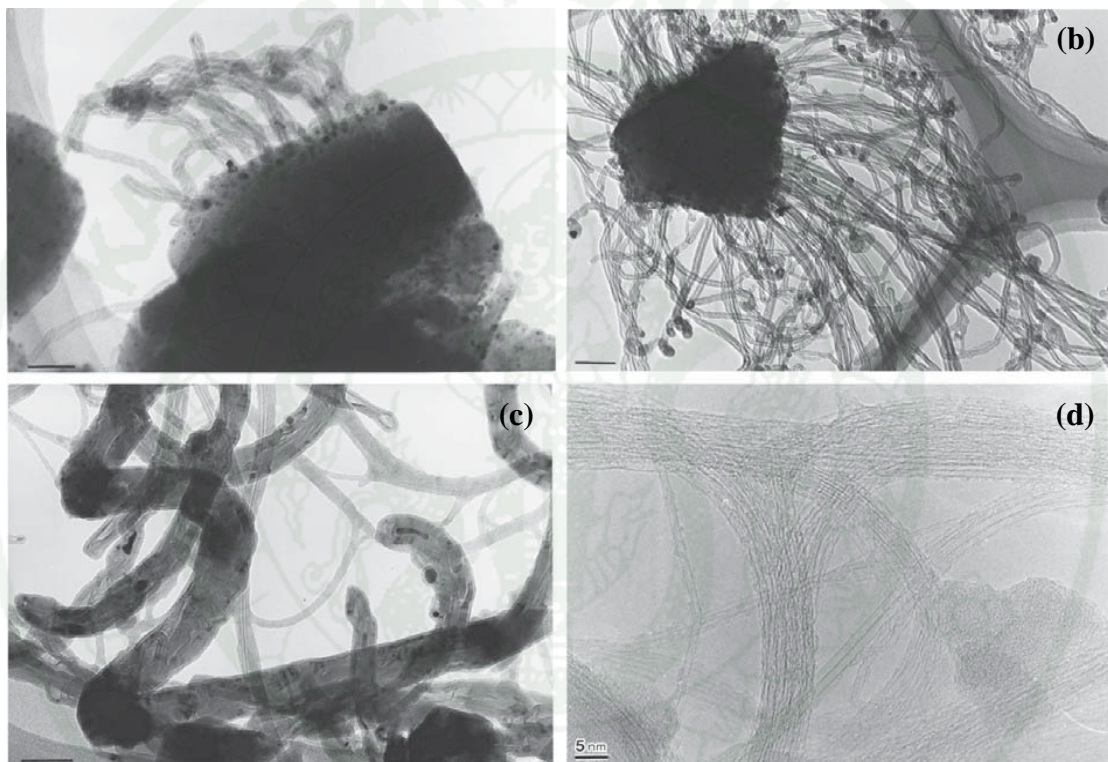


**Figure 9** TEM images of CNTs with different synthesis temperatures: (a) 550°C, (b) 650°C, (c) 900°C and (d) SWCNTs at 990°C.

**Source:** Kumar and Ando (2010)

## 2. Effect of synthesis temperature on CNFs growth

CNFs can be synthesized in two different structures including full and hollow fiber forms. At low temperature, carbon was slowly decomposed to carbon radicals and diffused to the entire backward of metal clusters, so the full fibers were formed (Figure 10a). At the moderated temperature, the feaster carbon

decomposition was occurred and carbon radicles were diffused to the interface of metal and support, leading to the formation of hollow fibers which this process was same as CNTs formation (Figure 10b) (Kumar and Ando, 2010).

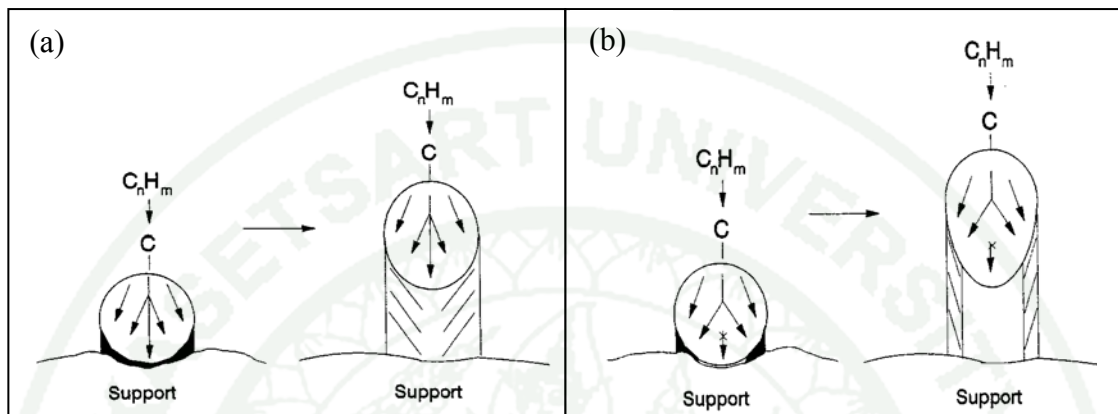


**Figure 10** Schematic of the formation of (a) full carbon nanofiber and (b) hollow carbon nanofiber.

**Source:** Kumar and Ando (2010)

## 1.4 Composites of mesoporous silica (MPS) and CNTs

### 1.4.1 Synthesis of MPS-CNTs composites

Several synthesis methods of mesoporous silica-CNTs composites are shown below.

#### 1. Addition of CNTs into MPS

Vila *et al.* (2009) studied the addition of CNTs into SBA-15 at different synthesis stages. They reported that the CNTs addition time during the synthesis had effect on the composite formation. The composite was formed when CNTs were added into ordered amorphous silica after the TEOS addition of 0-2 min, as shown in Figure 11a. In the case of CNTs addition after 20 min of TEOS addition (Figure 11b), the hexagonal and CNTs were not the only structure in the composite. In

the case of addition after 90 min (Figure 11c), the homogeneity of the composite was the highest and the obtained silica was ordered hexagonal structure while CNTs were also well dispersed.

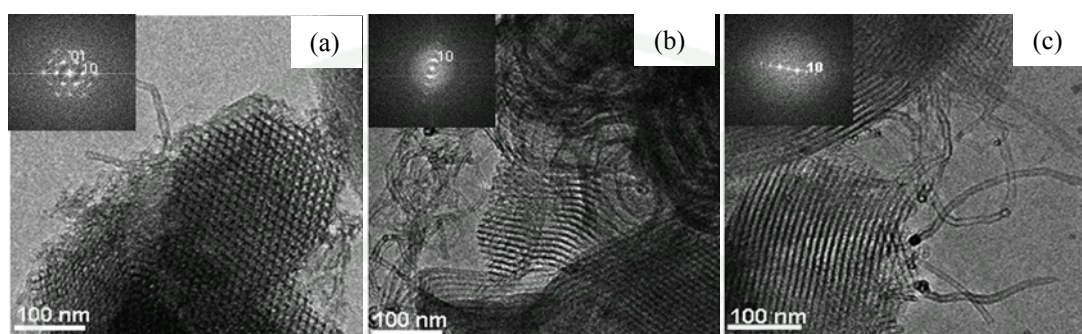


**Figure 11** TEM images of SBA-15– 2 % CNTs composites with different CNTs addition times

**Source:** Vila *et al.* (2009)

## 2. Direct synthesis of CNTs onto MPS

Many researchers studied the effect of the support, metal and the reaction condition on the structure of the synthesized CNTs-MPS composites. The different mesoporous silica supports such as MCM-41, MCM-48, SBA-15 and others silica were used in order to examine their physical and chemical properties on the selective growth of CNTs. It was found that the morphology of silica support strongly affected the CNTs growth (Ramesh *et al.*, 2005). With the support material of large and flat morphology, the CNTs were selectively synthesized on the surface. In the case of spherical and smaller morphology, the CNTs tended to suspend between such particles. Generally, CNTs were formed on the outer surface of mesoporous silica support.

In order to selectively synthesize the CNTs inside the pores of mesoporous silica, the metal loading method was investigated. Iron was loaded into

the SBA-15 support using impregnation and direct synthesis methods. In the case of direct synthesis method, metal loaded on the external surface were removed and the result was compared to that of without metal removal. It was found that MWNTs of various diameters (20 nm-90 nm) were formed on the external surface of samples which metals were not removed. The sample with metal removal could produce the MWNTs with a narrow diameter distribution, and no nanoparticles were found at the ends of the CNTs outside the mesoporous silica. It was suggested that CNTs growth originated from metal nanoparticles inside the mesoporous silica matrix and they were not transferred to the external surface of silica (Barreca *et al.*, 2007).

#### 1.4.2 Application of the CNTs-MPS composites

Recently, composites based on mesoporous silica and CNTs have been synthesized to use in many applications such as conductor composites for cell stimulation, bone regeneration, drug delivery (Vila *et al.*, 2009) and protein adsorption (Zhang *et al.*, 2010). As these composites have both characteristics of mesoporous silica and CNTs, the excellent properties including high surface area, uniform pore size distribution, high mechanical stiffness, hydrothermal stability, high mechanical property, and inert surface properties were observed (Lee *et al.*, 2008; Li *et al.*, 2010). Moreover, due to their wide variety of properties, CNTs-MS composites were also considered as a catalyst in wide variety of reactions.

## **2. The related catalytic reactions of CO<sub>2</sub> reforming of methane and liquid-phase hydrogenation reaction**

### 2.1 Carbon dioxide reforming of methane reaction

Nowadays, carbon dioxide (CO<sub>2</sub>) and methane (CH<sub>4</sub>) are continuously released to the atmosphere by the result of industrial processes, and man-made activities play a major role in global warming (Wang *et al.*, 1996; Bradford *et al.*, 2007; Bhavani *et al.*, 2013). Many attempts have been made in order to eliminate

these greenhouse gases, for example, the use as raw materials in various value-added chemical synthesis reactions such as dry reforming (Fan *et al.*, 2009; Choudhary *et al.*, 2006), methane cracking (Amin *et al.*, 2012), steam reforming of methane (Guo *et al.*, 2012), and carbon dioxide hydrogenation (Wang *et al.*, 2013). In dry reforming reaction, CO<sub>2</sub> and CH<sub>4</sub> are primarily converted to carbon monoxide and hydrogen (synthesis gas), which are further converted to alcohols (methanol and ethanol) and hydrocarbon feedstock for petrochemical industries through Fischer–Tropsch synthesis reaction (Ishida *et al.*, 2012; Zhao *et al.*, 2013).

The corresponding carbon dioxide reforming of methane reaction (Equation 4) is described as follows:

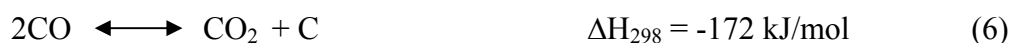


This reaction is highly endothermic and favored by low pressure and requires a higher temperature. However, there are many side reactions occurred with carbon dioxide reforming of methane reaction, as the detail shown below.

Hydrogen gas as a product is consumed through reverse water-gas shift reaction (RWGS) as shown in Equation (5).



Whereas, another product, carbon monoxide is used via Boudouard reaction as shown in Equation (6).



Moreover, the catalyst is deactivated by coke deposition through methane cracking reaction as shown in Equation (7).



Many researchers have an attempt to improve the catalyst performance in carbon dioxide reforming of methane in order to decrease the reaction temperature, solve the catalyst deactivation caused by coke deposition, and increase the desired products. The details of catalysts and mechanisms in this reaction are described as follows.

### 1. Catalyst

Carbon dioxide reforming of methane reaction was found to be actively catalyzed by certain transition metals both noble metals and non-noble metals. Noble metals such as Ru, Rh, Pd, Ir, Pt were reported to give high catalytic activity, stability and less sensitive for coke formation, but their cost are considerably high. In the case of non-noble metal (Ni, Fe, Co), nickel (Ni) metal was widely used as a metal catalyst in this reaction because it gave higher activity and stability compared to other non-noble metals, as shown in Table 6. Moreover, nickel had low cost and available. However, nickel metal was much easily deactivated by coke formation than that of noble metals, so many researchers have attempted to diminish carbon formation and enhance catalytic activity in dry reforming reaction by means of oxide supports and promoters.

**Table 6** Methane conversions with different non-noble metals loaded on silica support

Catalysts	CH <sub>4</sub> conversion (%)
Ni	80
Co	66
Fe	2
Mo	15
W	0
Cu	0

<sup>1</sup> The operating conditions were as follows: CH<sub>4</sub>/CO<sub>2</sub> mole ratio of 1, temperature of 850°C under atmospheric pressure in fixed-bed reactor.

**Source:** Edwards and Marita (1995)

Many types of materials can be used as a catalyst support such as silica, zeolite and metal oxide. Among them, metal oxide or oxide support was widely used in carbon dioxide reforming of methane because it can inhibit the coke formation on metal catalyst and prolong catalyst stability (Nagaraja *et al.*, 2011; Kambolis *et al.*, 2010). The oxide catalyst support can improve CO<sub>2</sub> adsorption on oxygen-containing surfaces and reduce the amount of carbon formation through reversed Boudouard reaction to form carbon monoxide. Moreover, oxide support can also enhance the catalyst activity, as the result shown in Table 7.

Moreover, the addition of promoter such as alkali metal, earth alkali metal and rare earth metal oxide onto catalysts could enhance the catalytic activity and limit the coke formation on the catalyst due to the unique properties of each promoter such as their highly stable oxidation state (Barroso-Quiroga *et al.*, 2010; Ballarin *et al.*, 2012).

**Table 7** CH<sub>4</sub> conversions with different supports

Catalysts	CH <sub>4</sub> conversion (%)
Ni/Al <sub>2</sub> O <sub>3</sub>	84
Ni/SiO <sub>2</sub>	79
Ni/MgO	71
Ni/La <sub>2</sub> O <sub>3</sub>	82
Ni/CeO <sub>2</sub>	63
Ni/TiO <sub>2</sub>	8
Ni/AC	5
Ni/Clay	61
Ni/Zeolite	73

<sup>1</sup> The operating conditions were as follows: CH<sub>4</sub>/CO<sub>2</sub> mole ratio of 1, temperature of 700°C under atmospheric pressure in fixed-bed reactor.

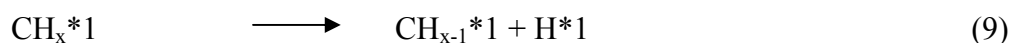
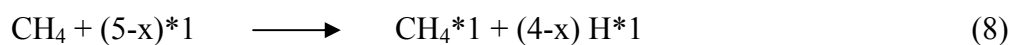
**Source:** Lu and Wang (1999)

## 2. Reaction Mechanism

The mechanism of carbon dioxide reforming of methane was proposed by many researchers (Edwards *et al.*, 1995; Ferreira-Aparicio *et al.*, 2000; Cui *et al.*, 2007) and could be concluded as described below.

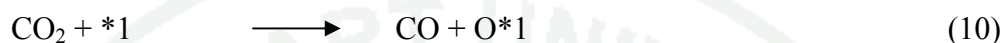
(1) CH<sub>4</sub> was firstly dissociated to the surface carbon species (CH<sub>x</sub>\*1) and hydrogen (H\*1) at the surface of active metal, as shown in Equation 8.

CH<sub>4</sub> dissociation:



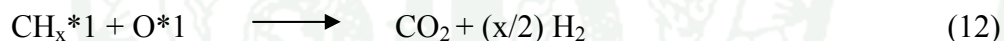
(2) CO<sub>2</sub> was decomposed to carbon monoxide (CO) and surface oxygen (O\*1 and O\*2) at both the surface of active metal (\*1) and support (\*2), as shown in Equations 10 and 11.

CO<sub>2</sub> decomposition:



(3) The surface carbon species on active surface metal (CH<sub>x</sub>\*1) could be dissociated to the lower surface carbon species (CH<sub>x-1</sub>\*1) as shown in Equation 9, and oxidized with surface oxygen (O\*1) to produce carbon dioxide (CO) and hydrogen (H<sub>2</sub>) gases, as shown in Equation 12.

Oxidation of CH<sub>x</sub>:



(4) The surface CO (CO\*1) and H (H\*1) were obtained by reforming reaction (Equation 13) as the key step to produce CO and H<sub>2</sub> gases.

Reforming reaction:



(5) The surface of active site could be regained by desorption of CO and H<sub>2</sub> gases, as shown in Equations 14 and 15.

CO desorption:



H<sub>2</sub> desorption



However, the mechanism of carbon dioxide reforming of methane could be somehow changed because of the influence of the metal and support.

## 2.2 Phenylacetylene hydrogenation in liquid phase

Phenylacetylene is concerned as a hazardous impurity in styrene feedstock which plays role as the poisoning on polymerization catalysts, therefore its maximum acceptable limit of not more than 10 ppm is required (Wilhite *et al.*, 2002; Dominguez-Dominguez *et al.*, 2008; Duraczynska *et al.*, 2009). Accordingly, phenylacetylene hydrogenation is an important process in petrochemical industry as it can eliminate the certain amounts of phenylacetylene in styrene production. Phenylacetylene can be converted to styrene through the selective hydrogenation of alkyne to alkene process. This reaction consisted of two consecutive reactions in parallel with a single directly to the final hydrogenation product as shown in Figure 12.

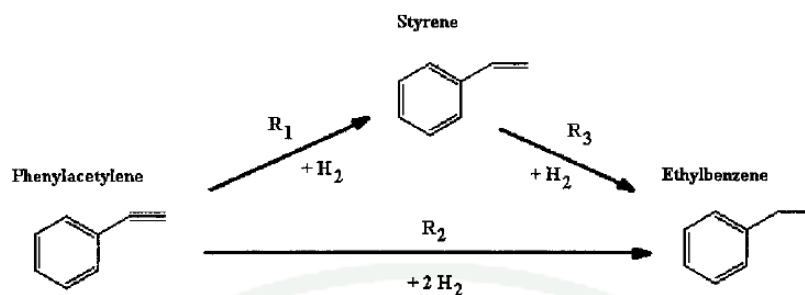


**Figure 12** Pathway of phenylacetylene hydrogenation

**Source:** Wilhite *et al.*, (2002)

### 2.2.1 Phenylacetylene hydrogenation catalysts

Phenylacetylene hydrogenation was shown to be catalyzed by transition metal such as palladium (Pd), platinum (Pt), and nickel (Ni) (Wilhite *et al.*, 2002; Dominguez-Dominguez *et al.* 2008; Relvas *et al.*, 2008). Among of them, Pd was widely used as a metal catalyst in this reaction due to its unique ability to selective hydrogenation (Dominguez-Dominguez *et al.* 2008; Basimova *et al.*, 2009). However, considering the high cost and limited availability of Pd, it is more practical to develop nickel catalyst which is cheaper and more available than that of Pd catalyst. Moreover nickel also shows high catalytic performance in hydrogenation reaction (Bautista *et al.*, 1998; Relvas *et al.*, 2008; Navalikhina *et al.*, 2012).

### 2.2.2 Support

The support is of great importance in the supported metallic catalysts because its interaction with the metallic phase has an effect on the catalytic properties and the catalyst performance in reaction. The details of supports are summarized as follows:

### Mesoporous silica

Mesoporous silica such as SBA-15 and MCM-41 is one of the frequently used supports for phenylacetylene hydrogenation because mesoporous silica has large surface area and uniform pore size, leading to enhance the metal dispersion on support (Wang *et al.*, 2012; Baudouin *et al.*, 2013). However, due to the fact that hydrogenation of phenylacetylene is carried out in liquid phase system, therefore the limitation of reactant diffusion is a major problem in the conventional catalysts (Wilhite *et al.*, 2002; Na-Chiangmai *et al.*, 2011). With an attempt to overcome the diffusion limitation of phenylacetylene, larger pore of mesoporous silica modified by swelling agent was used as the catalyst support as reported by Na-Chiangmai and co-worker (2011).

### Carbon nanotubes

Carbon nanotubes (CNTs) have been considered to be a potential catalyst support in hydrogenation reaction. CNTs have unique structure feature, electronic properties, and interaction between support and nanostructured metal particles (Li *et al.*, 2012). The surface defects and functional groups created under the strong oxidizing conditions can be used effectively as anchors for metal species (Li *et al.*, 2012).

### Titanium dioxide

Titanium dioxide ( $\text{TiO}_2$ ) is of interesting for the use as the catalyst support. It exhibits the strong metal-support interaction phenomena after reduction at high temperature because of the metal surface, this could be attributed to partially reduced metal oxide or by electron transfer between support and metal (Weerachawanasak *et al.*, 2008). Li and co-worker (2004) reported that Pd/ $\text{TiO}_2$  catalyst showed higher selectivity for alkene hydrogenation in liquid phase to long chain alkadiene.

### 3. Photocatalytic reaction of dye degradation

The photocatalytic reaction has been widely applied as a process for the degradation of organic pollutants because of its effectiveness, nontoxic process and easy operation (Zhao *et al.*, 2012; Chiou *et al.*, 2008). Among various photocatalysts, titanium dioxide (TiO<sub>2</sub>) has been widely used in photocatalytic reaction because of its performance, low cost, favorable combination of electronic structure, light absorption properties, charge transport characteristics, and excited-state lifetime (Kamat 1993; Fujishima *et al.*, 2000; Nakata *et al.*, 2012).

#### 3.1 Mechanism of photocatalytic reaction

The principle mechanism of photocatalytic reaction is shown in Figure 13. When the surface of photocatalyst (TiO<sub>2</sub>) adsorbs ultraviolet (UV) radiation from sunlight or illuminated light source (fluorescent lamp), it will produce pair of electron and holes. The electron at the valence band of TiO<sub>2</sub> becomes excited when illuminated by light. The energy difference between the valence and the conduction band is known as "the band gap". The excess energy of this excited electron promoted the electron to the conduction band of TiO<sub>2</sub>, and therefore creating the negative-electron (e<sup>-</sup>) and positive-hole (h<sup>+</sup>) pair (Fujishima *et al.*, 2000; Thiruvengkatachari *et al.*, 2008; Nakata *et al.*, 2012).

The mechanism of photocatalytic reaction described above can be represented by Equations (16)-(20) as shown below:



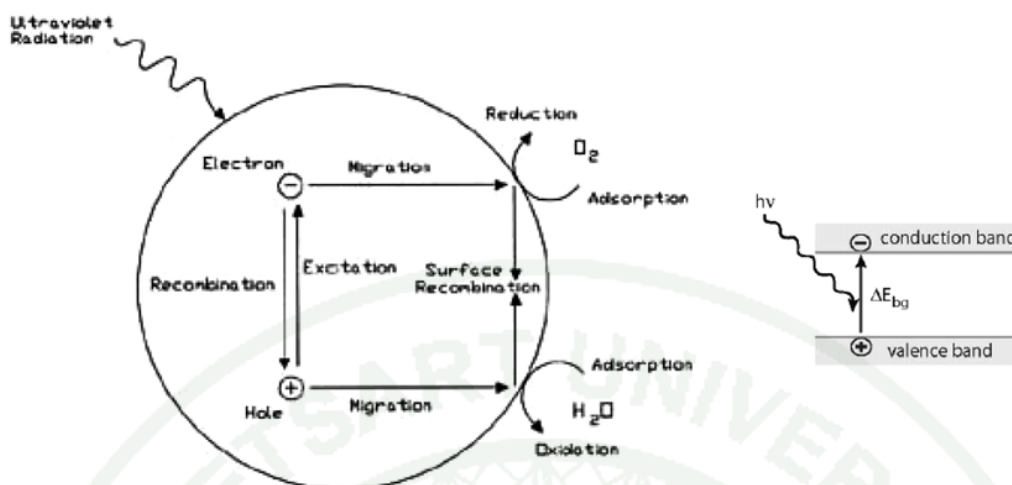


**Figure 13** Schematic representation of the mechanism of photocatalytic activity (photochemical activation and electron-hole formation)

**Source:** Thiruvengkatachari (2008)

### 3.2 Photocatalytic degradation of methylene blue

The textile industry generated dye pollutions are becoming a major source of environmental contamination. It was approximated 10 to 15 percent of dyestuff permitted to release into water during dyeing process without treatment. As international environmental standards are becoming more stringent (based on ISO 14001, October 1996), technological systems for the removal of organic pollutants, such as dyes have been recently developed (Houas *et al.*, 2001; Wu *et al.*, 2006; Yao *et al.*, 2010).

Accordingly, methylene blue is a frequently used model of cationic dye employed by textile industry for a variety of purposes. The structural formula of methylene blue is shown in Figure 14. It is a heterocyclic aromatic chemical compound with a molecular formula  $C_{16}H_{18}N_3SCl$ . Methylene blue may be responsible for permanent injury to human eyes. It can also cause irritation to the gastrointestinal tract with symptoms of nausea, vomiting and diarrhea. Methylene

blue also causes irritation to skin when in contact with it (Umoren *et al.*, 2013; Wu *et al.*, 2006).

Many methods have been applied in order to eliminate dyes contamination such as adsorption, coagulation, membrane process, oxidation-ozonation, and the degradation in photocatalytic reaction. Among them, the degradation in photocatalytic reaction has been interested because of its effectiveness and nontoxic process.

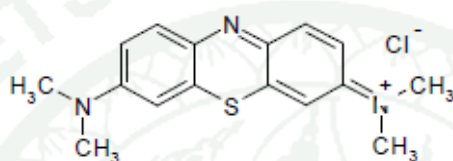


**Figure 14** Chemical structure of methylene blue dye.

**Source:** Umoren *et al.* (2013)

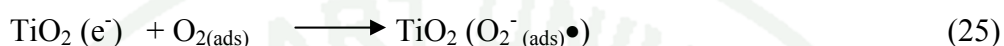
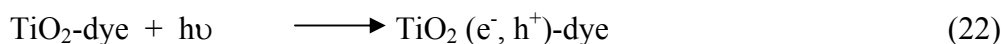
### 1. Mechanism of photocatalytic degradation of methylene blue

In order to investigate the mechanism of photocatalytic degradation of methylene blue, methylene blue solution was premixed with TiO<sub>2</sub> suspension before UV light was turned on to excite TiO<sub>2</sub> particles. The adsorption of methylene blue on the surface of TiO<sub>2</sub> particles firstly occurs in the photocatalytic reaction. Methylene blue-occupied TiO<sub>2</sub> particles were then excited to generate hydroxyl radical (OH•) and superoxide radical (O<sub>2</sub><sup>-</sup>•) of which both decomposed the adsorbed methylene blue (Wu *et al.*, 2006; Houas *et al.*, 2001). The equation of methylene blue decomposition can be explained as follows:

Equation 20 represents the reversible adsorption step of the dye molecules onto TiO<sub>2</sub> surface.



Equations 21-24 express the reaction network of OH free radical and superoxide free radical formations.



Equations 25-26 composed of the OH free radical and the superoxide free radical reacted with the pre-adsorbed dye compounds.



The reaction network based on the above reaction mechanism is shown in Figure 15.

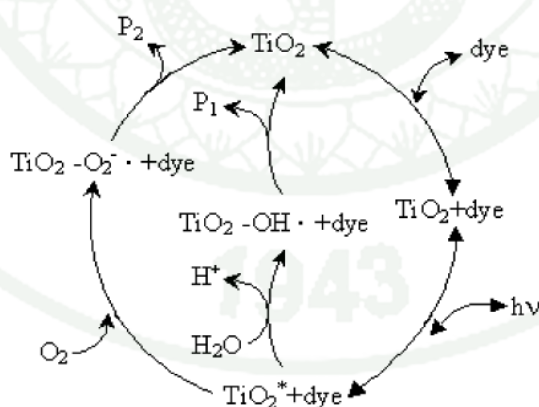


**Figure 15** Proposed organic compound decomposition pathway by photocatalytic reaction system.

**Source:** Wu (2006)

## MATERIALS AND METHODS

In this research, carbon composited with metal over porous catalyst supports have been proposed to use in various hydrocarbon reactions in order to prolong the life time of active catalysts due to coke formation and/or improve the catalytic activity. Accordingly, Ni-carbon/mesocellular silica composite catalysts and TiO<sub>2</sub>-carbon composite catalyst have been synthesized.

For the preparation of Ni-carbon/mesocellular silica composite catalysts, pores sizes of SBA-15 mesoporous silica was primarily expanded by using 1,3,5 – trimethylbenzene (TMB) as a swelling agent. The obtained products were denoted as mesocellular silica (MS). After that, nickel metal was loaded onto MS supports via incipient wetness impregnation method and then carbon were synthesized on Ni/MS catalyst by using catalytic chemical vapor deposition (CCVD) technique. The obtained Ni-carbon/MS composite catalyst was then examined for their potential application in dry reforming reaction and liquid-phase hydrogenation reaction.

Moreover, TiO<sub>2</sub>-carbon composite catalyst was also synthesized and tested in photocatalytic reaction. The details of equipment, material and method for the synthesis of mesocellular silica, nickel loading, carbon synthesis and the test for the catalytic performance on dry reforming and hydrogenation reactions, and the synthesis of TiO<sub>2</sub>/carbon composite catalysts and testing in photocatalyst degradation of methylene blue are shown as follows.

### 1. Synthesis of Ni-carbon/mesocellular silica composite catalyst

#### 1.1 Synthesis of mesocellular silica support

##### 1.1.1 Equipment of mesocellular silica synthesis

1. Digital hot plate and stirrer (Schott, SLR)
2. Magnetic hot plate and stirrer (Schott, SLR)

3. Furnace (Carbolite, ELF10/6)
4. Balance (Metler Toledo, AT 400)
5. Hot air oven (Binder, ED53)
6. Autoclave (In-house made)

#### 1.1.2 Materials of mesocellular silica synthesis

1. Sodium silicate ( $\text{Na}_2\text{Si}_3\text{O}_7$ : P.Q. company; purity 32 wt. % silica)
2. Pluronic P123 ( $\text{C}_5\text{H}_8\text{O}_4$ : Aldrich; Product code No. 435-465)
3. 1,3,5 – Trimethylbenzene or Mesitylene for synthesis (Merck)
4. Hydrochloric acid (HCl: J.T. Backer; conc. 36.5-38.0 wt. %)
5. Distilled water

#### 1.1.3 Methods of mesocellular silica synthesis

Mesocellular silica was prepared by modifying the pore diameter of SBA-15 by using 1,3,5-trimethylbenzene (TMB) as a swelling agent. The process of SBA-15 synthesis using Pluronic P123 as a pore structure-directing agent and sodium silicate as a silica source under acidic condition was described below, and the schematic of SBA-15 synthesis is summarized as shown in Figure 16.

1. The solution of Pluronic P123 was prepared by dissolved 0.00875 mole (0.875 g) of Pluronic P123 in 200 mole (60 ml) of deionized water under stirring at room temperature.

2. Sodium silicate solution (1 g) was dropped into Pluronic P123 solution and the obtained mixture was stirred at 300 rpm for 5 min.

3. Hydrochloric acid (5.4 ml) was added into the obtained mixture under vigorous stirring at 40°C for 24 h.

4. The mixture was placed in the autoclave and heated at 100°C for 24 h.

5. The solid products were separated from the mixture by filtration and washed several times with deionized water and dried at 100°C overnight in the oven and calcined in air at 550 °C for 6 h.

In the case of mesocellular silica synthesis, the similar synthesis process to SBA-15 was applied, except that 1,3,5 – trimethylbenzene (TMB, swelling agent) was added into the process of SBA-15 synthesis and the obtained product was denoted as MS. In this research, the ratios of Pluronic P123 and TMB were 1 and 2 and the sequences of TMB addition in SBA-15 synthesis shown in Table 8 were investigated.

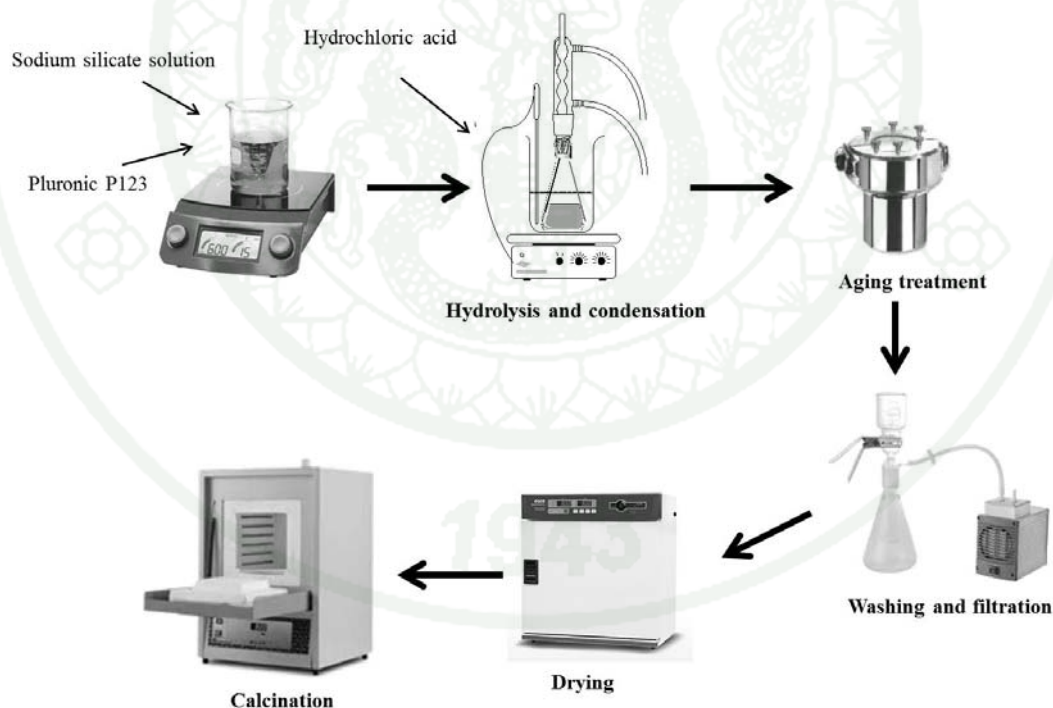


**Figure 16** Schematic diagram of SBA-15 synthesis process

**Table 8** Sequences of TMB addition in SBA-15 synthesis

Sample ID	Sequences of TMB addition
MS-1	P123 + TMB + SiO <sub>2</sub> + HCl
MS-2	P123 + SiO <sub>2</sub> + TMB + HCl
MS-3	P123 + SiO <sub>2</sub> + HCl + TMB (immediately)
MS-4	P123 + SiO <sub>2</sub> + HCl + TMB (after 1 h HCl addition)
MS-5	P123 + SiO <sub>2</sub> + HCl + TMB (after 3 h HCl addition)
MS-6	P123 + SiO <sub>2</sub> + HCl + TMB (after 6 h HCl addition)
MS-7	P123 + SiO <sub>2</sub> + HCl + TMB (after 9 h HCl addition)
MS-8	P123 + SiO <sub>2</sub> + HCl + TMB (after 12 h HCl addition)
MS-9	P123 + SiO <sub>2</sub> + HCl + TMB (after 24 h HCl addition)

#### 1.1.4 Characterization of mesocellular silica support

##### 1. N<sub>2</sub> sorption measurement

Adsorption-desorption isotherm, BET surface area, pore size distribution, and pore volume of support were analyzed by using N<sub>2</sub> sorption equipment (Quantachrome Corporation: Autosorb-1). Prior to each measurement, the sample was degassed at 200°C under vacuum and followed by flowing helium gas to remove adsorbed water and other volatile matters from the surface of the sample. The measurement was done at high vacuum level (10<sup>-4</sup> Torr) at the temperature of liquid nitrogen (-196°C) using the total N<sub>2</sub> adsorption-desorption points of 55 points.

##### 2. Transmission Electron Microscopy (TEM)

The structures of SBA-15 mesoporous silica and mesocellular silica were observed by using transmission electron microscopy (JEOL: JEM-2010 microscope with the acceleration voltage of 200 kV). The sample was prepared by

suspending in ethanol and followed by thermal evaporation of ethanol on a copper grid coated with a carbon film.

## 1.2 Synthesis of Ni-carbon/MS composite catalyst

### 1.2.1 Equipment for Ni-carbon/MS composite catalyst synthesis

1. Furnace (Carbolite: CWF 1300)
2. Thermocouple (SL: type K, class 1,200 °C, diameter 10 mm)
3. Mass flow controller (Aalborg: GFC 117)
4. Furnace (Carbolite)
5. Tube reactor (made by order, diameter 28 mm)
6. Bubble flow meter (made by order)

### 1.2.2 Materials of Ni-carbon/MS composite catalyst synthesis

1. Nickel (II) acetate:  $\text{Ni}(\text{CH}_3\text{COO})_2 \cdot 4\text{H}_2\text{O}$  (Carlo Erba reagent)
2. Quartz wool (Alltech)
3. Nitrogen gas,  $\text{N}_2$  (TIG, purity 99.9995%)
4. Acetylene gas,  $\text{C}_2\text{H}_2$  (TIG, purity 99.5 %)
5. Hydrogen gas,  $\text{H}_2$  (TIG, purity 99.9995%)

### 1.2.3 Methods of Ni-carbon/MS composite catalyst synthesis

#### 1. Nickel metal loading

Nickel/MS catalysts with different amounts of Ni loading were prepared by incipient wetness impregnation method using nickel (II) acetate as a nickel precursor as the following procedure:

1. A required amount of an aqueous solution of nickel (II) acetate 0.212 g (5 wt.%) and 0.424 (10 wt.%) was added with MS support (1 g).

2. The mixture was agitated at room temperature for 1 h, air-dried in an oven at 100°C overnight and calcined in air at 550°C for 4 h. The catalyst was denoted as x Ni/MS.

## 2. Synthesis of carbon nanotubes composite catalyst

Carbon nanotubes were synthesized via catalytic chemical vapor deposition (CCVD) technique in a fixed-bed steel reactor (28 mm inner diameter). The synthesis details are as follows:

1. The 0.2 g of x Ni/MS was placed in the center of the CCVD reactor and reduced with hydrogen at the flow rate of 20 ml/min at 500 °C for 4 h. After that, the reactor was flushed with nitrogen at the flow rate 18 ml/min and the temperature was increased to 750 °C.

2. Acetylene gas was then fed into the reactor at the flow rate of 2 ml/min for 60 min. After that, the reactor was cooled to room temperature under nitrogen. The obtained product was denoted x Ni-CNTs/MS catalyst.

## 3. Synthesis of carbon nanofibers composite catalyst

Carbon nanofibers were synthesized via CCVD technique in a fixed-bed alumina reactor (28 mm inner diameter). The synthesis details are as follows:

1. The 0.2 g of x Ni/MS was placed in the center of the CCVD reactor and reduced with hydrogen at the flow rate of 60 ml/min at 500 °C for 1 h. After that, the reactor was flushed with nitrogen at the flow rate 100 ml/min for 30 min.

2. Methane gas was then fed into the reactor at the flow rate of 50 ml/min with different synthesis times and was cooled to room temperature under

nitrogen. The obtained products were denoted as 10Ni-CNFs(1)/MS and 10Ni-CNFs(3)/MS corresponded the synthesis times of 1 and 3 h, respectively.

#### 1.2.4 Characterization of Ni-carbon/MS composite catalyst

##### 1. N<sub>2</sub> sorption measurement

Nitrogen sorption technique was used to analyze adsorption-desorption isotherm, BET surface area, pore size distribution, and pore volume of composite catalyst (Model: Autosorb1, Quantachrome Corporation). Prior to each measurement, the sample was degassed at 200°C under vacuum and followed by flowing helium gas to remove adsorbed water and other volatile matters from the surface sample. The measurement was done at high vacuum level ( $10^{-4}$  Torr) at the temperature of liquid nitrogen (-196°C) using the total N<sub>2</sub> adsorption-desorption points of 55 points.

##### 2. Transmission Electron Microscopy (TEM)

The composite catalysts structure was observed by using transmission electron microscopy (TEM: Hitachi HT7700 with the acceleration voltage of 120 kV). The sample was prepared by suspending in ethanol and followed by thermal evaporation of ethanol on a copper grid coated with a carbon film.

##### 3. Field Emission Scanning Electron Microscopy (FE-SEM)

The morphology of fresh and used composite catalysts were observed by using field emission scanning electron microscope (FE-SEM: Hitachi SU8020) operated at 20 keV with Pt-coated using sputtering technique.

#### 4. X-ray Diffraction (XRD) Spectroscopy

The crystalline phases of nickel and graphite were examined by using X-Ray diffraction spectroscopy (XRD: Bruker, D8 Advance) operated with monochromated Cu K $\alpha$  radiation (40 kV to 40 mA) at room temperature. The crystallite sizes of nickel metal was calculated by using Scherrer equation (Equation 25) from the most intense Ni metal peak at 2 $\theta$  of 44 $^\circ$ .

$$d = \frac{0.89\lambda}{B \cos \theta} \times \frac{180^\circ}{\pi} \quad (25)$$

where  $d$  = mean crystallite diameter

$\lambda$  = X-ray wave length (1.54 Å)

$B$  = full width half maximum (FWHM) of nickel metal diffraction peak

#### 5. Thermogravimetric analysis (TGA)

The types and amounts of carbon on the composite catalyst were determined by using thermogravimetric analyzer (TG-DTA: TA instrument, SDT2960 simultaneous DSC-TGA universal 2000). In the analysis process, the sample was heated in air atmosphere from room temperature to 800 $^\circ$ C at the heating rate of 5 $^\circ$ C/min.

#### 6. CO chemisorption

The amount of nickel active atoms on composite catalyst was determined by using CO adsorption measurement (BEL-METAL-1, BEL Japan, Inc.). The catalyst was pretreated under hydrogen flow at 700 $^\circ$ C for 1 h. After reduction, the catalyst was evacuated to remove the residual hydrogen, and then cooled to 50 $^\circ$ C for analyses. The CO chemisorption was operated at 50 $^\circ$ C. The number of exposed metal atoms on the surface was calculated from the amount of CO adsorbed at stoichiometric value of CO: Ni equals to 2.

## 7. Raman spectroscopy

The crystallinity of carbon on composite catalyst was analyzed by using Raman spectroscopy (NTEGRA spectra, NT-MDT).

## 8. Water adsorption

Water adsorption isotherms at 298 K were recorded by using a BEL-SORP max (BEL Japan, Inc.) after degassing samples under vacuum at 200°C for 2 h. The relative water adsorption capacity was calculated by the adsorbed amount of water on each Ni-CNFs/MS catalysts at  $P/P_0 = 0.5$ .

## 2. Catalytic performance of composite catalysts

Ni-carbon/MS composite material was applied as the catalyst and tested in both of dry reforming reaction (gas-phase reaction) and phenylacetylene hydrogenation (liquid-phase reaction). The detail of equipments, materials and methods each of reaction are provided below.

### 2.1 Dry reforming reaction

#### 2.1.1 Equipment for dry reforming reaction

##### 1. Catalytic reaction testing unit

- 1.1 Pressure regulator
- 1.2 Mass flow controller (GFC117, Aalborg)
- 1.3 Mass flow controller (8300 Series, KOFLOG)
- 1.4 Thermocouple (K-type)
- 1.5 Temperature controller (120-R/E, Shino)
- 1.6 Temperature indicator (RI, Shino)
- 1.7 Tube furnace (CFW 1300, Carbolite)

## 1.8 Bubble flow meter

### 2. Gas analysis unit

2.1 Gas chromatograph equipped with thermal conductivity detector (TCD) (GC-2014, Shimadzu) was used to quantitatively analyze the amounts of H<sub>2</sub>, CO, CO<sub>2</sub>, CH<sub>4</sub>, and water.

2.2 Gas-tight syringes (1002LTN gastight syringe, Hamilton; and A-2 type gas tight syringe, PS)

#### 2.1.2 Materials used in dry reforming reaction

##### 1. Reactant gases

1.1 Carbon dioxide (CO<sub>2</sub>: 99.2 % purity, TIG)

1.2 Methane (CH<sub>4</sub>: 99.99 % purity, TIG)

1.3 Hydrogen (H<sub>2</sub>: 99.99 % purity, TIG)

1.4 Nitrogen (N<sub>2</sub>: 99.99% purity, TIG)

##### 2. Standard gases

Mixture of 25% carbon monoxide (CO), 25% carbon dioxide (CO<sub>2</sub>), 25% methane (CH<sub>4</sub>), 25% hydrogen (H<sub>2</sub>) was used as the standard gas (SOXAL).

3. Quartz wool – Quartz wool was used as the catalyst bed support (Alltech).

#### 2.1.3 Methods for dry reforming reaction

The catalytic testing unit for dry reforming reaction is shown in Figure 17. This experimental unit consists of a feed flow measuring and controlling system, a furnace equipped with stainless steel tube reactor and a sampling system. The catalytic reaction testing unit was designed to operate under high temperature and atmospheric pressure conditions. The details of particular system are explained below.

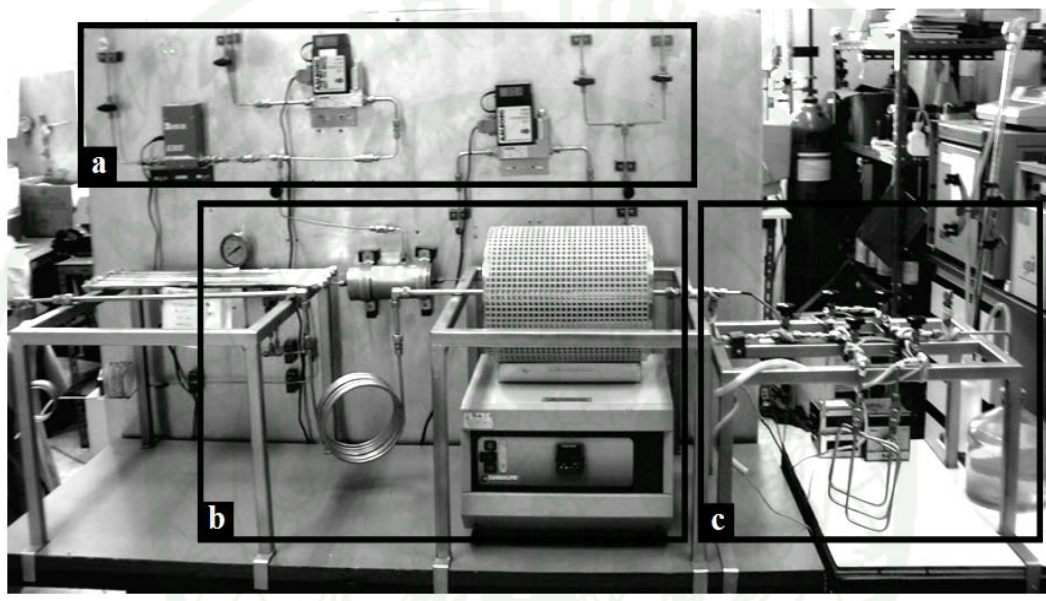


**Figure 17** Catalytic reaction testing unit: (a) a feed flow measuring and controlling system, (b) a furnace-equipped stainless steel tube reactor and (c) a sampling system.

### 1. Feed flow measuring and controlling system

In this system, mass flow controllers were used to finely indicate and control the flow rates of feed gases including hydrogen, carbon dioxide and methane. Carbon dioxide and methane were used as reactant gases, and hydrogen was used for the catalyst reduction. In order to monitor the system leakage, nitrogen gas was applied. Flow rates of hydrogen, methane, and nitrogen were measured and controlled by Aalborg mass flow controller (Figure 18a) and KOFLOC mass flow controller (Figure 18b) was used to control the flow rate of carbon dioxide.

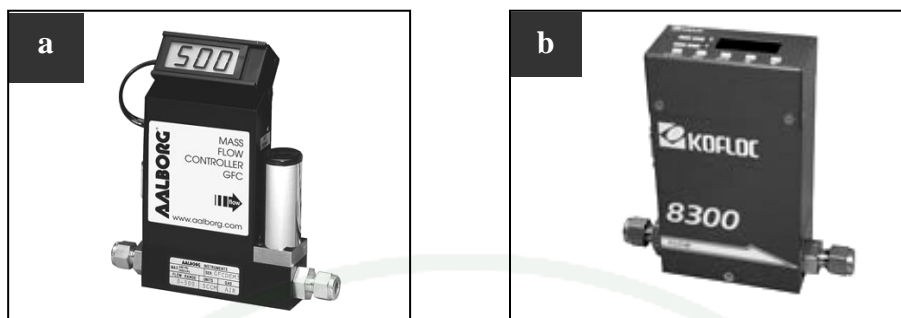


**Figure 18** Mass flow controller: (a) Aalborg GFC thermal mass flow controller and (b) KOFLOC mass flow controller and mass flow meter with indicator.

## 2. Pack-bed reactor

The inconel tube (O.D. 3/8") was used as the fixed-bed reactor. During the reaction stage, the tube reactor was heated with an electric heater (Figure 19) controlled by the temperature controller. The K-type thermocouple connecting to a temperature controller unit was inserted inside the tube reactor in order to measure and accurately control the temperature of the catalyst bed. The catalyst powder was packed in the isothermal zone of the tube reactor and fixed between quartz wool layers as the scheme shown in Figure 20.

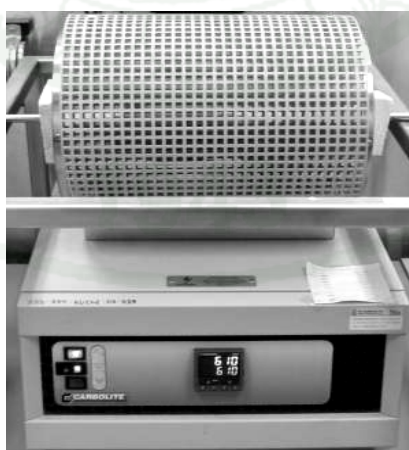


**Figure 19** Tube reactor equipped with the electric heater (Carbolite tube furnace).

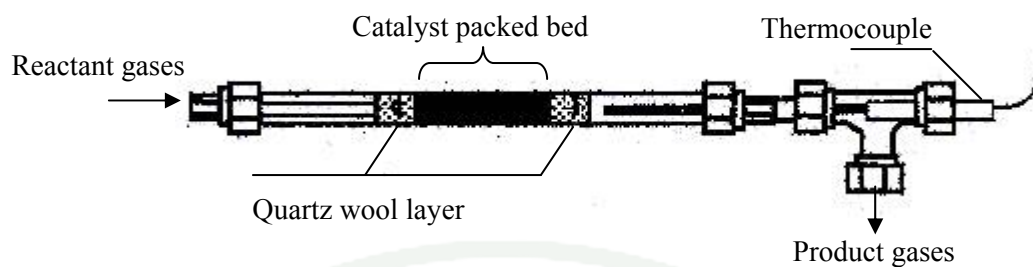


**Figure 20** Schematic setup of pack-bed reactor.

### 3. Operating conditions of dry reforming reaction

Before testing the catalytic performance, 0.1 g of catalyst was mixed with 0.4 g of inert sand and packed in an inconel tube reactor (3/8 in. outer diameter) placed horizontally in the center of a tubular furnace equipped with k-type thermocouple located in the center of the catalyst bed.

The catalyst was firstly reduced in hydrogen atmosphere at 700°C for 1 h prior to the performance test. During dry reforming reaction, carbon dioxide and methane were converted to synthesis gas over the catalyst bed at the constant reaction temperature (650°C) and atmospheric pressure with CO<sub>2</sub>/CH<sub>4</sub> molar ratio of 1 and total gas flow rate of 40 ml/min. The obtained products were analyzed by a gas chromatograph (Shimadzu, GC-2014) equipped with thermal conductivity detector and Unibead C column at the operating condition as shown below.

The conditions for analysis of H<sub>2</sub>, CO, CH<sub>4</sub> and CO<sub>2</sub> were:

- Carrier gas (Ar) flow rate: 25 ml/min
- Injector temperature: 150 °C
- Column temperature: 150 °C
- Detector temperature (Pre): 150 °C
- Detector temperature: 150 °C
- Current: 60 mA

## 2.2 Phenylacetylene hydrogenation reaction

### 2.2.1 Equipment for phenylacetylene hydrogenation reaction

1. Glass reactor fitted with a reflux condenser (made by order)
2. Magnetic stirrer and oil bath
3. Furnace (made by order)
4. Rotameter (floating body)

### 2.2.2 Materials for phenylacetylene hydrogenation reaction

1. Phenylacetylene ( $C_8H_6$ : 97.0 % purity, TCI)
2. Biphenyl ( $C_6H_5C_6H_5$ , nacalai tesque)
3. 2-propanol ( $CH_3CH_2CH_2OH$ , nacalai tesque)
4. Hydrogen ( $H_2$ : 99.99 % purity)

### 2.2.3 Methods for phenylacetylene hydrogenation reaction

Before testing the catalyst performance, 20 mg of catalyst (Ni/MS, Ni-CNFs(1)/MS and Ni-CNFs(3)/MS) was placed in a glass reactor with a reflux condenser in the center of furnace equipped with thermocouple located at the side of the glass reactor. Prior to each experiment, the catalyst was reduced with hydrogen gas at  $450^\circ C$  for 1 h.

The mixture of reactants (PA; 0.174 g, 2-propanol; 5 ml, and biphenyl (internal standard); 0.077 g) was introduced into the glass reactor under magnetic stirring at  $80^\circ C$  in oil bath. After that, hydrogen gas (5 ml/min) was continuously fed into the mixture. The remained reactant (PA) and the reaction products (styrene and ethylbenzene) were analyzed by Shimadzu GC-2014 gas chromatograph using flame ionization detector (FID) equipped with Rtx®-5 capillary column (5 % phenyl and 95 % dimethyl polysiloxane) at the condition as shown below.

- Carrier gas (He) pressure: 30 kPa
- H<sub>2</sub> gas pressure: 60 kPa
- Air gas pressure: 50 kPa
- Injector temperature: 250 °C
- Initial column temperature: 80 °C
- Holding time: 5 min
- Temperature program rate: 20 °C/min
- Final column temperature: 250 °C

### 3. Photocatalytic reaction

#### 3.1 Synthesis of TiO<sub>2</sub>/carbon composite catalyst

##### 3.1.1 Equipment for TiO<sub>2</sub>/carbon composite catalyst preparation

1. Magnetic hot plate and stirrer (Schott, SLR)
2. Balance (Metler Toledo, AT 400)
3. Hot air oven (Binder, ED53)

##### 3.1.2 Materials for TiO<sub>2</sub>/carbon composite catalyst preparation

1. TiO<sub>2</sub> slurry in 2-propanol (18 wt. % of TiO<sub>2</sub>, Tayca co., Japan)
2. Pure TiO<sub>2</sub> (AMT-100, Tayca corp., Japan)
3. Zeolite template carbon (ZTC, Kyotani Lab)
4. Commercial activated carbon (AC, Shirasagi)

##### 3.1.3 Methods for TiO<sub>2</sub>/carbon composite catalyst synthesis

TiO<sub>2</sub> slurry (Tayca corporation, Japan) used as a titanium dioxide source was prepared on the different carbon materials support including ZTC and commercial activated carbon (AC, Shirasagi). ZTC was prepared in accordance with previous literatures (Paredes *et al.*, 2005 and Nishihara *et al.*, 2009). The composite

catalyst was synthesized via a simple impregnation method. Firstly carbon material was suspended in  $\text{TiO}_2$  dissolved in 2-propanol solution under stirring at room temperature for 30 min. After that temperature was increased to  $70^\circ\text{C}$  for 2-propanol evaporation under reduced pressure. The obtained composite catalyst was dried at  $100^\circ\text{C}$  for 12 h. The amount of  $\text{TiO}_2$  was adjusted to 5 wt. % in each sample.

### 3.1.4 Characterizations of $\text{TiO}_2$ /carbon composite catalyst

#### 1. X-Ray Diffraction Spectroscopy (XRD)

The crystalline phases of titanium dioxide were examined by using X-Ray diffraction spectroscopy (XRD: Rigaku Ultima IV) operated with monochromated  $\text{Cu K}\alpha$  radiation (40 kV to 40 mA) at room temperature.

#### 2. Transmission Electron Microscopy (TEM)

The structure of composite catalysts between  $\text{TiO}_2$  and carbon was observed by using transmission electron microscopy with the acceleration voltage of 200 kV (TEM: JEOL, JEM-2010). The sample was prepared by suspending in ethanol and followed by thermal evaporation of ethanol on a copper grid coated with carbon film.

#### 3. $\text{N}_2$ sorption measurement

Nitrogen sorption technique was used to analyze adsorption-desorption isotherm, BET surface area, pore size distribution, and pore volume of composite catalyst (BEL Japan, BELSORP-max). Prior to each measurement, the sample was degassed at  $200^\circ\text{C}$  under vacuum and followed by flowing helium gas to remove adsorbed water and other volatile matters from the surface of sample. The measurement was operated at high vacuum level at the temperature of liquid nitrogen ( $-196^\circ\text{C}$ ).

#### 4. Water adsorption

Water adsorption isotherms at 298 K were recorded by using a BEL-SORP max (BEL Japan, Inc.) after degassing samples under vacuum at 200°C for 2 h. The relative water adsorption capacity was calculated by the adsorbed amount of water on each composite catalysts of TiO<sub>2</sub> and carbon at  $P/P_0 = 0.3$ .

##### 3.2 Photocatalyst degradation of methylene blue

###### 3.2.1 Equipment for photocatalyst degradation of methylene blue

1. Hot plate with magnetic stirrer (Schott, SLR)
2. Glass tube (made by order)
2. Magnetic stirrer
3. High-pressure mercury lamp and cooling system
4. Rotameter (floating body)

###### 3.2.2 Materials used for photocatalyst degradation of methylene blue

1. Methylene blue (C<sub>16</sub>H<sub>18</sub>N<sub>3</sub>S.Cl<sub>3</sub>H<sub>2</sub>O, cica reagent, Kanto chemical CO.,Inc)
2. Oxygen (O<sub>2</sub>: 99.99 %)

###### 3.2.3 Methods used for phenylacetylene hydrogenation reaction

###### 1. Methylene blue adsorption measurement

The adsorption capacity of different supports in methylene blue (MB) solution was investigated under dark condition at room temperature. Each support (10 mg) was added into MB (concentrations: 0.3, 0.5 0.7 and 1 mM) under stirring for 30 min. After reaching equilibrium, the absorption of remained MB at around 664 nm was monitored by using diffuse reflectance UV-visible spectroscopy

in the wavelength between 400-800 nm at 298 K with a Shimadzu UV- 2450A double-beam digital spectrophotometer.

## 2. Photocatalyst degradation of methylene blue

The photocatalytic activity of catalysts was evaluated by the decolorization of MB diluted in water. In each reaction test, the catalyst of 10 mg was used. An aqueous MB (30 ml; 2 mmol/l) was fed into a quartz reaction vessel exposed to UV light irradiation (intensity of 5 mW/cm<sup>2</sup>). The reaction was carried out at 298 K by using a high-pressure mercury lamp. The changes of solution color were monitored by UV-vis absorption measurement using a UV-2450A spectrometer at certain time intervals. Photocatalytic activity was also tested on TiO<sub>2</sub> powder (AMT-100; Tayca corp., Japan) as a reference.

## RESULTS AND DISCUSSION

In this research, the carbon composited with metal over porous catalyst supports have been proposed to use in various hydrocarbon reactions in order to prolong the life time of active catalysts due to coke formation and/or improve the catalytic activity. Accordingly, the carbons (carbon nanotubes (CNTs) and carbon nanofibers (CNFs)), composited with nickel (Ni) metal over mesocellular silica (MS) support were synthesized and used as the catalysts in gas-phase and liquid-phase reactions. Moreover, the carbon composited with titanium dioxide ( $\text{TiO}_2$ ) was also prepared and its performance on photocatalyst reaction was investigated. In the view of that, the result and discussion has been categorized into 4 parts including (1) mesocellular silica synthesis, (2) effect of Ni-CNTs/MS composite catalyst on dry reforming reaction, (3) effect of Ni-CNFs/MS composite catalyst on liquid-phase hydrogenation reaction, and (4) effect of  $\text{TiO}_2$ /carbon photocatalyst on dye degradation. The details of each part are shown as follows.

### 1. Mesocellular Silica Synthesis

It was found that the textural and structural characteristics of mesocellular silica (MS) support strongly depended on the amount of swelling agent (1,3,5-trimethylbenzene (TMB)) and the sequences of TMB addition in the synthesis process, as the results shown below.

#### 1.1 Effect of Pluronic P123 to TMB ratio

The textural and structural characteristics of SBA-15 mesoporous silica and mesocellular silica were compared by using the nitrogen adsorption-desorption isotherms and TEM images obtained with different Pluronic P123 to TMB ratios as shown in Figure 21A. It was found that SBA-15 exhibited type IV isotherm with H1 hysteresis loop, indicating the mesoporous structure with uniform cylindrical pore size. After SBA-15 mesoporous silica was modified by using TMB, MS obtained with

different Pluronic P123 to TMB ratios showed type IV isotherm with H2 hysteresis loop, representing the mesoporous structure with less uniform pore size.

Figure 21B reported the pore size distribution of SBA-15 and MS with different Pluronic P123 to TMB ratios. SBA-15 mesoporous silica had a narrow pore size distribution with mean pore size of approximately 9 nm, while the pore diameters of MS supports were expanded in the range of 7-30 nm with Pluronic P123 to TMB ratio equal to 1, and in the range of 12-200 nm with Pluronic P123 to TMB ratio equal to 2, as shown in Figure 21B. The specific surface area and pore volume were calculated by using Brunauer-Emmett-Teller (BET) method, as the results shown in Table 9. SBA-15 mesoporous silica shows the highest specific surface area and the smallest pore volume. Considering MS support, the specific surface area was decreased and pore volume was increased with increasing Pluronic P123 to TMB ratios from 1 to 2.

In order to compare the structure of SBA-15 and MS support, TEM technique was used to observe the pore characteristics, as shown in Figure 22. SBA-15 revealed high ordered hexagonal pore structure. In the case of MS support with different Pluronic P123 to TMB ratios, hexagonal mesostructure was changed to mesocellular structure (spherical pore). Moreover, MS support with the ratio of 2 had more well-formed pore structure than that of the ratio 1.

From nitrogen adsorption data and TEM images, the synthesis condition of MS support with the ratio of 2 was selected to apply for further investigation regarding the sequence of TMB addition affecting the mesocellular structure. From nitrogen adsorption result and TEM image (Figures 21 and 22), it can be explained that after adding TMB into Pluronic P123 solution, molecules of TMB then expanded the hydrophobic region of Pluronic P123 micelle, as shown in Figure 23. As a result, mesocellular silica had larger pore diameter than that of SBA-15.

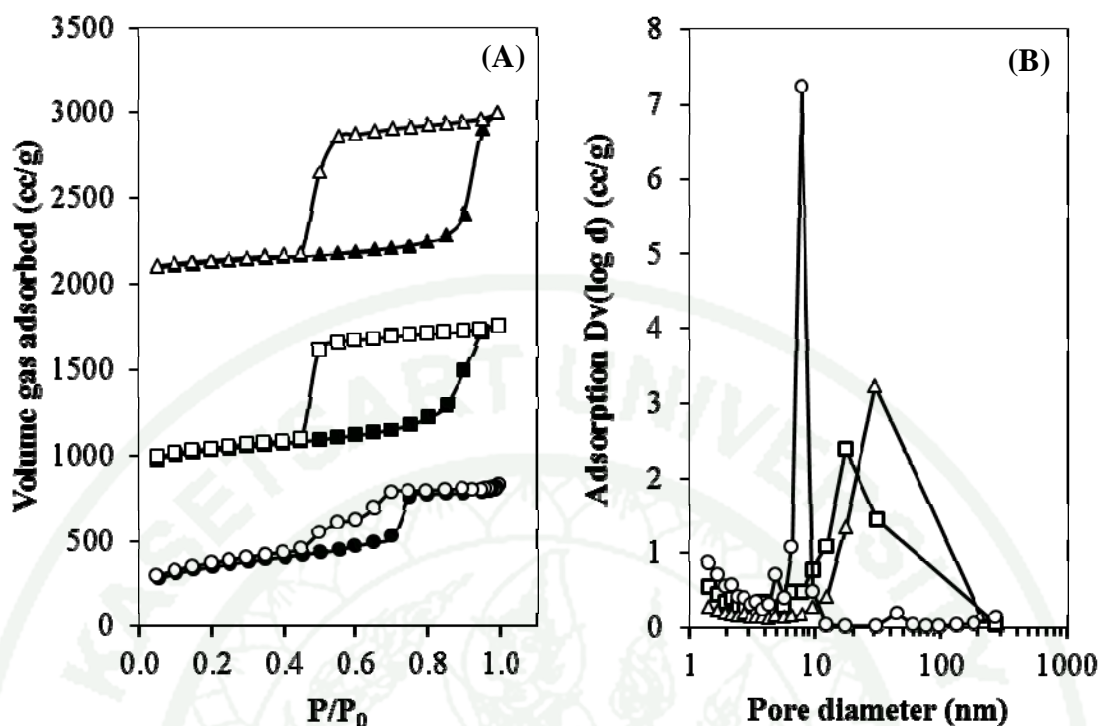


**Figure 21** (A) Nitrogen adsorption-desorption isotherm and (B) pore size distribution of MS support and catalysts.

○ SBA-15, □ MS (P123:TMB=1), and △ MS (P123:TMB=2)

**Table 9** Physical properties of SBA-15 mesoporous silica and mesocellular silica with different Pluronic P123 to TMB ratios

Samples	BET surface area ( $\text{m}^2/\text{g}$ )	Total pore volume ( $\text{cc}/\text{g}$ )
SBA-15	860	0.95
MS (P123:TMB=1)	751	1.47
MS (P123:TMB=2)	432	1.53

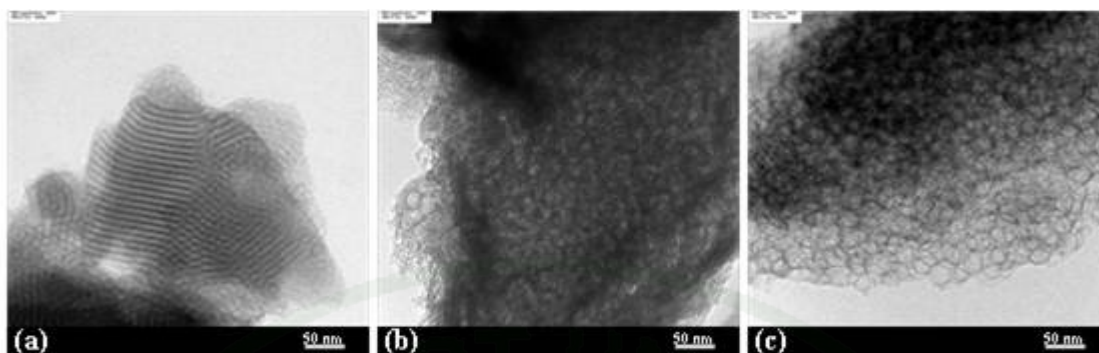


**Figure 22** TEM images of SBA-15 mesoporous silica and mesocellular silica with different Pluronic P123 to TMB ratios. (a) SBA-15, (b) MS (P123: TMB = 1), and (c) MS (P123: TMB = 2).

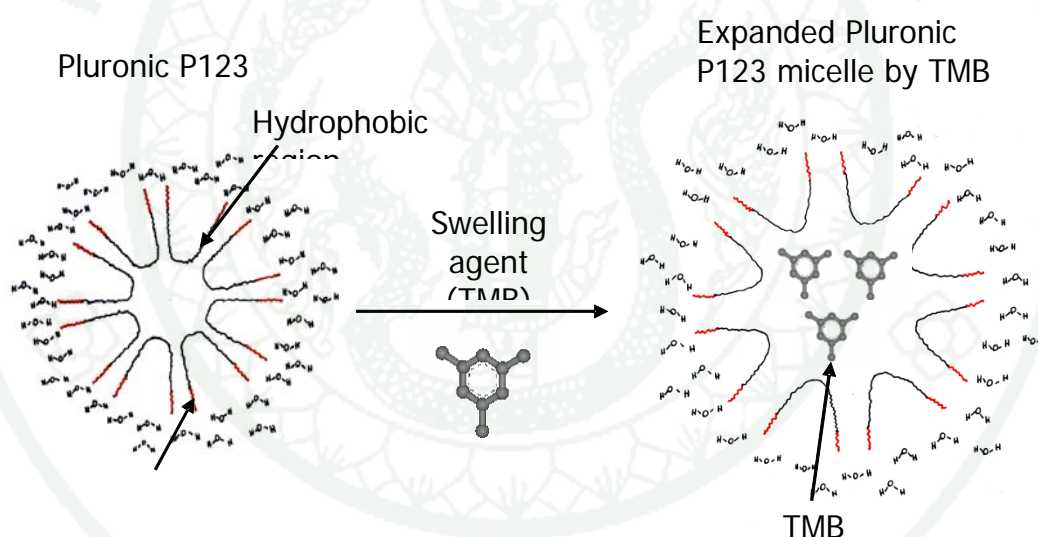


**Figure 23** Expansion of Pluronic P123 micelle with TMB as a swelling agent

## 1.2 Effect of sequences of TMB addition

Figure 24 shows nitrogen adsorption-desorption isotherm of mesocellular silica synthesized with different sequences of TMB addition. It was found that mesocellular silica with TMB addition prior to HCl (MS-1 and MS-2), immediately after HCl (MS-3), and 1-h after HCl (MS-4) exhibited type IV isotherm with H2 hysteresis loop. Whereas the mesocellular silica obtained with HCl addition 3-h, 6-h,

9-h, 12-h and 24-h prior to TMB (denoted as MS-5, MS-6, MS-7, MS-8 and MS-9, respectively) showed type IV isotherm with H1 hysteresis loop, similar to SBA-15 isotherm.

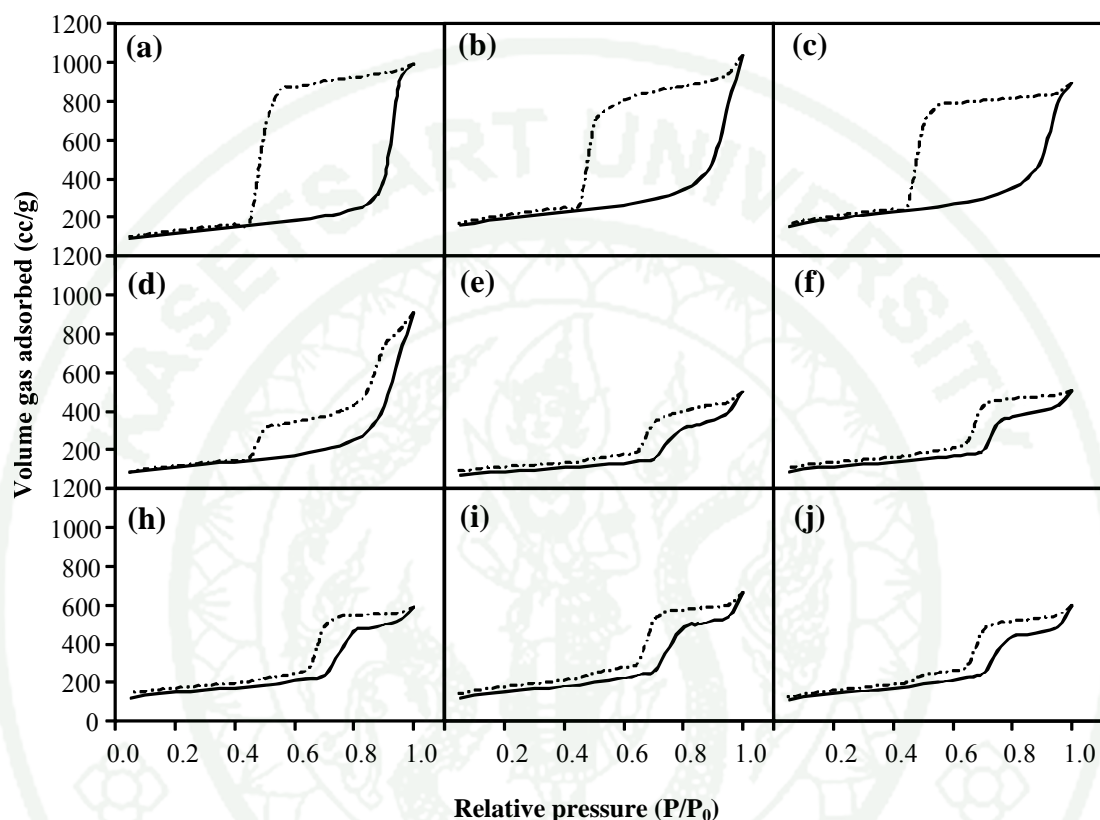


**Figure 24** Nitrogen adsorption-desorption isotherm of mesocellular silica with different sequences of TMB addition. (a) MS-1, (b) MS-2, (c) MS-3, (d) MS-4, (e) MS-5, (f) MS-6, (g) MS-7, (h) MS-8, and (i) MS-9.

Pore size distribution of mesocellular silica synthesized with different sequences of TMB addition is shown in Figure 25. Mesocellular silica with TMB addition prior to HCl, immediately after HCl and 1-h after HCl addition (Figure 25a, b, c, and d) exhibited wide ranges of pore size distribution with mean pore diameter of approximately 30 nm. On the other hand, mesocellular silica synthesized with HCl addition prior to TMB (Figure 25e, f, g, h, i and j) demonstrated the narrow pore size distribution approximately 7 nm as similar to SBA-15 pore size.

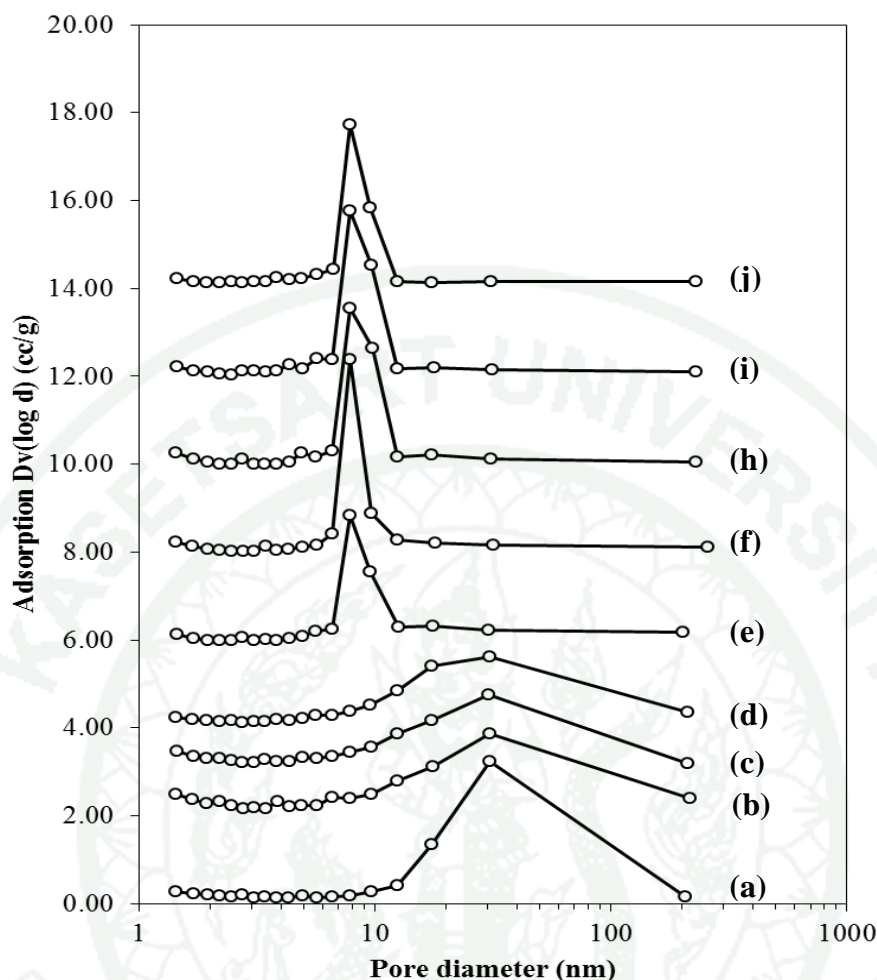


**Figure 25** Pore size distribution of mesocellular silica with different sequences of TMB addition; (a) MS-1, (b) MS-2, (c) MS-3, (d) MS-4, (e) MS-5, (f) MS-6, (g) MS-7, (h) MS-8, and (i) MS-9.

Table 10 shows BET surface area and pore volume of mesocellular silica obtained with different sequences of TMB addition. It was found that the BET surface area of mesocellular silica did not change with the sequence of TMB addition. However, pore volume of mesocellular silica synthesized with TMB addition prior to HCl, immediately after HCl, and 1-h after HCl addition (MS-1, MS-2, MS-3 and MS-4) were in the range of 1.4-1.6 cc/g of which were larger than that of HCl addition prior to TMB (MS-5, MS-6, MS-7, MS-8, and MS-9). The later was in the range of 0.8-1.0 cc/g.

**Table 10** Physical properties of SBA-15 mesoporous silica and mesocellular silica with different sequences of TMB addition

Samples	BET surface area (m <sup>2</sup> /g)	Total pore volume (cc/g)
MS-1	432	1.53
MS-2	663	1.60
MS-3	659	1.38
MS-4	400	1.40
MS-5	309	0.77
MS-6	398	0.78
MS-7	500	0.91
MS-8	518	1.02
MS-9	495	0.92

Figure 26 shows TEM images of mesocellular silica obtained with different sequences of TMB addition. Considering mesocellular silica synthesized with TMB addition prior to HCl, immediately after HCl, and specific periods after HCl addition, the structure of mesocellular silica obtained with TMB addition immediately after HCl exhibited the highest ordered mesocellular structure with larger pore than that of the other conditions.

This could be attributed to the fact that in the case of TMB addition immediately after HCl, the structures of micelle (Pluronic P123) were not rigid and

therefore the swelling agent (TMB) could uniformly penetrate into the hydrophobic regions of micelle and evenly expand the micelle structure during hydrolysis-condensation process. As a result, micelle with mesocellular structure was obtained. On the other hand, it should be mentioned that TMB had less effect on the micelle structure of Pluronic P123 after a period of HCl addition because the hydrolysis-condensation process occurred immediately after HCl addition into the mixture of Pluronic P123 and sodium silicate solution under the suitable temperature. Therefore, the molecule of TMB could not penetrate inside and expand the Pluronic P123 micelle. Moreover, in the case of TMB addition prior to HCl, the structure of Pluronic P123 micelle expanded by TMB was not stable; it could be transformed under stirring condition. Although sodium silicate solution was added into this solution, the structure of silica formed over this Pluronic P123 micelle could be still transformed until HCl was added into the solution under suitable temperature. Accordingly, disordered mesocellular structure was observed.

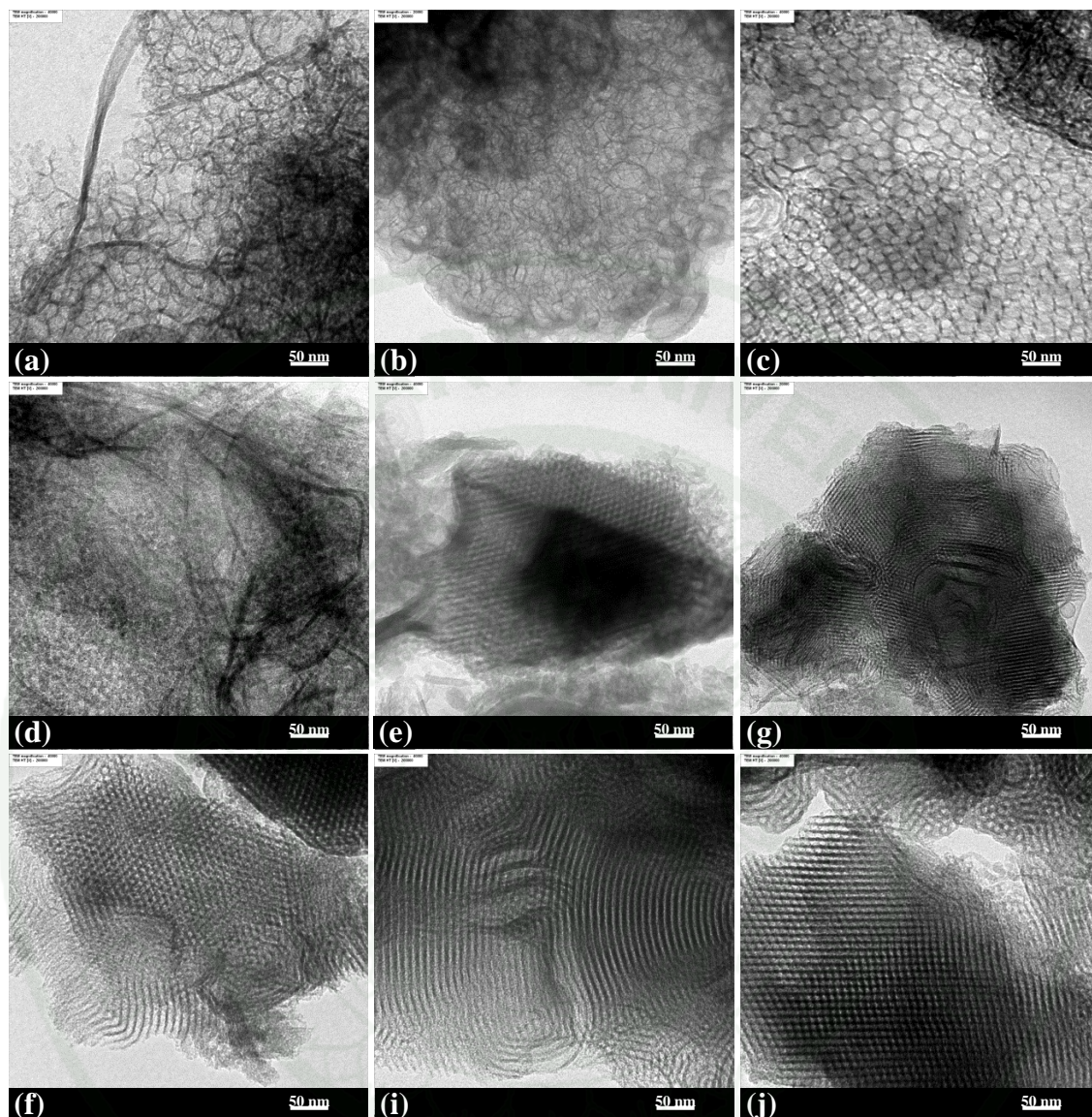


**Figure 26** TEM images of mesocellular silica with different sequences of TMB addition. (a) MS-1, (b) MS-2, (c) MS-3, (d) MS-4, (e) MS-5, (f) MS-6, (g) MS-7, (h) MS-8, and (i) MS-9.

## 2. Effect of nickel-carbon nanotubes/mesocellular silica composite catalysts on dry reforming reaction

### 2.1 Physical and chemical properties of catalyst without and with CNTs composite

Figure 27A shows nitrogen adsorption-desorption isotherm of MS support and catalyst without and with CNTs composite. It was found that MS support and all catalysts without and with CNTs composite exhibited type IV isotherm with H2 hysteresis loop, indicating the presence of mesoporous structure. From this result, it indicated that the existence of nickel metal and CNTs did not affect the pore structure of MS support. Considering the pore size distribution, MS support had the pore diameter in the range of 15-40 nm, resulting from pore expansion of SBA-15 by TMB as a swelling agent (Figure 27B). After nickel metal loading and CNTs synthesis, the mean pore diameters were slightly decreased to 15-35 nm. BET surface area and pore volume were calculated by using Brunauer-Emmett and Teller (BET) method and the results were shown in Table 11. BET surface area and pore volume were observed in the case of MS support, they were decreased with increasing the amount of nickel loading and CNTs composite due to the fact that nickel metal and CNTs could partially block the pores of MS supports.

XRD patterns of fresh catalysts without (reduced in H<sub>2</sub>) and with CNTs composite (unreduced in H<sub>2</sub>) are shown in Figure 28. It was found that all the catalysts (5Ni/MS and 10Ni/MS, and 5Ni-CNTs/MS and 10Ni-CNTs/MS catalysts) showed the diffraction pattern at 2θ of 44° and 52°, corresponding to metallic nickel phase (Jung et al., 1999 and Zhu et al., 2008). Nickel metal size was calculated by using Scherrer equation, as shown in Table 11. The nickel metal sizes of 5Ni/MS and 10Ni/MS catalysts were not significantly changed while the amount of nickel was increased because of the effect of nickel precursor (Li *et al.*, 2010). In this research, nickel (II) acetate which in general has relatively higher metal dispersion was used as the nickel metal precursor; therefore the smaller metal particle size was obtained. Nevertheless, after CNTs synthesis, nickel metal size of 5 wt. % loading was almost

not changed while larger metal size was observed with 10 wt. % because of the aggregation of nickel particles at high temperature. Furthermore, the diffraction peak at  $2\theta$  of  $26^\circ$  was observed in the catalysts with CNTs composite (Aiello *et al.*, 2000), indicating the presence of carbon on the surface of catalysts.

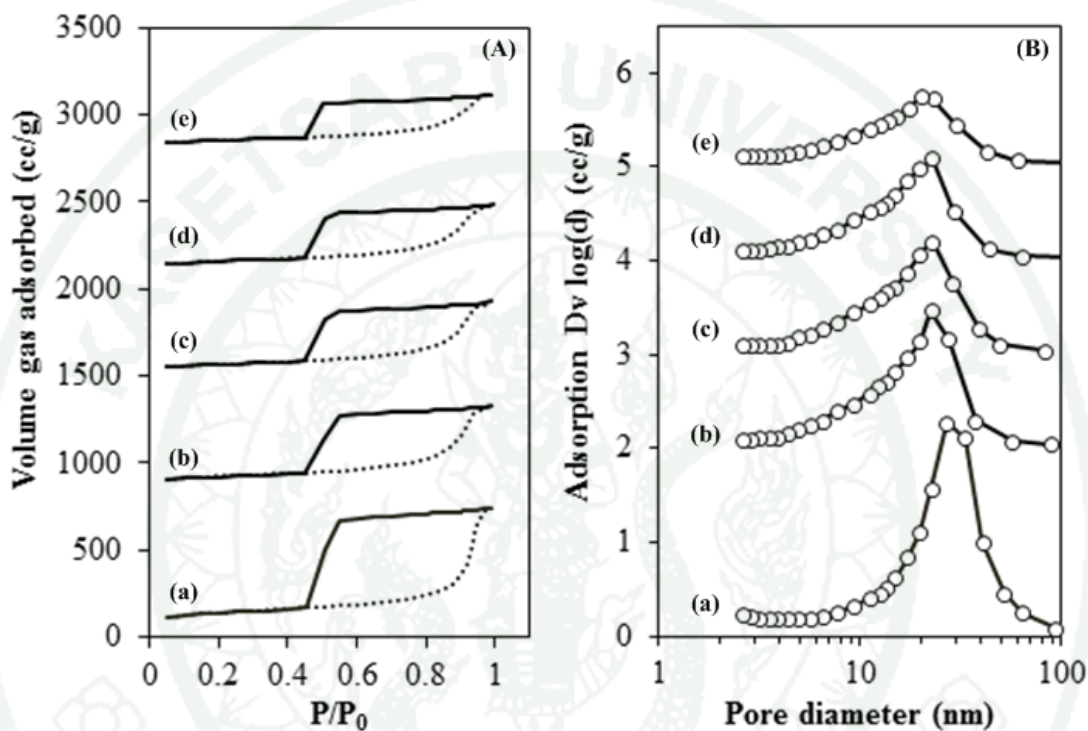


**Figure 27** (A) Nitrogen adsorption-desorption isotherm and (B) pore size distribution of MS support and catalysts. (a) MS, (b) 5Ni/MS, (c) 10Ni/MS, (d) 5Ni-CNTs/MS, (e) 10Ni-CNTs/MS

Figure 29 shows the morphologies of CNTs composite catalysts with different amount of nickel loading. The similar morphology of CNTs on MS support was observed in 5Ni-CNTs/MS and 10Ni-CNTs/MS catalysts. Moreover, various types of carbon allotropes with wide ranges of diameters were obviously found.

**Table 11** Textural properties of catalysts without and with CNTs composite, and amount of carbon on fresh catalysts

Samples	BET surface area (m <sup>2</sup> /g)	Pore volume (cm <sup>3</sup> /g)	Ni metal size <sup>a</sup> (nm)	Amount of carbon <sup>b</sup> (%)	Types of carbon (%)
					Amorphous, less-stable CNTs, CNTs
MS	474	1.15			
5Ni/MS	255	0.74	7.6	-	-
10Ni/MS	234	0.66	9.2	-	-
5Ni-CNTs/MS	210	0.60	6.9	12.14	0.69, 10.95, 0.50
10Ni-CNTs/MS	190	0.48	9.9	18.86	1.75, 13.64, 3.47

<sup>a</sup> Calculated from Scherrer equation

<sup>b</sup> Calculated from Thermogravimetric analysis

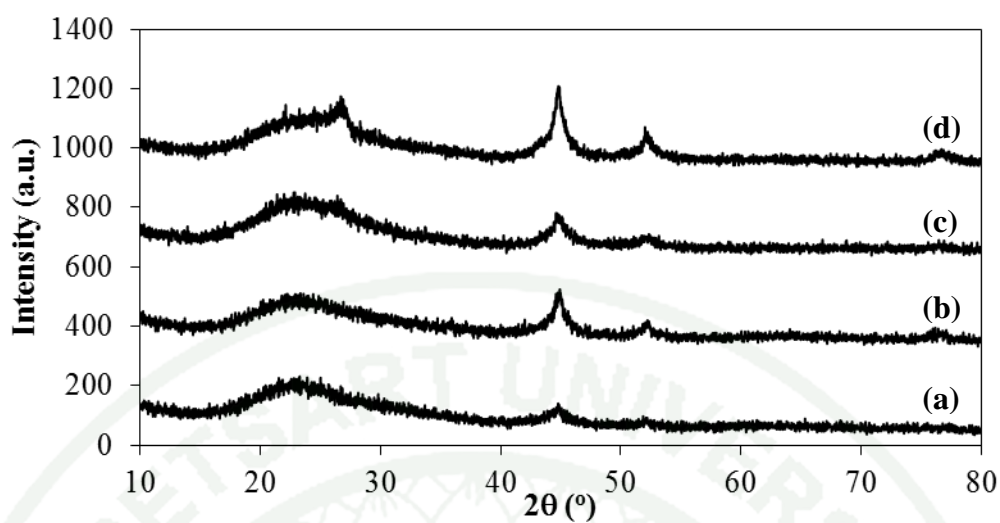


**Figure 28** XRD patterns of fresh catalysts. (a) 5Ni/MS, (b) 10Ni/MS, (c) 5Ni-CNTs/MS, (d) 10Ni-CNTs/MS

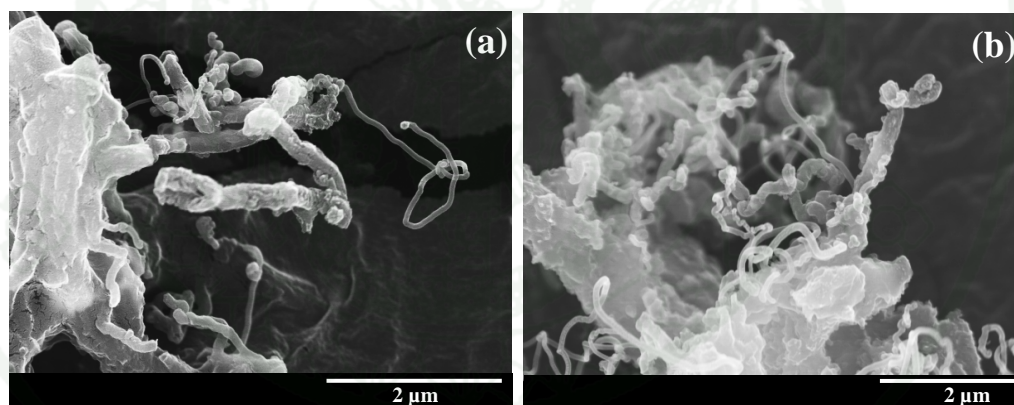


**Figure 29** FE-SEM images of fresh CNTs composite catalysts.

(a) 5Ni-CNTs/MS, (b) 10Ni-CNTs/MS

In order to investigate types of carbon allotropes, the composite catalysts were analyzed by using TGA-DTA technique, as shown in Figure 30. The curve of derivative weight loss showed four peaks of weight changes which could be classified into two temperature ranges (380-430°C and 430-720°C). The first peak at the temperature range of 380-430°C was attributed to the decomposition of amorphous

carbon (Hong *et al.*, 2006; Mathur *et al.*, 2008; Scheibe *et al.*, 2010). Other three peaks were observed at the temperature range of 430-720°C, indicating the presence of CNTs with wide range of diameters. Less-stable CNTs were easily decomposed at the temperature range of 430-650°C (Mathur *et al.*, 2008; Scheibe *et al.*, 2010). The last peak of at 650-720°C can be identified to CNTs with stable CNTs (Aiello *et al.*, 2000). The total amount of carbon in the composite catalysts was calculated by using TGA data in the temperature range between 380-720°C. The amounts of carbon on 5Ni-CNTs/MS and 10Ni-CNTs/MS catalysts were 12.14 wt.% and 18.86 wt.%, respectively, as the result shown in Table 11. Moreover, the amounts of CNTs (both less-stable and stable CNTs) on 5Ni-CNTs/MS and 10Ni-CNTs/MS catalysts were 11.45 wt.% and 17.11 wt.%, respectively.

The crystallinity of CNTs on composite catalyst was examined by using Raman spectroscopy (Figure 31). The D band (disorder carbon structure) and the G band (order carbon structure) were observed at 1335 cm<sup>-1</sup> and 1590 cm<sup>-1</sup>, respectively. The intensity of G band was almost the same as that of D band, indicating the existence of disorder graphite and amorphous carbon in the composite catalyst. Furthermore, this result implied that multi-walled carbon nanotubes (MWNTs) were selectively synthesized on Ni/MS catalysts because Raman spectra of MWNTs showed the similar ratio between G band and D band which high intensity of D band indicated higher quantity of structural defects in the CNTs due to their multiple graphite layers (Bai *et al.*, 2002; Scheibe *et al.*, 2010).

1943

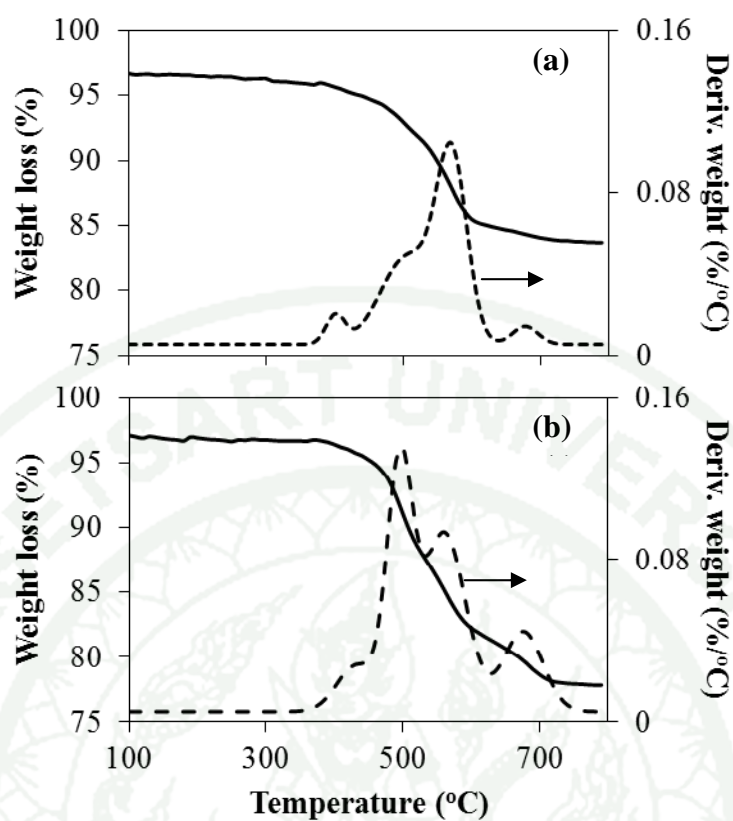


**Figure 30** TGA-DTA curves of fresh CNTs composite catalysts. (a) 5Ni-CNTs/MS, (b) 10Ni-CNTs/MS

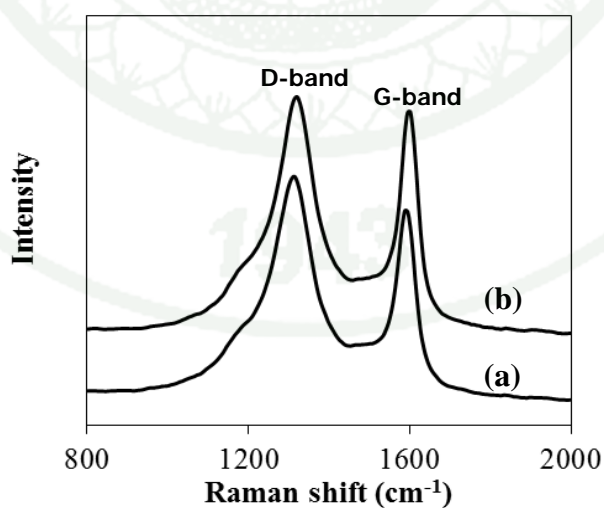


**Figure 31** Raman spectra of fresh CNTs composite catalysts. (a) 5Ni-CNTs/MS, (b) 10Ni-CNTs/MS.

## 2.2 Catalyst performance in dry reforming reaction

The performance of CNTs composited with nickel and mesocellular silica catalysts on carbon dioxide reforming of methane reaction under atmospheric pressure were investigated at 650°C for 24 h in a packed bed reactor. In the case of Ni-CNTs/MS catalysts, the composite catalysts were not reduced with H<sub>2</sub> prior to the reaction due to the fact that nickel particles on Ni-CNTs/MS catalysts were completely changed to metallic nickels (active nickel) during CNTs synthesis process as was confirmed by the XRD patterns shown in Figure 28.

Figure 32 shows the time profile of methane (a) and carbon dioxide (b) conversions of the catalysts without and with CNTs composite. It was found that the catalysts with CNTs composite (5Ni-CNTs/MS and 10Ni-CNTs/MS) exhibited lower CO<sub>2</sub> and CH<sub>4</sub> conversions than that of without CNTs (5Ni/MS and 10Ni/MS) due to their lower amounts of active nickel metal on the CNTs composite catalysts compared to that of without CNTs. This could be attributed to the surface coverage of active nickel metals by CNTs formation (mainly tip-growth mechanism) (Jong et al., 2007; Harris 2009). As shown in Figures 32a and b, it was found that without CNTs, the amounts of nickel (5 and 10% loading) did not affect methane and carbon dioxide conversions, whereas a relatively larger difference was observed with CNTs composite catalysts due to nickel surface coverage by CNTs. Moreover, CH<sub>4</sub> and CO<sub>2</sub> conversions of CNTs composite catalysts were slightly increased with increasing time on stream (3% increased at 24-h time on stream), whereas those of without CNTs were gradually decreased (10% decreased at 24-h time on stream).

The turnover frequencies (TOFs) after 24-h time on stream of 10Ni/MS and 10Ni-CNTs/MS catalysts are compared (inset of Figures 32a-b) based on the same amount of active nickel metals. It was found that 10Ni-CNTs/MS catalyst gave significantly higher TOFs of both methane and carbon dioxide than those of 10Ni/MS catalyst. This result clearly indicated that nickel composited with CNTs could improve the catalyst stability during dry reforming reaction.

It was found that H<sub>2</sub>/CO ratio obtained from the catalyst without CNTs was lower than that of with CNTs (Figure 32c). This lower H<sub>2</sub>/CO ratio obtained from the catalysts without CNTs implied the occurrence of reverse water-gas shift (RWGS) reaction of which hydrogen product was consumed through the side reaction as shown in Eq. 26 (Sousa *et al.*, 2012; Ma *et al.*, 2013).

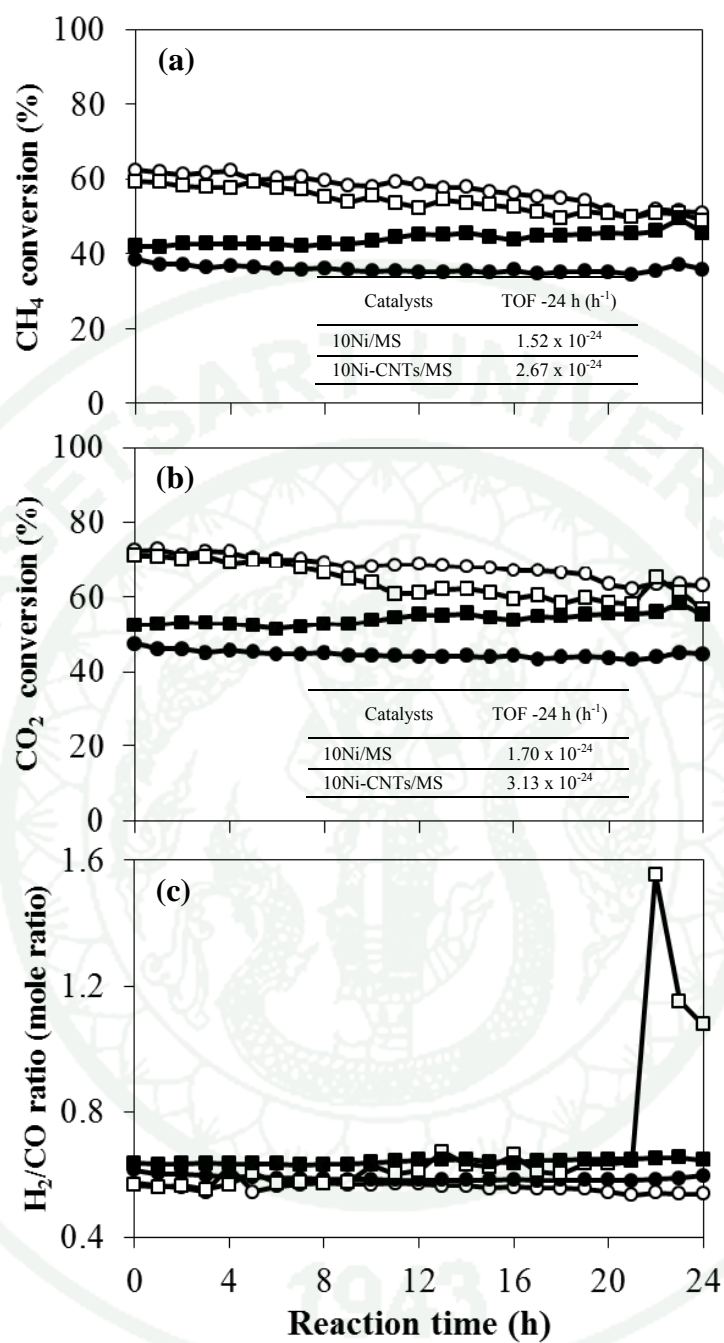


In order to investigate types of carbon affecting carbon dioxide reforming of methane, Ni-CNTs/MS composite catalysts were reduced with H<sub>2</sub> in order to remove unstable carbon prior to the reaction. As shown in Figure 33A, the derivative weight loss curves of amorphous carbon (380-430°C) and less-stable CNTs (430-650°C) were significantly decreased, while stable CNTs (650-720°C) was almost not changed after reduced with H<sub>2</sub>.

The FE-SEM images of unreduced (Figure 29) and reduced CNTs composite catalysts (Figure 33B) also clearly confirmed the disappearance of amorphous carbon and less-stable CNTs. After reduction with H<sub>2</sub>, CNTs with smaller size were mainly observed.

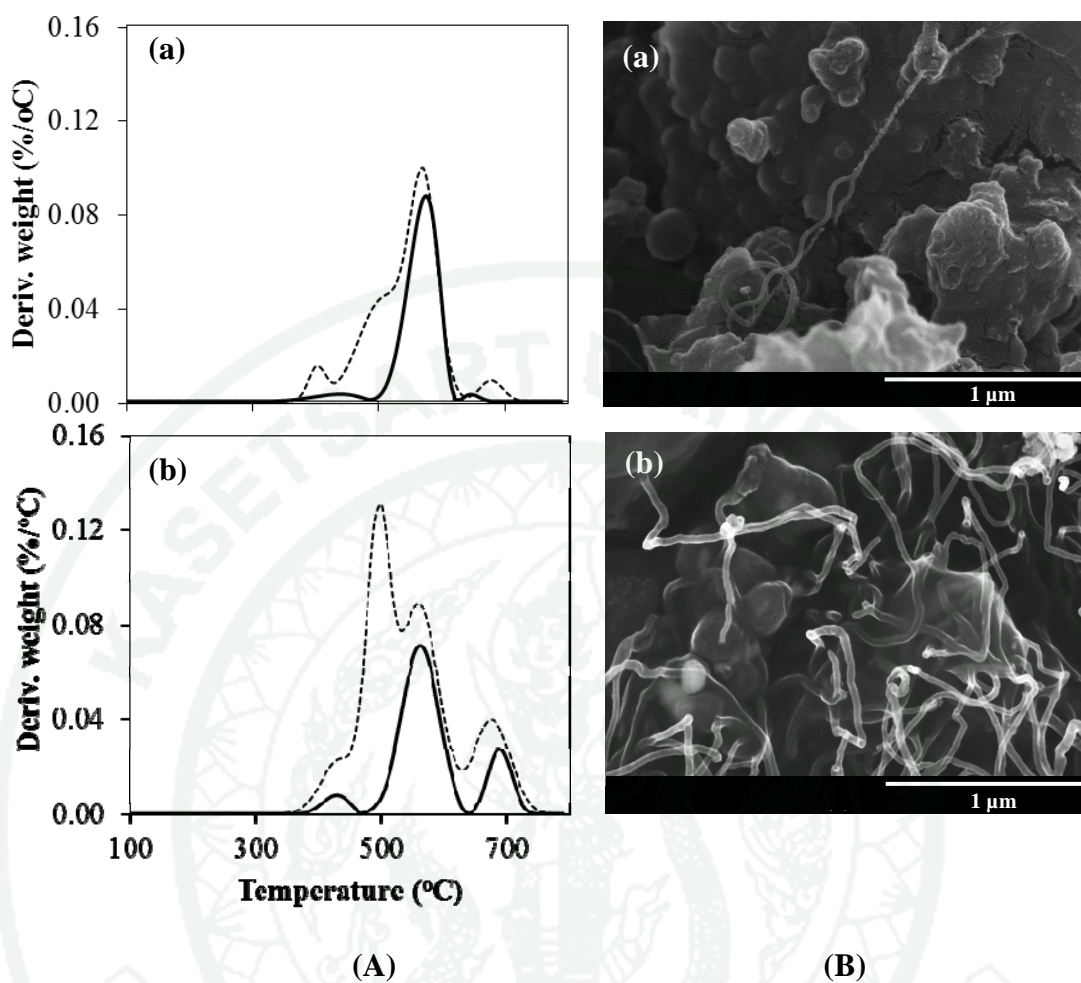
The disappearance of amorphous carbon and less-stable CNTs on composite catalysts can be explained through methane cracking reaction (Eq. 27) (Fan *et al.*, 2009).





**Figure 32** Performances of catalysts without and with CNTs composite with time on stream in dry reforming reaction at 650°C for 24 h. (a) CH<sub>4</sub> conversion, (b) CO<sub>2</sub> conversion, (c) H<sub>2</sub>/CO mole ratio

○ 5Ni/MS, □ 10 Ni/MS, ● 5Ni-CNTs/MS, ■ 10Ni-CNTs/MS



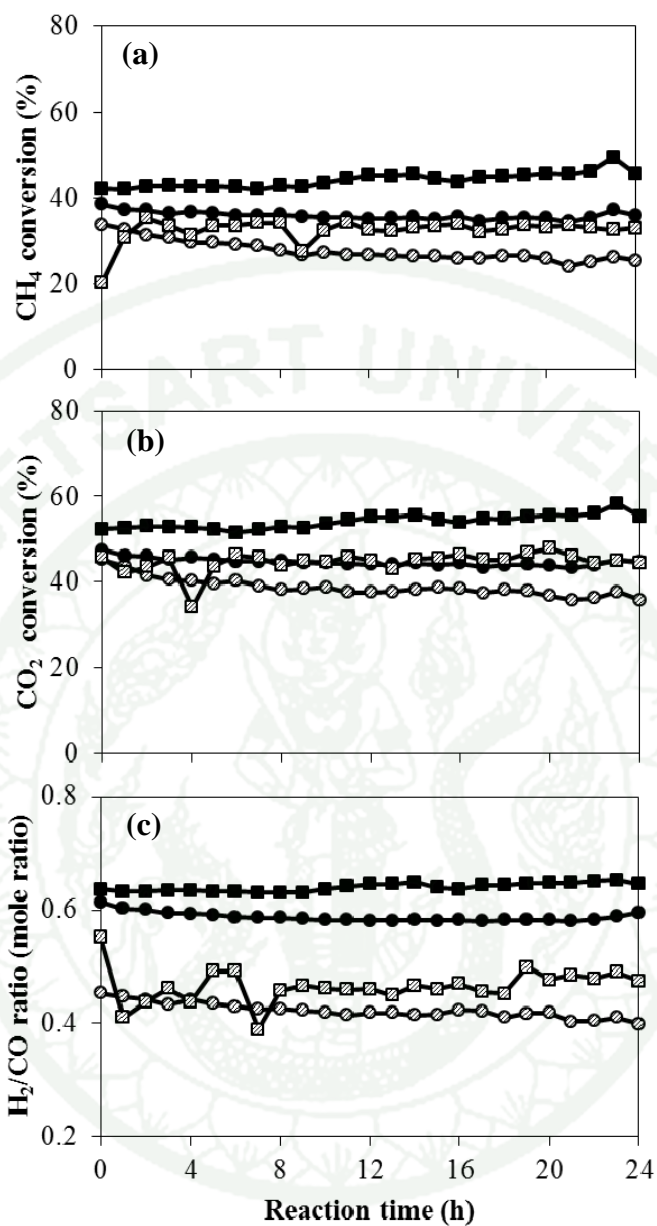
**Figure 33** (A) TGA-DTA curves of unreduced (dashed line) and reduced (solid line) catalysts and (B) FE-SEM images of reduced CNTs composite catalysts. (a) 5Ni-CNTs/MS (reduced), (b) 10Ni-CNTs/MS (reduced)

Figure 34 shows the time profile of methane (a) and carbon dioxide (b) conversions over unreduced and reduced CNTs composite catalysts. As shown in Figure 34a and b, the unreduced CNTs composite catalysts (5Ni-CNTs/MS and 10Ni-CNTs/MS) show relatively higher CH<sub>4</sub> and CO<sub>2</sub> conversions compared to those of reduced catalysts (5Ni-CNTs/MS (reduced) and 10Ni-CNTs/MS (reduced)). This result could be attributed to the difference in types of carbons between the unreduced and reduced CNTs composite catalysts (fresh catalysts). In the case of unreduced

CNTs composite catalyst, amorphous carbon and less-stable CNTs (larger size) were still remained on the catalyst surface. However, in the case of reduced CNTs composite catalyst, amorphous carbon was disappeared while the amounts of less-stable CNTs were reduced (as shown in Figure 33A and B). This result therefore indicated that types of carbons have a significant effect on the catalyst performance. As the unreduced CNTs composite catalysts exhibited higher catalyst performance in dry reforming reaction, it implied that amorphous carbon and less-stable CNTs could therefore enhance methane and carbon dioxide conversions in some extent.

Moreover, it was found that the  $H_2/CO$  ratios of the reduced CNTs composite catalysts were lower than those of the unreduced one (Figure 34c), indicating the inhibition of RWGS reaction caused by the existence of amorphous carbon and less-stable CNTs. However, it should be noted that with the CNTs composite, the stability of catalysts have been prolonged compared to that of the conventional catalysts (Ni/MS catalyst).

In order to examine the deactivation phenomena of the catalysts after reaction, the used catalysts were analyzed by using XRD as the result shown in Figure 35. The diffraction peaks of carbon and nickel metal were found in all catalysts at  $2\theta$  of  $26^\circ$  and  $42^\circ$ , and  $44^\circ$  and  $52^\circ$ , respectively. It should be noted that nickel metal size slightly increased after dry reforming reaction (Table 12) due to sintering of nickel. However, it was clearly seen that Ni metal sizes after reaction were quite similar in all cases; this result indicated that carbon formation therefore principally affected the catalyst deactivation.



**Figure 34** Performances of unreduced and reduced CNTs composite catalysts with time on stream in dry reforming reaction at 650°C for 24 h.

(a) CH<sub>4</sub> conversion, (b) CO<sub>2</sub> conversion, (c) H<sub>2</sub>/CO mole ratio

● 5Ni-CNTs/MS                      ■ 10 Ni-CNTs/MS  
 ○ 5Ni-CNTs/MS (reduced)        □ 10Ni-CNTs/MS (reduced)

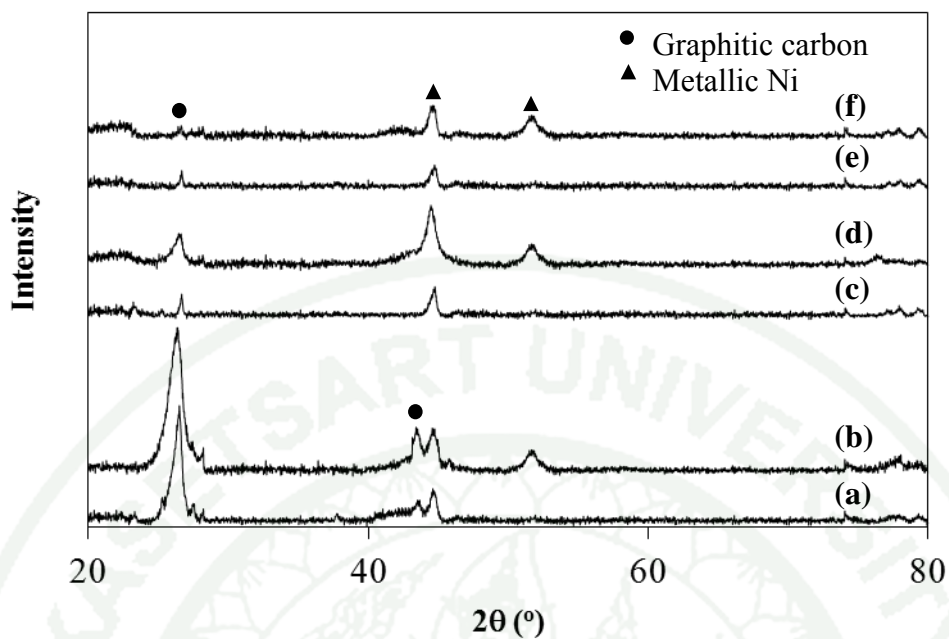


**Figure 35** XRD patterns of catalysts after dry reforming reaction at 650°C for 24 h.

- (a) 5Ni/MS-used, (b) 10Ni/MS-used,  
 (c) 5Ni-CNTs/MS-used, (d) 10Ni-CNTs/MS-used,  
 (e) 5Ni-CNTs/MS(reduced)-used, (f) 10Ni-CNTs/MS(reduced)-used

**Table 12** Nickel metal size of catalyst after dry reforming reaction

Catalysts	Ni metal size <sup>a</sup> (nm)
5Ni/MS-used	15.1
10Ni/MS-used	12.6
5Ni-CNTs/MS-used	14.1
10Ni-CNTs/MS-used	10.6
5Ni-CNTs/MS(H <sub>2</sub> )-used	15.1
10Ni-CNTs/MS(H <sub>2</sub> )-used	14.8

<sup>a</sup> Calculated from Scherrer equation

### 2.3 Characterization of used catalysts after dry reforming reaction

TGA-DTA was used to analyze types of carbon formed on Ni/MS and Ni-CNTs/MS catalysts after dry reforming reaction at 650°C for 24 h and the results are shown in Figure 36. As the catalysts were mixed with inert sand prior to each dry reforming experiment, only the qualitative data regarding the types of carbon were examined. Considering the catalyst without CNTs, the change in derivative weight loss curve at the temperature range of 550-650°C could be attributed to the decomposition of carbon nanofibers (CNFs). This result was in good agreement with the works reported by Kumar *et al.* (2007) and Ghosh *et al.* (2008). It should be noted that the decomposition of less-stable CNTs also occurred within the same range of temperature (430-650°C).

In the case of catalysts with CNTs composite (unreduced and reduced), the change in derivative weight loss was observed in the same temperature range. This indicated that CNFs also occurred on composite catalysts after dry reforming reaction. Comparing the relative amount of carbons on CNTs composite catalyst before and

after reaction, it was found that the amount of amorphous carbon (380-430°C) was decreased whereas that of stable CNTs (650-720°C) was quite constant. In the temperature range of 430-650°C, the relative amount of less-stable CNTs (CNTs of larger size) and CNFs was increased due to CNFs formation after dry reforming reaction.

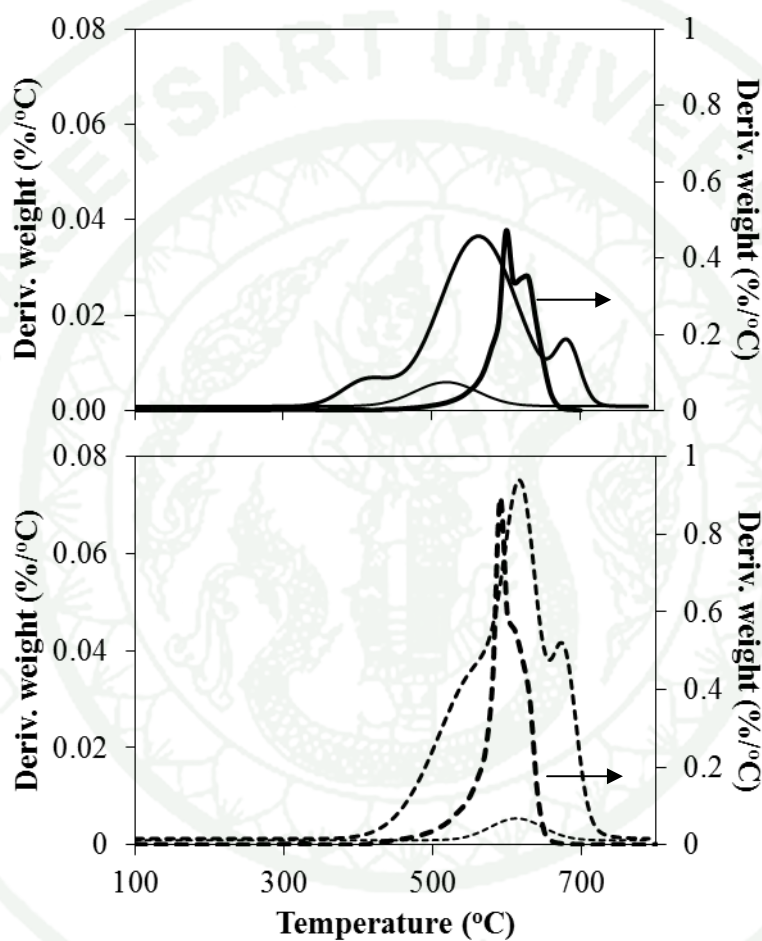


**Figure 36** TGA-DTA curves of catalysts after dry reforming at 650°C for 24 h.

- |   |                            |           |                             |
|---|----------------------------|-----------|-----------------------------|
| — | 5Ni/MS-used                | - - -     | 10Ni/MS-used                |
| — | 5Ni-CNTs/MS-used           | · · ·     | 10Ni-CNTs/MS-used           |
| — | 5Ni-CNTs/MS (reduced)-used | · · · · · | 10Ni-CNTs/MS (reduced)-used |

In order to examine the crystallinity of carbon formed on the catalysts after reaction, the catalysts were analyzed using Raman spectroscopy, as shown in Figure 37. The relative intensity of D band and G band was the highest in the case of

the catalysts without CNTs. This result indicated the existence of carbon products with low graphitization due to the characteristics of CNFs on Ni/MS catalysts (Teo *et al.*, 2003). Although CNFs occurred on the catalysts with CNTs composite (unreduced and reduced), the relative intensities of D band and G band were different from the catalyst without CNTs. The intensity of G band was almost the same as D band in the case of unreduced catalysts with CNTs composite, indicating the existence of stable CNTs with high order of graphitization. Moreover, in the case of the reduced catalysts with CNTs composite, the intensity of G band was the highest. This could be attributed to the majority of carbon on the composite catalysts containing CNTs with high order of graphitization.

The morphology of catalysts after reaction was observed by FE-SEM images. It was found that the CNFs growth positions on Ni/MS and Ni-CNTs/MS catalysts were different. In the case of Ni/MS catalysts, CNFs formed and blocked the active Ni over MS support (Figure 38a-b), leading to lowering the performance of Ni/MS catalyst (Figure 32). On contrary, in the case of Ni-CNTs/MS catalysts (unreduced and reduced), carbon formation was selectively extended at the active interface between nickel and coexisted CNTs primarily formed by CCVD technique as an extension of CNTs tube length (Figure 38c-f). Moreover, it was found that CNFs with different sizes were also observed on the unreduced and reduced CNTs composite catalysts. During the reaction, small parts of nickel metal could possibly separate from nickel cluster, and further activate carbon formation in the form of less stable CNTs and CNFs, and resulting in the formation of CNFs (with smaller size of metal on tips) on CNTs. As a result, the activity of the CNTs composite catalysts was quite stable throughout the period of study.

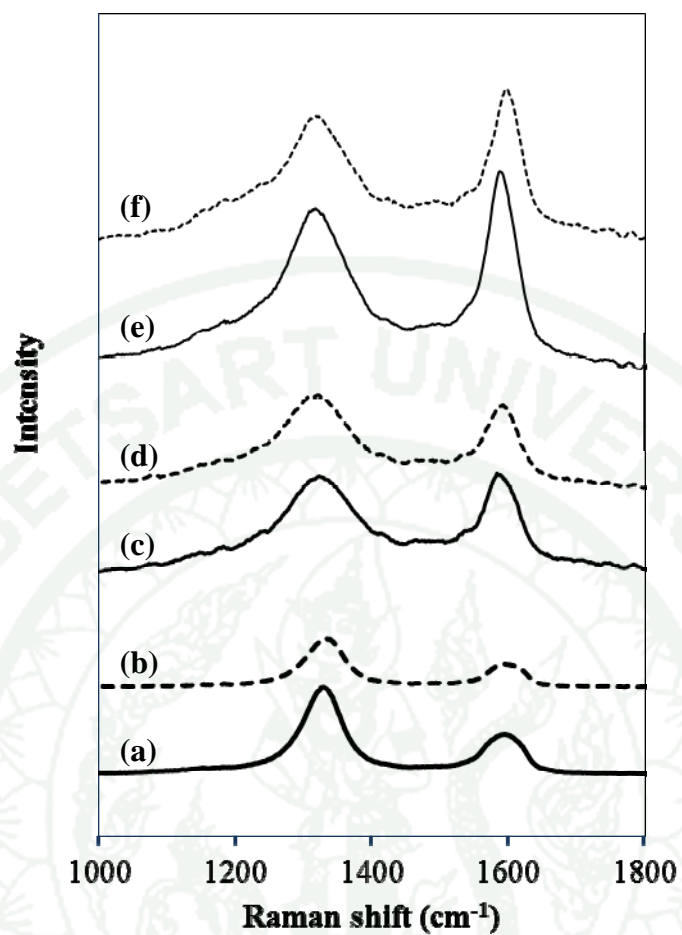


**Figure 37** Raman spectra of catalysts after dry reforming at 650°C for 24 h.

- |                                |                                 |
|--------------------------------|---------------------------------|
| (a) 5Ni/MS-used                | (b) 10Ni/MS-used                |
| (c) 5Ni-CNTs/MS-used           | (d) 10Ni-CNTs/MS-used           |
| (e) 5Ni-CNTs/MS (reduced)-used | (f) 10Ni-CNTs/MS (reduced)-used |

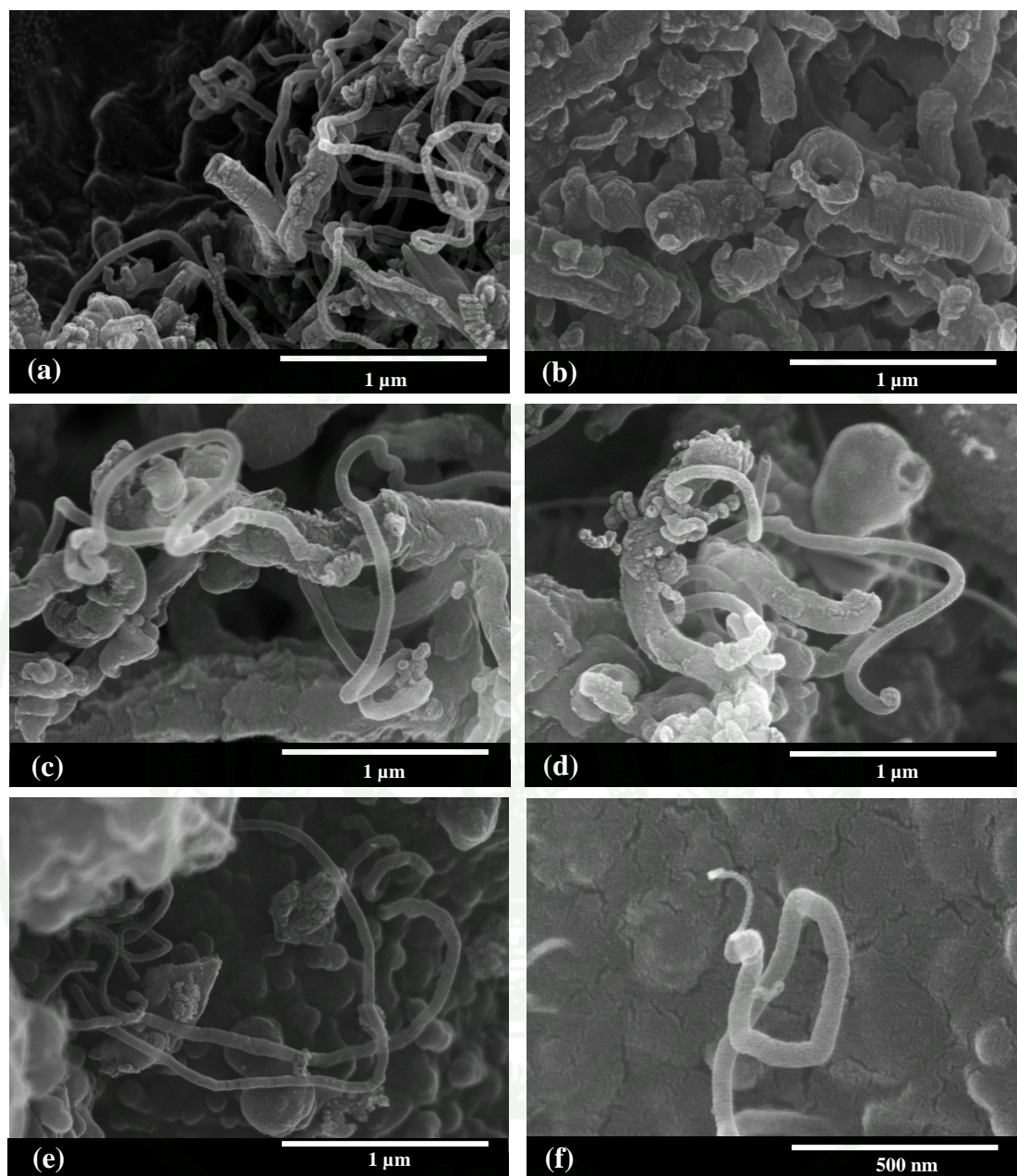


**Figure 38** FE-SEM images of catalysts after dry reforming at 650°C for 24 h.

- |                                 |                                  |
|---------------------------------|----------------------------------|
| (a) 5Ni/MS-used,                | (b) 10Ni/MS-used,                |
| (c) 5Ni-CNTs/MS-used,           | (d) 10Ni-CNTs/MS-used,           |
| (e) 5Ni-CNTs/MS (reduced)-used, | (f) 10Ni-CNTs/MS (reduced)- used |

#### 2.4 Proposed mechanism of selective carbon formation on catalysts

The different types of carbon formed were observed in TEM images of fresh and used catalysts without and with CNTs composites (both unreduced and reduced) as shown in Figure 39 (a, c, and e) and (b, d, and f), respectively.

For Ni/MS catalysts, CNFs were formed and partially covered the surface of active nickels (Figure 39b), leading to slightly decrease of the catalyst performance. On contrary, in the case of Ni-CNTs/MS catalysts both unreduced and reduced with H<sub>2</sub>, the carbon products were selectively formed as the tube-length extension of the existing CNTs following the tip-growth mechanism (Figure 39d and f). As a result, carbon formation caused by methane cracking reaction then had no effect on losses of active Ni species and the stability of these composite catalysts was then evidently maintained during 24-h time on stream.

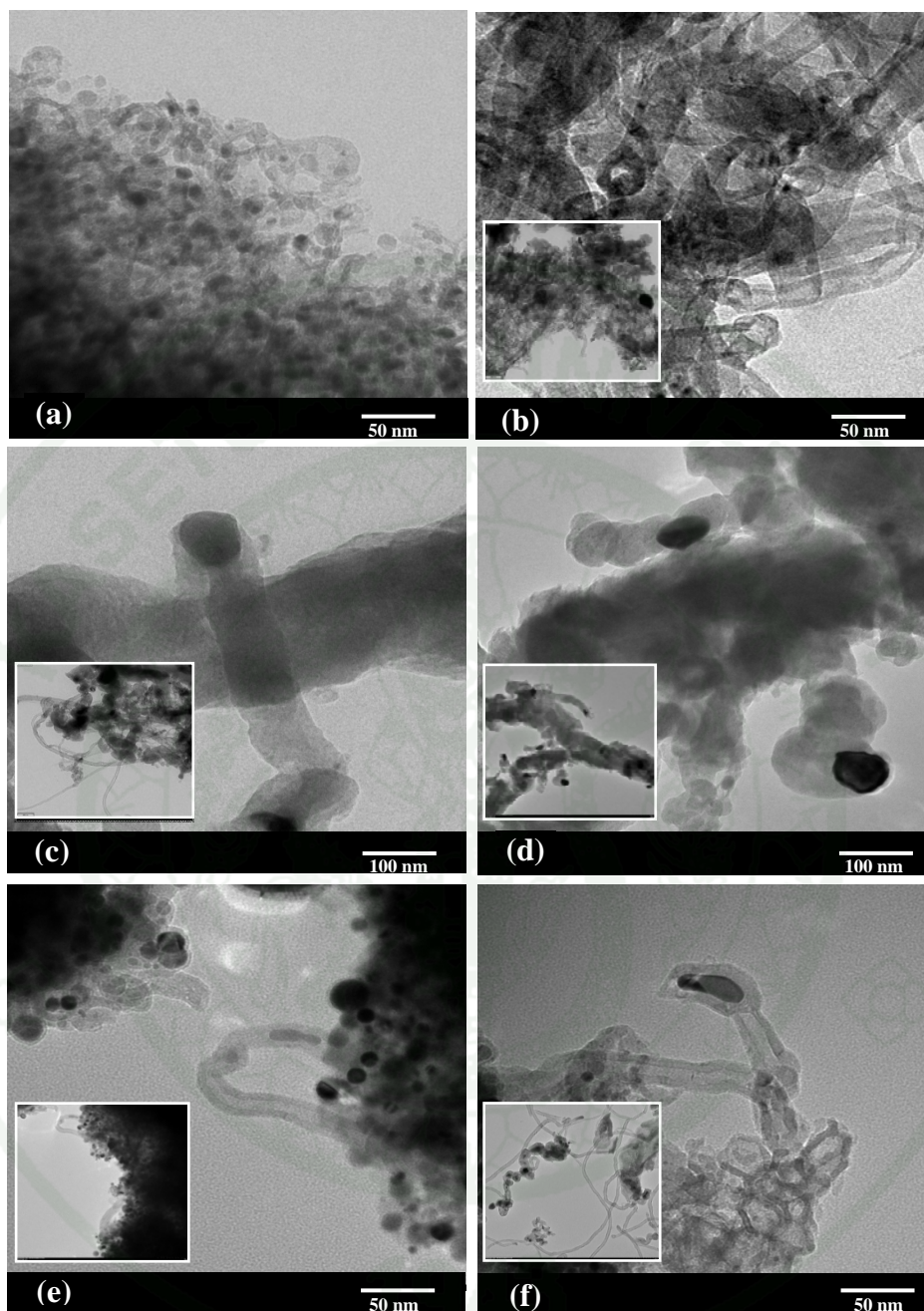


**Figure 39** TEM images of catalysts before and after dry reforming at 650°C for 24 h.

- |                                   |                                 |
|-----------------------------------|---------------------------------|
| (a) 10Ni/MS-fresh,                | (b) 10Ni/MS-used,               |
| (c) 10Ni-CNTs/MS-fresh,           | (d) 10Ni-CNTs/MS-used,          |
| (e) 10Ni-CNTs/MS (reduced)-fresh, | (f) 10Ni-CNTs/MS (reduced)-used |

Consequently, the mechanism of selective carbon formation on Ni/MS and Ni-CNTs/MS catalysts during dry reforming reaction were proposed based on the above result, as shown in Figure 40. With Ni/MS catalyst (Figure 40a), after 24-h time on stream the catalyst was deactivated by CNFs formation of which partially covered and blocked the surface of active nickels.

It should be mentioned that CNTs composites were synthesized by CCVD method of which known as the method for CNTs synthesis. Based on this method, acetylene decomposition took place over active nickel metals and carbon radicals were consecutively transferred through nickel to the active interfaces between nickel and mesocellular silica support where CNTs formation took place. As a result, CNTs were then formed and continuously lifted up nickel metal clusters following the tip-growth mechanism.

When CNTs composite catalysts were used in dry reforming reaction, active nickel metals were not deactivated even though nickel itself activated the carbon formation reaction. It was proposed that carbon formation mechanism occurred following the CCVD method of which was the same method for CNTs synthesis (Figure 40b). In this case, carbon formation selectively took place on the active interface between nickel and coexisted CNTs following the tip-growth mechanism, and simultaneously lifted up the nickel metal clusters as the CNTs were grown up, leading to better catalyst stability in dry reforming reaction.

1943

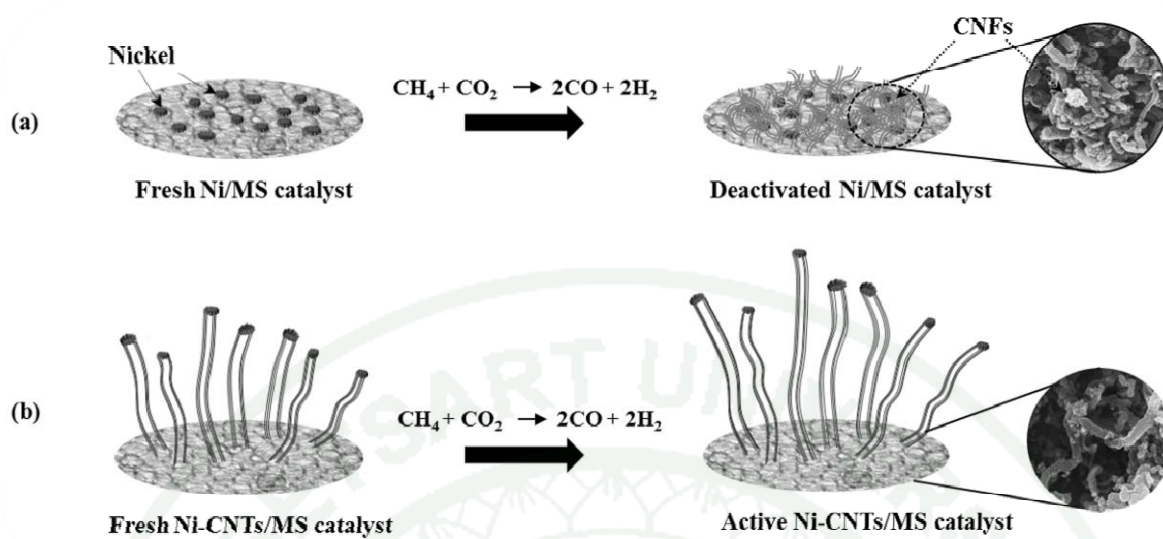


**Figure 40** Proposed schemes of different carbon formation mechanisms during dry reforming reaction leading to (a) deactivation of Ni/MS catalysts by coke deposition (b) prolonging stability of Ni-CNTs/MS catalysts by selective extension of CNT tube length.

### 3. Effect of nickel-carbon nanofibers-mesocellular silica composite catalyst on phenylacetylene hydrogenation reaction

#### 3.1 Physical and chemical properties of catalyst without and with CNFs composite

Figure 41A shows nitrogen adsorption-desorption isotherms of mesocellular silica (MS) support, Ni/MS, and Ni-CNFs/MS composites with different CNFs synthesis time periods. All the samples show type IV isotherm with H2 hysteresis loop, indicating the existence of mesopore structure. This result indicated that nickel metal and CNFs did not affect the structure of MS support. Considering pore diameter, MS support exhibited pore diameter in the range of 15-35 nm (Figure 41B). Moreover, all the catalysts revealed the similar range of pore diameter to that of the MS support but their peaks intensity were consecutively decreased after nickel loading and the increases of CNFs synthesis time periods. BET surface area and pore volume calculated by Brunauer-Emmett-Teller (BET) method area shown in Table 13. MS support has the highest specific surface area and pore volume of 535 m<sup>2</sup>/g and 1.36 cm<sup>3</sup>/g, respectively. BET surface area was significantly decreased after nickel loading onto the MS support due to the blockage of nickel particles in the MS pores. In the case of Ni-CNFs composite catalyst, BET surface area and pore volume were also decreased because of the growth of CNFs inside and over the surface of MS support.

XRD patterns of fresh catalysts without and with CNFs composite are shown in Figure 42. It was found that all catalyst exhibited the diffraction patterns at 2θ of 44° and 52° corresponded to the metallic nickel (1 1 1) and (2 0 0) (Richardson *et al.*, 2003; Chen *et al.*, 2009; Zeng *et al.*, 2012). Moreover, nickel metal size was calculated by Scherer equation, as the result shown in Table 13. It was found that nickel metal size increased with increasing CNFs synthesis time periods due to the aggregation of nickel metal clusters during the CCVD process caused by relatively high synthesis temperature. Furthermore, the diffraction peak of graphitic carbon (0 0 2) at 2θ of 25° (Kim *et al.*, 2009) was observed in the Ni-CNFs composite catalysts.

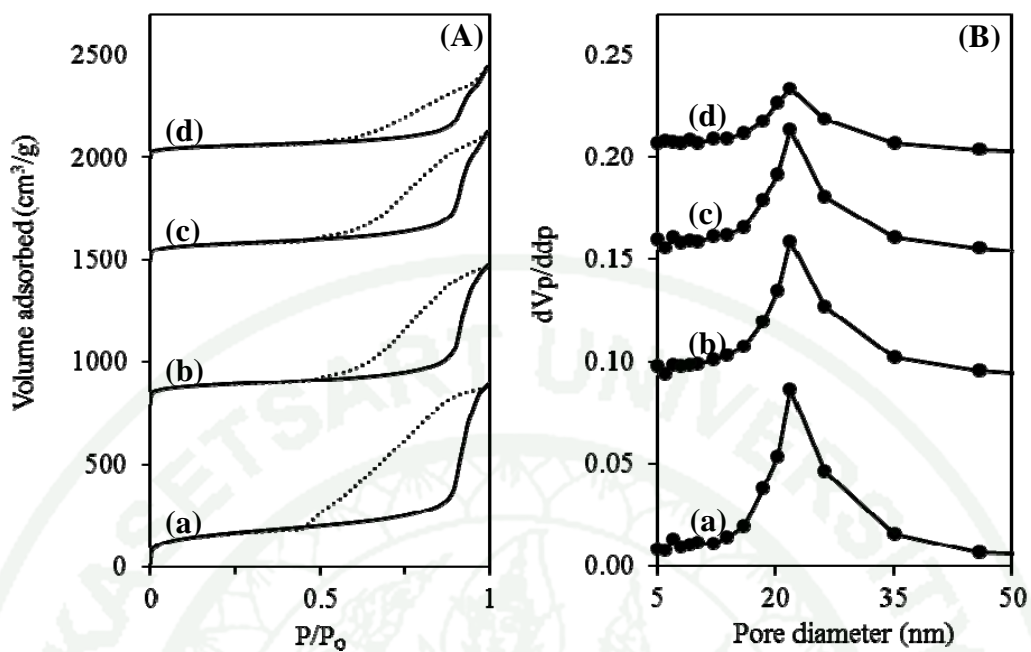


**Figure 41** (A) Nitrogen adsorption-desorption isotherm and (B) pore size distribution of mesoporous silica support and catalysts.

(a) MS, (b) Ni/MS, (c) Ni-CNFs(1)/MS, and (d) Ni-CNFs(3)/MS

**Table 13** BET surface area, pore volume and average nickel metal size of catalysts

Catalysts	BET surface area (m <sup>2</sup> /g)	Pore volume (cm <sup>3</sup> /g)	Ni metal size <sup>a</sup> (nm)
MS	535	1.36	
Ni/MS	299	1.13	19.29
Ni-CNFs(1)/MS	264	0.96	21.77
Ni-CNFs(3)/MS	194	0.67	26.53

<sup>a</sup> Calculated from Scherrer equation

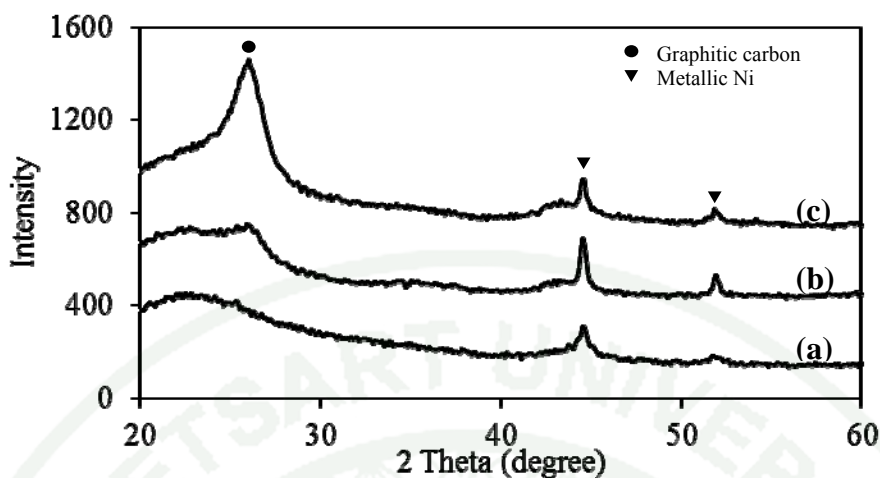


**Figure 42** XRD patterns of fresh catalysts after reduced with H<sub>2</sub> gas at 500°C.  
 (a) Ni/MS, (b) Ni-CNFs(1)/MS, and (c) Ni-CNFs(3)/MS

Figure 43 shows the weight loss curves of CNFs composite catalysts with different CNFs synthesis time periods. It was found that the weight loss below 400°C was attributed to moisture content in the catalyst, while weight loss in the temperature range of 400-570°C indicated the decomposition of CNFs (Dussault *et al.*, 2007; Romero *et al.*, 2007). Moreover, the amount of CNFs on the composite catalysts was evaluated by using thermogravimetric analysis (TGA) technique, as the result shown in Table 14. The amount of CNFs on Ni-CNFs(1)/MS and Ni-CNFs(3)/MS catalysts were 13.4 and 54.5 wt. %, respectively, indicating the CNFs obtained were increased with increasing synthesis time.

The crystallinity of CNFs on the composite catalysts was analyzed by using Raman spectroscopy, as shown in Figure 44. The D-band around 1340 cm<sup>-1</sup> was corresponding to disorder and defect of carbon structure, and the existence of amorphous carbon (Sano *et al.*, 2014) where the G-band around 1570 cm<sup>-1</sup> was attributed to graphitic carbon (Sano *et al.*, 2014). It was found that the relative intensity between the D band and the G band of Ni-CNFs(1)/MS catalyst was quite similar to that of Ni-CNFs(3)/MS catalyst, it means that the characteristics of CNFs did not change when CNFs synthesis time periods was increased.

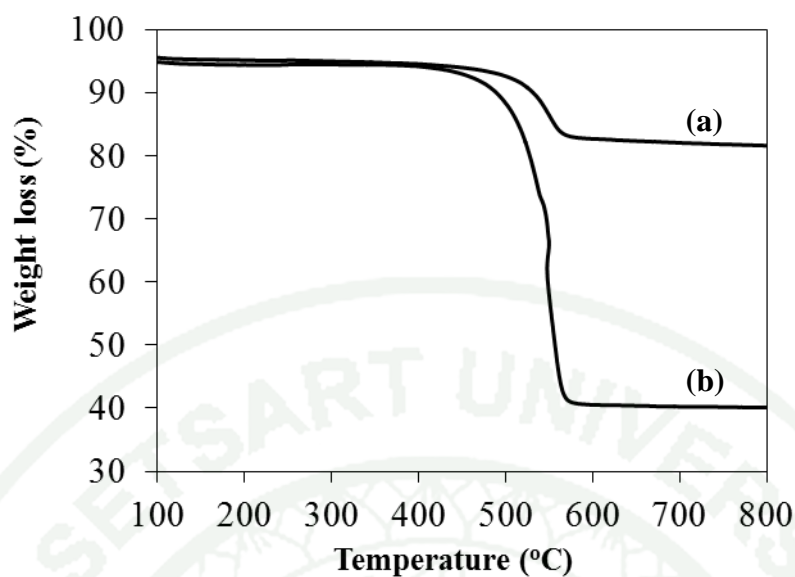


**Figure 43** Weight loss of fresh catalysts.

(a) 10Ni-CNFs(1)/MS and (b) 10Ni-CNFs(3)/MS

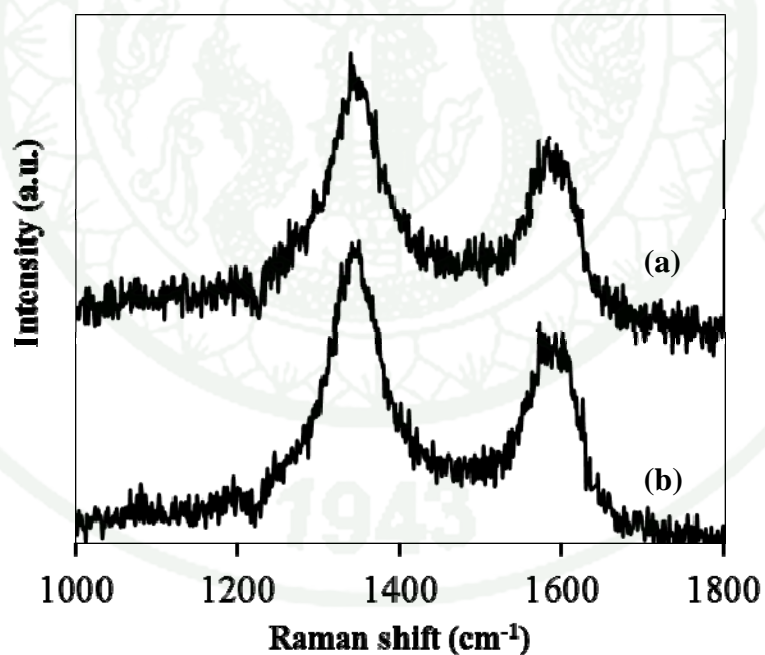


**Figure 44** Raman spectra of fresh catalysts.

(a) 10Ni-CNFs(1)/MS and (b) 10Ni-CNFs(3)/MS

CNFs composite catalyst structure was observed by using TEM image. CNFs with different diameters were grown from the surface MS support and

continuously lifted up nickel metal clusters from the support following the tip-growth mechanism of CNFs synthesis (Abild-Pedersen et al., 2006 and Jong et al., 2007), as shown in Figure 45.

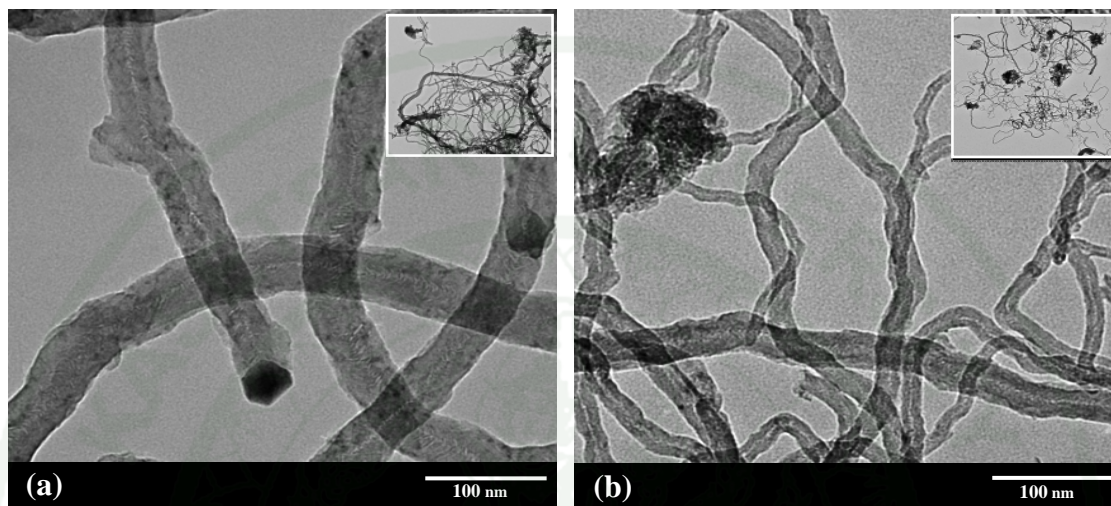


**Figure 45** TEM images of fresh catalysts.

(a) Ni-CNFs(1)/MS and (b) Ni-CNFs(3)/MS

The surface hydrophobicity of catalysts was evaluated by using water adsorption technique at 298 K. The relative amount of adsorbed water was calculated from the amount of water adsorbed at  $P/P_0 = 0.5$  (Table 14). The relative amount of adsorbed water was  $0.40 \text{ cm}^3/\text{m}^2$  for Ni/MS catalyst, while it was  $0.27 \text{ cm}^3/\text{m}^2$  for Ni-CNFs(3)/MS catalyst. The amount of water adsorbed was decreased after modification of Ni/MS by CNFs, showing the clear effect of CNFs modification on the improvement of surface hydrophobicity. This result indicated that the hydrophobicity of Ni-CNFs(3)/MS was approximately 1.5 times higher than that of the catalyst without CNFs (Table 14).

**Table 14** Amount of carbon, hydrophobicity, product selectivities, and turnover frequency (TOF) of catalysts in phenylacetylene hydrogenation

Catalysts	Amount of carbon (%)	Amount of adsorbed water (cm <sup>3</sup> /m <sup>2</sup> )	Hydrophobicity <sup>a</sup>	Selectivity <sup>b</sup> (%)		Ni active atom x10 <sup>18</sup> (atoms)	TOF <sup>c</sup> x10 <sup>-22</sup> (h <sup>-1</sup> )
				S	EB		
Ni/MS	-	0.40	1.0	89.6	10.4	6.14	0.82
Ni-CNFs(1)/MS	13.4	0.38	1.1	91.8	8.2	4.23	1.22
Ni-CNFs(3)/MS	54.5	0.27	1.5	91.6	8.4	1.42	2.59

<sup>a</sup> Calculated as a ratio of reverse proportion of amount of adsorbed water based on that of 10Ni/MS catalyst

<sup>b</sup> Calculated at 60% of PA conversion

<sup>c</sup> Calculated from TOF = (% conversion x mole of reactant) / (time x active atom of Ni at surface)

### 3.2. Performance of Ni-CNFs/MS catalysts on phenylacetylene hydrogenation

The catalyst performance was investigated through liquid-phase phenylacetylene hydrogenation under atmospheric pressure of hydrogen in the semi-batch glass reactor for 3 h. Phenylacetylene was hydrogenated to styrene and consecutively converted to ethylbenzene as a byproduct. Phenylacetylene conversions of Ni-CNFs composite catalysts (Ni-CNFs(1)/MS and Ni-CNFs(3)/MS) were compared with that of Ni/MS catalyst, as shown in Figure 46a, b, and c. With increasing the reaction time, phenylacetylene conversions of all catalysts were increased. It was found that Ni-CNFs(1)/MS composite catalyst exhibited the highest phenylacetylene conversion of 90.8 %, while Ni-CNFs(3)/MS composite catalyst gave the lowest conversion of 64.8%. Moreover, Ni-CNFs(1)/MS composite catalyst had higher conversion than that of Ni/MS catalyst.

Considering yields and product selectivities, Ni-CNFs composite catalysts gave higher styrene yield (the main product of phenylacetylene hydrogenation) than that of Ni/MS catalyst. The styrene selectivities of Ni/MS, Ni-CNFs(1)/MS and Ni-CNFs(3)/MS catalysts were 89.6, 91.8 , and 91.6 %, respectively, at same conversion of PA (60 %) (Table 14). It should be noted that the amount of active nickel metal atoms evaluated from CO chemisorption data (stoichiometric value of CO: Ni equals to 2 for CO adsorption analysis) (Table 14) of Ni/MS catalyst was the highest, whereas it became lower with Ni-CNFs(1)/MS and Ni-CNFs(3)/MS catalysts, consecutively. After catalyst modification with CNFs by using CCVD method following the tip-growth mechanism, the amount of active nickel metal atoms was obviously decreased for approximately 1.4 times for Ni-CNFs(1)/MS, and 4.3 times for Ni-CNFs(3)/MS catalysts compared to that of Ni/MS catalyst. This could be attributed to the fact that CNFs formed as the tip-growth mechanism partially covered the active nickel metal atoms. Moreover, this result implied that the longer CCVD period, the greater numbers of fibers of Ni-CNFs catalysts were formed until the CNFs-free active nickel clusters were all transformed into the composite fibers, the amount of active nickel metal atoms was then not changed.

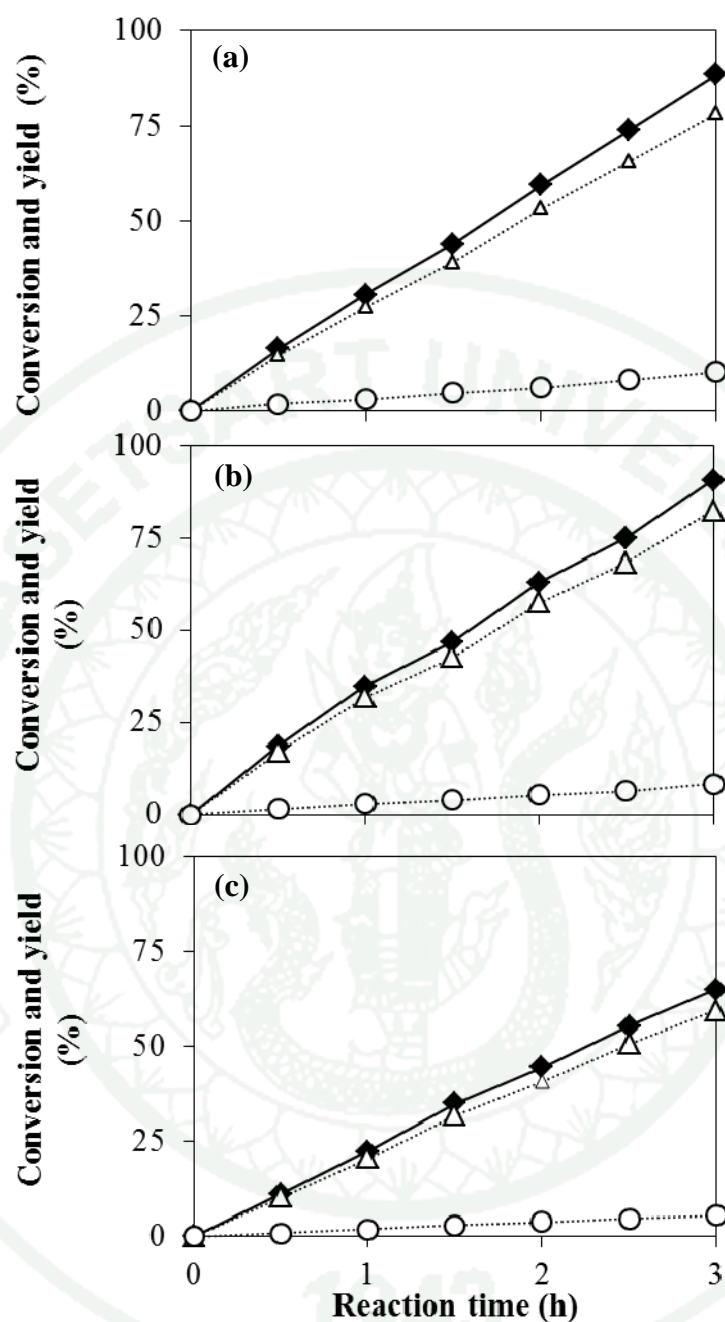


**Figure 46** The reaction-time profiles of phenylacetylene hydrogenation over different catalysts. (a) Ni/MS, (b) Ni-CNFs(1)/MS, and (c) Ni-CNFs(3)/MS

—◆— PA conversion    —△— S yield    —○— EB yield

In order to compare the catalytic activity based on amounts of active nickel metal atoms exposed to reactants, turnover frequencies (TOF) were calculated as shown in Table 14. The TOF value after 3-h time on stream of Ni-CNFs(3)/MS

catalyst was the highest among all catalysts as it was approximately 3.2 and 1.5 times higher than these of Ni/MS and Ni-CNFs(1)/MS catalysts, respectively. This result strongly confirmed that Ni-CNFs composite could enhance the catalytic activity in phenylacetylene hydrogenation due to their better surface hydrophobicity and unique composite structure.

### 3.3 Proposed surface reaction of phenylacetylene hydrogenation over Ni/MS and Ni-CNFs/MS catalysts

The catalytic activity in phenylacetylene hydrogenation could be improved by increasing the surface hydrophobicity of catalysts, leading to better adsorption ability of organic reactants during the reaction, and it therefore simultaneously promoted the catalytic activity in phenylacetylene hydrogenation as the step next to surface adsorption (Singh *et al.*, 2001; Tessonnier *et al.*, 2005). Moreover, since Ni-CNFs composite catalyst was the CNFs containing nickel metal clusters on their individual tips formed over MS support. This structure could therefore potentially overcome the limitation of reactant diffusion to active nickel atoms in order to react and convert to the product in liquid phase reaction.

In order to identify a degree of effect due to structure of Ni-CNFs composite catalyst on the catalytic activity while exclude the effect due to surface hydrophobicity, the TOF value of each catalyst was divided by its hydrophobicity value and compared to that of Ni/MS catalyst. The obtained numbers were 1.4 times for Ni-CNFs(1)/MS and 2.1 times for Ni-CNFs(3)/MS catalysts. This indicated that besides the effect of surface hydrophobicity, the catalyst structure also played significant role in promoting the activity in phenylacetylene hydrogenation. The higher numbers of composite fibers between nickel metal cluster and CNF, the better activity due to the catalyst structure was observed.

Based on the TOF, hydrophobicity, and effect of catalyst structure, the schemes of surface reaction of phenylacetylene hydrogenation over Ni/MS and Ni-CNFs/MS catalysts were proposed (Figure 47). It should be noted that the major

difference in structural characteristics between Ni/MS and Ni-CNFs/MS catalysts was the position of active nickel atoms. With Ni/MS catalyst, nickel metal clusters were mainly dispersed in the inner cavities of MS supports (Figure 47Aa). Consequently, the steric hindrance was potentially found in the case of Ni/MS catalyst due to the limited space over nickel metal clusters inside the catalyst support (Figure 47Bc). On contrary, in the case of Ni-CNFs/MS catalyst, nickel metal clusters were transformed to a bunch of Ni-CNF via CCVD technique and simultaneously lifted up from the MS support. As a result, the unique structure of an individual CNF with nickel metal cluster on its tip, spread away from the support was observed (Figure 47Bb). Therefore, more phenylacetylene molecules could be adsorbed and reacted to styrene product over Ni-CNFs/MS catalyst compared than that of Ni/MS catalyst, based on the same amount of nickel metal clusters (Figure 47Bd).

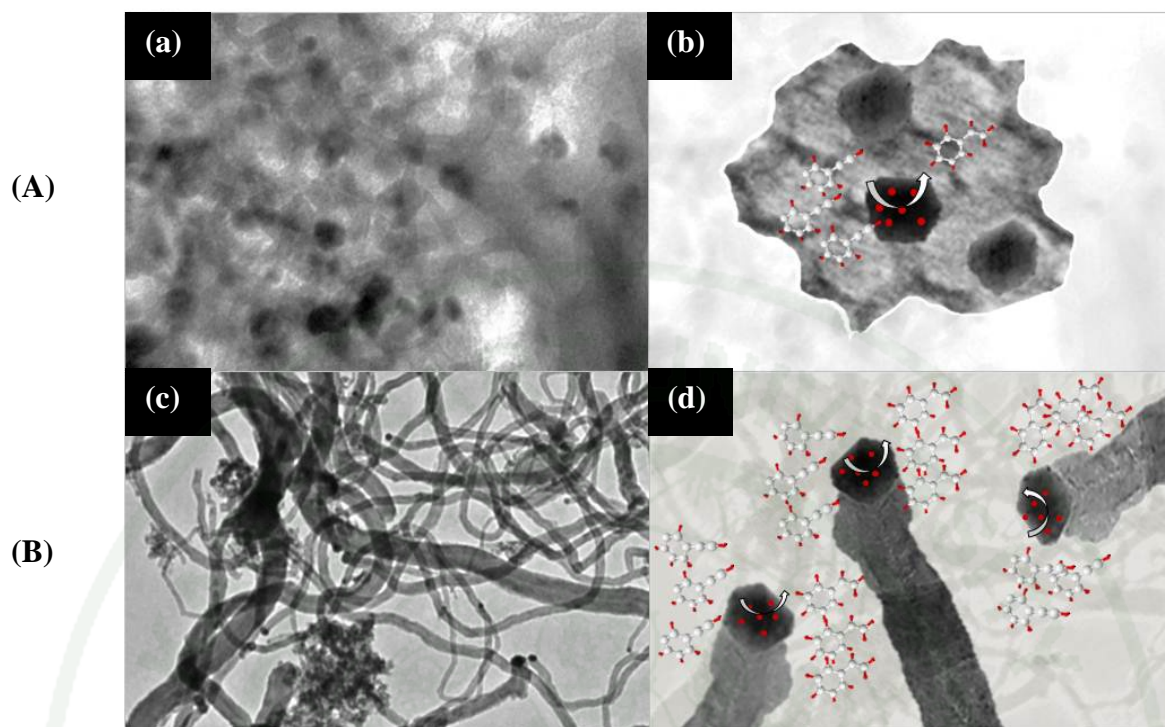


**Figure 47** (A) TEM images (a, b) and (B) proposed schemes of surface reaction of phenylacetylene hydrogenation (c, d) over Ni/MS and Ni-CNFs/MS catalysts.

#### 4. Effect of TiO<sub>2</sub>/carbon photocatalyst on dye degradation.

##### 4.1 Physical and chemical property of TiO<sub>2</sub>-carbon composite catalyst

Textural properties of TiO<sub>2</sub>-carbon composites (including TiO<sub>2</sub>-ZTC, and TiO<sub>2</sub>-AC) and pure TiO<sub>2</sub> powder were examined using nitrogen adsorption technique. BET method was applied to calculate the specific surface area and pore volume as shown the result in Table 15. The specific surface area and pore volume of TiO<sub>2</sub>-ZTC composite were approximately 2.5 times higher than those of TiO<sub>2</sub>-AC prepared by the use of commercialized activated carbon. TiO<sub>2</sub>-ZTC and TiO<sub>2</sub>-AC composite catalysts showed type I isotherm, indicating the existence of microporous structure (Figure 48A(a) and (b)), whereas TiO<sub>2</sub> powder (Figure 48A(c)) exhibited type IV isotherm due to the presence of mesoporous structure. Pore size distribution calculated by using Saito and Foley (SF) method revealed that the TiO<sub>2</sub>-ZTC composite catalyst (Figure 48B(a)) had larger pore size and relatively broader micro-pore size in range of 0.65-1.15 nm compared to the TiO<sub>2</sub>-AC composite catalyst which has a narrow pore size distribution (0.75 nm) (Figure 48B(b)).

Water adsorption measurement was used to evaluate surface hydrophobicity of the composite catalysts at 298 K. The amounts of water adsorbed per unit surface area were determined at the relative pressure ( $P/P_0 = 0.3$ ), as shown in Table 15. The amounts of water adsorbed on TiO<sub>2</sub>-ZTC was 6 times and 43 times lower than that on TiO<sub>2</sub>-AC and pure TiO<sub>2</sub>, showing the highest hydrophobic property as compared to the other composite catalysts.

The significant differences of TiO<sub>2</sub> dispersion over ZTC and AC supports were clearly observed by TEM technique, as shown in Figure. 49. It was found that ZTC support exhibited the relatively high dispersion of segregated TiO<sub>2</sub> nanoparticle clusters (Figure 49a). It should be noted that the unoccupied surface of ZTC was also extensively observed, while AC support led to the formation of aggregate clusters of TiO<sub>2</sub> nanoparticles (Figure 49b).

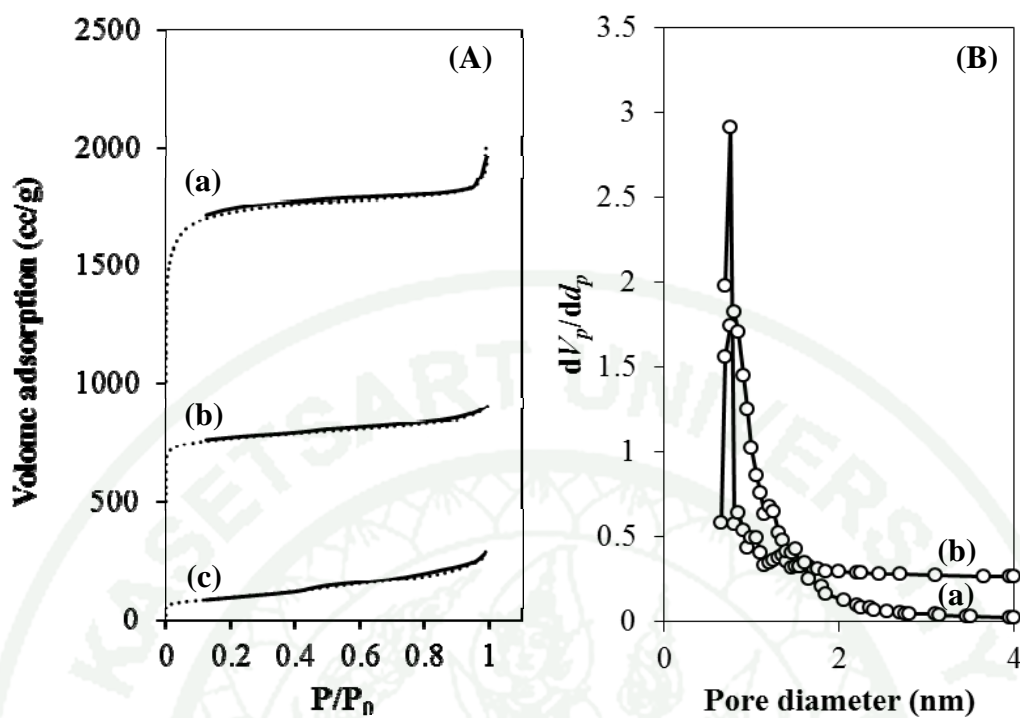


**Figure 48** (A) Nitrogen adsorption-desorption isotherm and (B) pore size distribution of catalysts. (a) TiO<sub>2</sub>-ZTC, (b) TiO<sub>2</sub>-AC, and (c) TiO<sub>2</sub> (AMT-100)

**Table 15** Physical properties of TiO<sub>2</sub> composite catalysts with different carbon supports

Catalysts	BET surface area (m <sup>2</sup> /g)	Pore volume (cm <sup>3</sup> /g)	Adsorption capacity of water <sup>a</sup> (cm <sup>3</sup> /m <sup>2</sup> )
TiO <sub>2</sub>	280	0.45	0.43
TiO <sub>2</sub> -ZTC	2167	1.56	0.01
TiO <sub>2</sub> -AC	846	0.62	0.06

<sup>a</sup> Calculated from water adsorption at P/P<sub>0</sub> of 0.3 and 298 K.

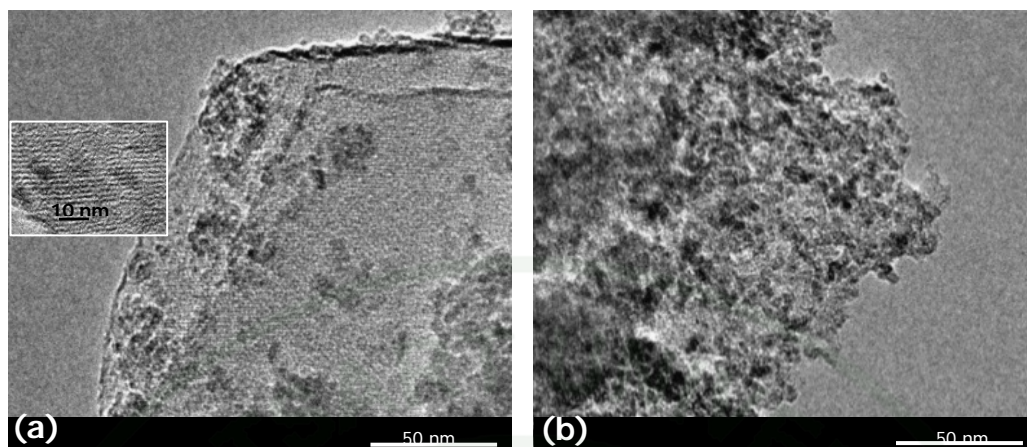


**Figure 49** TEM images of TiO<sub>2</sub> composite catalysts. (a) TiO<sub>2</sub>-ZTC and (b) TiO<sub>2</sub>-AC

The adsorption performance of carbon supports was investigated under dark condition using an aqueous solution of MB as the adsorbate. The differences of adsorption capacity of MB were clearly observed in the color changes of MB solution. As shown in Figure 50, UV-vis absorption spectrum of MB solution (concentration: 0.3 mM) shows intense absorption peak at around 664 nm. The effect of the addition of each sample into this solution was observed in the photographic images (Figure 51). ZTC support could completely adsorb MB, while AC support showed moderate adsorption capacity. However, quite small adsorption of MB was observed in the case of pure TiO<sub>2</sub>. As shown in Figure 50, with increasing the concentration of MB (0.3, 0.5, 0.7 and 1 mM), the adsorption capacity of ZTC support was increased, whereas the adsorption capacities of AC support and pure TiO<sub>2</sub> were not changed and quite constant at 0.16 and 0.018 g<sub>MB</sub>/g<sub>Support</sub>, respectively. From this result, ZTC support exhibited superior adsorption capacity ( $Q_e$ ) of MB in this concentration range due to its excellent physical properties including high specific surface area, large pore volume, and high hydrophobic surface property.

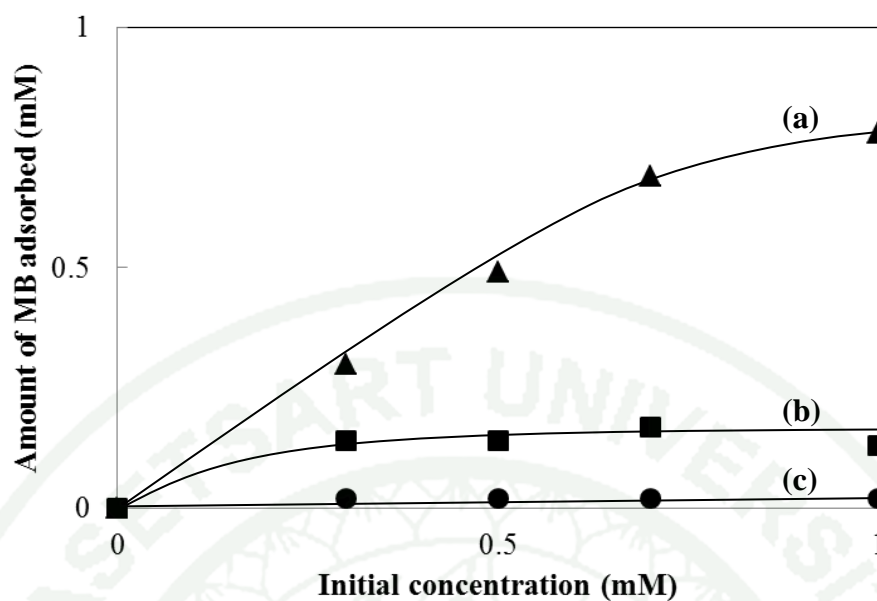


**Figure 50** Adsorption isotherm of MB over different carbon supports after 30 min under dark condition. (a) ZTC, (b) AC and (c) pure TiO<sub>2</sub>.

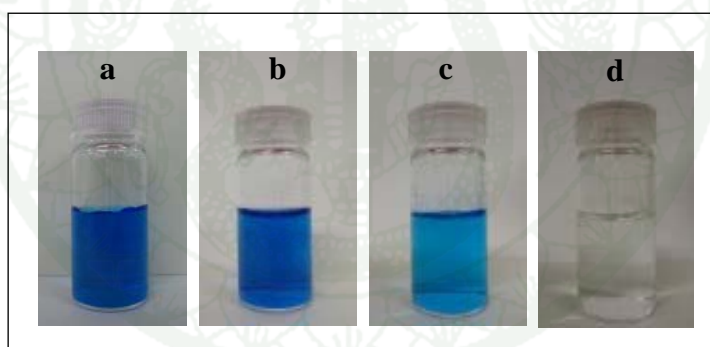


**Figure 51** Photographs of MB adsorption of different carbon supports under dark condition after 30 min; (a) initial concentration of 0.3 mM of MB, (b) pure TiO<sub>2</sub> (AMT-100), (c) AC support, and (d) ZTC support.

## 4.2 Photocatalyst reaction

TiO<sub>2</sub> composites with different carbon supports were tested in methylene blue degradation under UV light irradiation. The catalyst performance was revealed in the term of rate of degradation (Figure 52) calculated by using Equation 28.

$$\ln (C/C_0) = kt \quad (30)$$

where C<sub>0</sub> is initial concentration (mM), C is concentration at a given UV irradiation time (mM), t is time (h), and k is rate of degradation (h<sup>-1</sup>).

In this series of experiment, the TiO<sub>2</sub> slurry that provided the same type of TiO<sub>2</sub> powder used as a reference (pure TiO<sub>2</sub>) was used to load onto the carbon supports throughout this work. The diffraction peaks of TiO<sub>2</sub>, observed at 2θ of 25°, 37°, 47°, 55° and 63°, clearly indicated the existence of anatase phase (Figure 53) (Sivalingam *et al.*, 2003; Caplovicova *et al.*, 2012). It was found that TiO<sub>2</sub>-carbon composites had better potential to decompose MB molecules than that of pure TiO<sub>2</sub>. Among these composites, ZTC composite catalyst exhibited the highest photocatalytic activity as demonstrated in term of the rate of MB degradation. These results indicated that the catalyst performance strongly depended on the type of carbon supports.

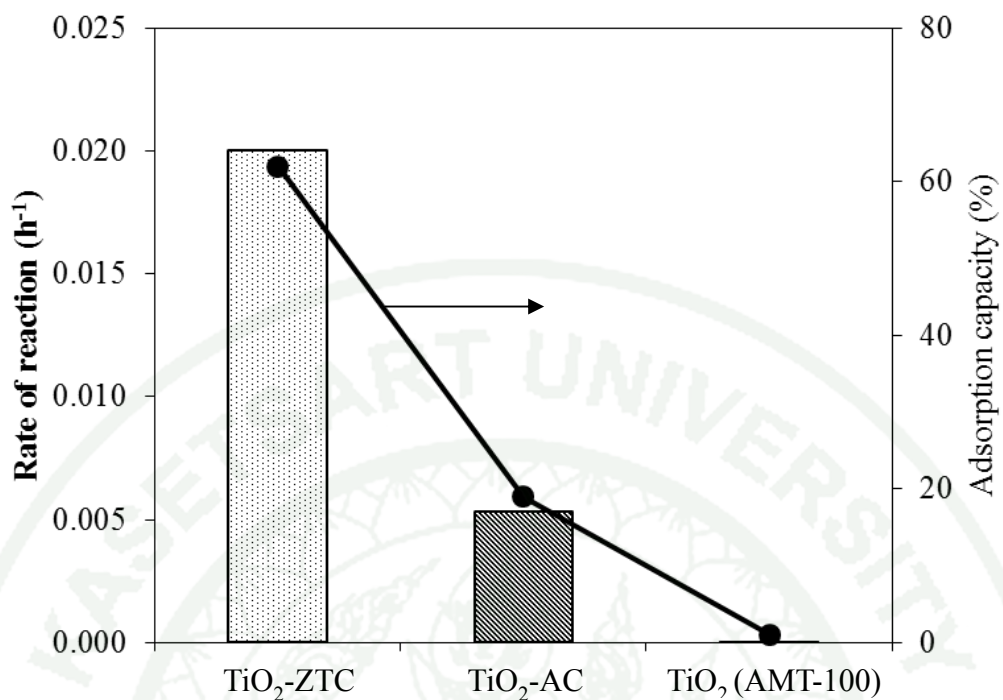


**Figure 52** Photocatalytic activities of TiO<sub>2</sub> composite catalysts with different carbon supports for photodegradation of methylene blue at 24-h reaction time.

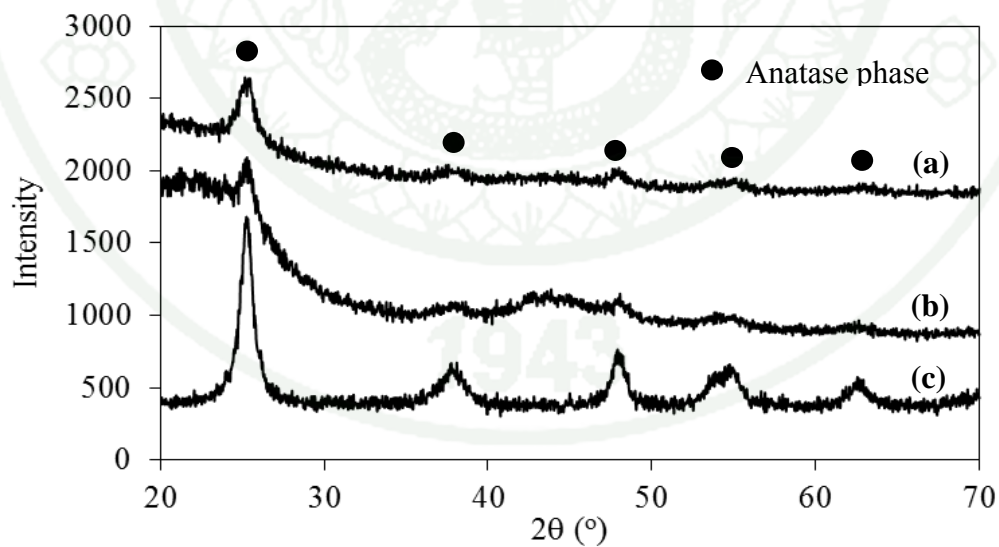


**Figure 53** XRD patterns of catalysts.

(a) TiO<sub>2</sub>-ZTC, (b) TiO<sub>2</sub>-AC, and (c) TiO<sub>2</sub> (AMT-100).

From these results, it can be concluded that TiO<sub>2</sub>-ZTC composite could enhance the performance in photodegradation of methylene blue due to the following reasons: 1) large specific surface area, large pore volume and high hydrophobic surface property strongly increased the adsorption capacity of organic compounds (MB in water), 2) extremely high surface area enabled to promote the dispersion of TiO<sub>2</sub> active sites and 3) ZTC could improve the photocatalytic activity of TiO<sub>2</sub> by reducing the recombination of electron-hole pairs.

Normally, the recombination of electron and hole occurs very fast under UV light irradiation. Nevertheless, utilization of ZTC as the composite support with TiO<sub>2</sub> could resolve this problem by means of the following proposed process: the excited electrons at the conduction band (CB) move to ZTC surface and react with O<sub>2</sub> adsorbed on the ZTC surfaces, and then form superoxide anions ( $\bullet\text{O}_2^-$ ). Simultaneously, the positive holes react with water molecules or hydroxyl groups and generate hydroxyl radicals ( $\bullet\text{OH}$ ). After that, both the superoxide anions and hydroxyl radicals then continuously decompose organic molecules (Yu *et al.*, 2005; Kuo *et al.*, 2009).

## CONCLUSION AND RECOMMENDATIONS

### Conclusion

In this research, the main results were categorized based on types of carbon composite catalysts and their test reactions into four parts including (1) mesocellular silica synthesis, (2) effect of nickel-carbon nanotubes/mesocellular silica composite catalysts on dry reforming reaction, (3) effect of nickel-carbon nanofibers/mesocellular silica composite catalysts on phenylacetylene hydrogenation reaction, and (4) effect of  $\text{TiO}_2$ /carbon photocatalysts on dye degradation reaction. These results can be concluded as follows:

#### 1. Mesocellular silica synthesis

- The amount of TMB and sequences of TMB addition in SBA-15 synthesis have a significant effect on the characteristics of porous structure of mesocellular silica.

- The suitable condition for mesocellular silica synthesis was as follows: Pluronic P123/TMB ratio of 2 and the sequence of TMB addition immediately after HCl addition.

#### 2. Effect of nickel-carbon nanotubes/mesocellular silica composite catalysts on dry reforming reaction

- The composites between nickel and carbon nanotubes over mesocellular silica support (Ni-CNTs/MS) were successfully synthesized through tip-growth mechanism using CCVD technique.

- Based on the same amount of nickel metal on each catalyst, after 24 h of reaction period, the conversions of  $\text{CO}_2$  and  $\text{CH}_4$  were approximately 3 % increased with Ni-CNTs/MS catalysts, while they were 10 % decreased with Ni/MS catalysts.

- The unique characteristics of composite catalysts with nickel on the tips of CNTs could result in selective formation of carbon products as the tube-length extension of CNTs via tip-growth mechanism, and therefore prolonging the stability of catalysts. However, without CNT composites, the random formation of carbon nanofibers could partially block nickel active metals and deactivate the catalysts.

### 3. Effect of nickel-carbon nanofibers-mesocellular silica composite catalyst on phenylacetylene hydrogenation reaction

- The composites of nickel and carbon nanofibers over mesocellular silica support (Ni-CNFs/MS) were successfully synthesized through tip-growth mechanism using CCVD technique.

- With catalyst modification in the form of Ni metal clusters on the tips of CNFs, the higher catalytic performance of Ni-CNFs/MS catalyst was obtained compared to that of the conventional Ni/MS catalyst.

- The higher surface hydrophobicity and unique structure with Ni clusters on tips of Ni-CNFs/MS catalysts were the main effect for improving the performance of Ni-CNFs/MS catalysts in hydrogenation reaction.

### 4. Effect of TiO<sub>2</sub>/carbon photocatalyst on dye degradation

- TiO<sub>2</sub>-ZTC composite catalyst revealed the highest specific surface area, pore volume and hydrophobic surface property compared to that of TiO<sub>2</sub>-AC composite catalyst.

- The excellent adsorption property of organic compounds and the electron transfer property of TiO<sub>2</sub>-ZTC surface could slow down the electron-hole pair recombination and enhance the photocatalytic activity in the degradation of methylene blue.

### **Recommendations**

Even though the results from this research have indicated new findings, the other issues related to this study should be further studied in detail. The recommendations regarding further studies are given as follows:

1. The catalyst stability of Ni-CNTs/MS catalyst reaction was obtained during dry reforming at 650°C for 24 h. However, only CNTs synthesized at 750°C has been applied in this reaction. Other CNTs synthesis temperatures affecting the activity and stability of dry reforming reaction should be further investigated.
2. Due to the unique characteristics of the composite catalysts with metal on the tips of CNTs, other potential applications should be considered and investigated.

## LITERATURE CITED

- Abild-Pedersen, F. and J.K. Norskov. 2006. Mechanisms for catalytic carbon nanofiber growth studied by ab initio density functional theory calculations. **Physical Review B**. 73: 115419 (1-13).
- Aiello, R., J.E. Fiscus, H.C. zur Loye and M.D. Amiridis. 2000. Hydrogen production via the direct cracking of methane over Ni/SiO<sub>2</sub>: catalyst deactivation and regeneration. **Applied Catalysis A: General**. 192: 227–234.
- Amin, A.M., E. Croiset, C. Constantinou and W. Epling. 2012. Methane cracking using Ni supported on porous and non-porous alumina catalysts. **International Journal of Hydrogen Energy**. 37: 9038-9048.
- Bai, J.B., A.L. Hamon, A. Marraud, B. Jouffrey and V. Zyma. 2002. Synthesis of SWNTs and MWNTs by a molten salt (NaCl) method. **Chemical Physics Letters**. 365: 184–188.
- Ballarini, A., F. Basile, P. Benito, I. Bersani, G. Fornasari, S. de Miguel, S.C.P. Maina, J. Vilella, A. Vaccari and O.A. Scelzaa. 2012. Platinum supported on alkaline and alkaline earth metal-doped alumina as catalysts for dry reforming and partial oxidation of methane. **Applied Catalysis A: General**. 433–434: 1–11.
- Barreca, D., W.J. Blau, G.M. Croke, F.A. Deeney, F.C. Dillon, J.D. Holmes, C. Kufazvinei, M.A. Morris, T.R. Spalding and E. Tondello. 2007. Iron oxide nanoparticle impregnated mesoporous silicas as platforms for the growth of carbon nanotubes. **Microporous and Mesoporous Materials**. 103: 142–149.
- Barroso-Quiroga M.M. and A.E. Castro-Luna. 2010. Catalytic activity and effect of modifiers on Ni-based catalysts for the dry reforming of methane. **International Journal of Hydrogen Energy**. 35: 6052-6056.

- Basimova, R.A., M.L. Pavlov, S.I. Myachin, A.V. Prokopenko and A.V. Askarova. 2009. Selective hydrogenation on palladium-containing catalysts of byproduct phenylacetylene present in industrial fractions of styrene. **Petroleum Chemistry**. 49: 360–365.
- Baudouin, D., U. Rodemerck, F. Krumeich, A. de Mallmann, K.C. Szeto, H. Ménard, L. Veyre, J.P. Candy, P.B. Webb, C. Thieuleux and C. Coperet. 2013. Particle size effect in the low temperature reforming of methane by carbon dioxide on silica-supported Ni nanoparticles. **Journal of Catalysis**. 297: 27–34.
- Bautista, F.M., J.M. Campelo, A. Garcia, D. Luna, J.M. Marinas, R.A. Quiros and A.A. Romero, 1998. Influence of surface support properties on the liquid-phase selective hydrogenation of phenylacetylene on supported nickel catalysts. **Catalysis Letters**. 52: 205–213.
- Bhavani, A.G., W.Y. Kim and J.S. Lee. 2013. Barium substituted lanthanum manganite perovskite for CO<sub>2</sub> reforming of methane. **ACS Catalysis**. 3: 1537–1544.
- Bradford, M.C.J. and M.A. Vannice. 1999. CO<sub>2</sub> reforming of CH<sub>4</sub>. **Catalysis Reviews: Science and Engineering**. 41: 1-42.
- Caplovicova, M., P. Billik, L. Caplovic, V. Brezova, T. Turanie, G. Plescha and P. Fejdi. 2012. On the true morphology of highly photoactive anatase TiO<sub>2</sub> nanocrystals. **Applied Catalysis B: Environmental**. 117– 118: 224– 235.
- Castro, A.J.R., J.M. Soares, J.M. Filho, A.C. Oliveira, A. Campos and E.R.C. Milet. 2013. Oxidative dehydrogenation of ethylbenzene with CO<sub>2</sub> for styrene production over porous iron-based catalysts. **Fuel**. 108: 740–748.

- Chen, J., G. Li, Y. Huang, H. Zhang, H. Zhao, T. An. 2012. Optimization synthesis of carbon nanotubes-anatase TiO<sub>2</sub> composite photocatalyst by response surface methodology for photocatalytic degradation of gaseous styrene. **Applied Catalysis B: Environmental** 123–124: 69–77.
- \_\_\_\_\_, R., Q. Wang, Y. Dub, W. Xinga and N. Xu. 2009. Effect of initial solution apparent pH on nano-sized nickel catalysts in p-nitrophenol hydrogenation. **Chemical Engineering Journal**. 145: 371–376.
- \_\_\_\_\_, S., Chen, Z. Qin, G. Wang, M. Dong and J. Wang. 2013. Promoting effect of carbon dioxide on the dehydrogenation of ethylbenzene over silica-supported vanadium catalysts. **Fuel** 109: 43–48.
- Chiou, C.H., C.Y. Wu and R.S. Juang. 2008. Influence of operating parameters on photocatalytic degradation of phenol in UV/TiO<sub>2</sub> process. **Chemical Engineering Journal**. 139: 322–329.
- Choudhary, V.R., K.C. Mondal and T.V. Choudhary. 2006. CO<sub>2</sub> reforming of methane to syngas over coo<sub>x</sub>/mgo supported on low surface area macroporous catalyst carrier: influence of co loading and process conditions. **Industrial & Engineering Chemistry Research**. 45: 4597-4602.
- Cui, Y., H. Zhang, H. Xu and W. Li. 2007. Kinetic study of the catalytic reforming of CH<sub>4</sub> with CO<sub>2</sub> to syngas over Ni/ $\alpha$ -Al<sub>2</sub>O<sub>3</sub> catalyst: The effect of temperature on the reforming mechanism. **Applied Catalysis A: General**. 318: 79–88.
- Dominguez-Dominguez, S., A. Berenguer-Murcia, B.K. Pradhan, A. Linares-Solano and D. Cazorla-Amoros. 2008. Semihydrogenation of phenylacetylene catalyzed by palladium nanoparticles supported on carbon materials. **The Journal of Physical Chemistry C**. 112: 3827-3834.

- Dominguez-Dominguez, S., D. Cazorla-Amoros and A. Linares-Solano. 2006. Semihydrogenation of phenylacetylene catalyzed by metallic nanoparticles containing noble metals. **Journal of Catalysis**. 243: 74–81.
- Duraczynska, D., E.M. Serwicka, A. Drelinkiewicz and Z. Olejniczak. 2009. Ruthenium (II) phosphine/mesoporous silica catalysts: the impact of active phase loading and active site density on catalytic activity in hydrogenation of phenylacetylene. **Applied Catalysis A: General**. 371: 166–172.
- Dussault, L., J.C. Dupin, C. Guimon, M. Monthieux, N. Latorre, T. Ubieta, E. Romeo, C. Royo and A. Monzon. 2007. Development of Ni–Cu–Mg–Al catalysts for the synthesis of carbon nanofibers by catalytic decomposition of methane. **Journal of Catalysis**. 251: 223–232.
- Edwards, J.H. and A.M. Maitra. 1995. The chemistry of methane reforming with carbon dioxide and its current and potential applications. **Fuel Processing Technology**. 42: 269-289.
- Fan, M.S. A.Z. Abdullah and S. Bhatia. 2009. Catalytic technology for carbon dioxide reforming of methane to synthesis gas. **ChemCatChem**. 1: 192 – 208.
- Ferreira-Aparicio, P., M. Fernandez-Garcia, A. Guerrero-Ruiz and I. Rodriguez-Ramo. 2000. Evaluation of the role of the metal–support interfacial centers in the dry reforming of methane on alumina-supported rhodium catalysts. **Journal of Catalysis**. 190: 296–308.
- Fidalgo, B. and J.A. Menendez. 2011. Carbon materials as catalysts for decomposition and CO<sub>2</sub> reforming of methane: a review. **Chinese Journal of Catalysis**. 32: 207–216.
- Fujishima, A., T.N. Rao, D.A. Tryk. 2000. Titanium dioxide photocatalysis. **Journal of Photochemistry and Photobiology C: Photochemistry Reviews**. 1: 1–21.

- Gallego, G.S., J.G. Marin, C. Batiot-Dupeyrat, J. Barrault and F. Mondragon. 2009. Influence of Pr and Ce in dry methane reforming catalysts produced from  $\text{La}_{1-x}\text{A}_x\text{NiO}_{3-\delta}$  perovskites. **Applied Catalysis A: General**. 369: 97–103.
- Ghosh, P., T. Soga, K. Ghosh, T. Jimbo, R. Katoh, K. Sumiyama and Y. Ando. 2008. Effect of sulfur concentration on the morphology of carbon nanofibers produced from a botanical hydrocarbon. **Nanoscale Res Lett**. 3:242–248.
- Guo, J., H. Lou and X. Zheng. 2007. The deposition of coke from methane on a Ni/MgAl<sub>2</sub>O<sub>4</sub> catalyst, **Carbon**. 45: 1314–1321.
- \_\_\_\_\_, X., Y. Sun, Y. Yu, X. Zhu and C.J. Liu. 2012. Carbon formation and steam reforming of methane on silica supported nickel catalysts. **Catalysis Communications**. 19: 61–65.
- Harris, P.J.F.. 2009. **Carbon nanotube science synthesis, properties and applications**. Cambridge University Press. New York.
- He, S., J. Wei, H. Wang, D. Sun, Z. Yao, C. Fu, R. Xu, Y. Jia, H. Zhu, K. Wang and D. Wu. 2013. Stable superhydrophobic surface of hierarchical carbon nanotubes on Si micropillar arrays. **Nanoscale Research Letters**. 8:412-417.
- Hernadi, K., A. Fonseca, J.B. Nagya, A. Siska and I. Kiricsi. 2000. Production of nanotubes by the catalytic decomposition of different carbon-containing compounds. **Applied Catalysis A: General** 199: 245–255.
- Hong, K.B., A.A.B Ismail, M.E.B.M. Mahayuddin, A.R. Mohamed and S.H.S. Zeiri. 2006. Production of high purity multi-walled carbon nanotubes from catalytic decomposition of methane. **Journal of Natural Gas Chemistry**. 15: 266-270.

- Houas, A., H. Lachheb, M. Ksibi, E. Elaloui, C. Guillard and J.M. Herrmann. 2001. Photocatalytic degradation pathway of methylene blue in water. **Applied Catalysis B: Environmental**. 31: 145–157.
- Iler, R.K. 1979. **The chemistry of silica**. Willy. New York.
- Ishida, T., T. Yanagihara, X. Liu, H. Ohashi, A. Hamasaki, T. Honma, H. Oji, T. Yokoyama and M. Tokunaga. 2013. Synthesis of higher alcohols by Fischer–Tropsch synthesis over alkali metal-modified cobalt catalysts. **Applied Catalysis A: General**. 458: 145– 154.
- Jahjah, M., Y. Kihn, E. Teuma and M. Gomeza. 2010. Ruthenium nanoparticles supported on multi-walled carbon nanotubes: highly effective catalytic system for hydrogenation processes. **Journal of Molecular Catalysis A: Chemical**. 332: 106–112.
- Ji, J., X. Duan, G. Qian, X. Zhou, D. Chen and W. Yuan. 2013. In situ production of Ni catalysts at the tips of carbon nanofibers and application in catalytic ammonia decomposition. **Industrial & Engineering Chemistry Research**. 52: 1854–1858.
- Jong, K.P.D. and J.W. Geus. 2000. Carbon nanofibers: catalytic synthesis and applications. **Catalysis Reviews: Science and Engineering**. 42: 481-510.
- Jung, J.S., W.S. Chae, R.A. McIntyre, C.T. Seip, J.B. Wiley and C.J. O'Connor. 1999. Preparation and characterization of Ni nanoparticles in an MCM mesoporous material. **Materials Research Bulletin**. 34: 1353–1360.
- Kamat, P.V. 1993. Photochemistry on nonreactive and reactive (semiconductor) surfaces. **Chemical Reviews**. 93: 267-300.

- Kambolis, A., H. Matralis, A. Trovarelli and C. Papadopoulou. 2010. Ni/CeO<sub>2</sub>-ZrO<sub>2</sub> catalysts for the dry reforming of methane. **Applied Catalysis A: General** 377: 16–26.
- Kamegawa, T., D. Yamahana and H. Yamashita. 2010. Graphene coating of tio<sub>2</sub> nanoparticles loaded on mesoporous silica for enhancement of photocatalytic activity. **The Journal of Physical Chemistry C**. 114: 15049–15053.
- Kim, Y.I., D. Soundararajan, C.W. Park, S.H. Kim, J.H. Park and J.M. Ko. 2009. Electrocatalytic properties of carbon nanofiber web–supported nanocrystalline pt catalyst as applied to direct methanol fuel cell. **International Journal of Electrochemical Science**., 4: 1548 – 1559.
- Kumar, M. and Y. Ando. 2010. Chemical vapor deposition of carbon nanotubes: a review on growth mechanism and mass production. **Journal of Nanoscience and Nanotechnology**. 10: 3739–3758.
- \_\_\_\_\_, S., T. Rath, R.N. Mahaling, C.S. Reddy, C.K. Das, K.N. Pandey, R.B. Srivastava and S.B. Yadaw. 2007. Study on mechanical, morphological and electrical properties of carbon nanofiber/polyetherimide composites. **Materials Science and Engineering B**. 141: 61–70.
- Kuo, C.Y. 2009. Prevenient dye-degradation mechanisms using UV/TiO<sub>2</sub>/carbon nanotubes process. **Journal of Hazardous Materials**. 163: 239–244.
- Lee, S.A., S.H. Hong, D.O. Kim, T.H. Han, S.I. and J.D. Nam, 2008, A mesoporous composite template composed of self-assembled silica nanotube and multi-walled carbon nanotube, **Microporous and Mesoporous Materials** 111; 292–299

- Lee, T.Y., J.H. Hana, S.H. Choia, J.B. Yooa, C.Y. Parka, T. Jungb, S. Yub, J. Leeb, W. Yib and J.M. Kimb. 2003. Comparison of source gases and catalyst metals for growth of carbon nanotube. **Surface and Coatings Technology** 169 –170: 348–352.
- Lettow, J.S., Y.J. Han, P. Schmidt-Winkel, P. Yang, D. Zhao, G.D. Stucky and J.Y. Ying. 2000. Hexagonal to mesocellular foam phase transition in polymer-templated mesoporous silicas. **Langmuir**.16: 8291-8295.
- Li, C., Z. Shao, M. Pang, C.T. Williams and C. Liang. 2012. Carbon nanotubes supported Pt catalysts for phenylacetylene hydrogenation: effects of oxygen containing surface groups on Pt dispersion and catalytic performance. **Catalysis Today** 186: 69–75.
- \_\_\_\_\_. 2012. Carbon nanotubes supported Pt catalysts for phenylacetylene hydrogenation: effects of oxygen containing surface groups on Pt dispersion and catalytic performance. **Catalysis Today**. 186: 69– 75.
- \_\_\_\_\_, and X. Zhang. 2012. Carbon nanotubes supported mono- and bimetallic pt and ru catalysts for selective hydrogenation of phenylacetylene. **Industrial & Engineering Chemistry Research**. 51: 4934–4941.
- Li, N., X. Wang, S. Derrouiche, G.L. Haller and L.D. Pfefferle. 2010. Role of Surface Cobalt Silicate in Single-Walled Carbon Nanotube Synthesis from Silica-Supported Cobalt Catalysts. **ACS NANO**. 4: 1759-1767.
- \_\_\_\_\_, Y., B. Xu, Y. Fan, N. Feng, A. Qiu, J.M.J. He, H Yang and Y. Chen. 2004. The effect of titania polymorph on the strong metal-support interaction of Pd/TiO<sub>2</sub> catalysts and their application in the liquid phase selective hydrogenation of long chain alkadienes. **Journal of Molecular Catalysis A: Chemical**. 216: 107–114.

- Lima, S.M., J.M. Assaf, M.A. Pena and J.L.G. Fierro. 2006. Structural features of  $\text{La}_{1-x}\text{Ce}_x\text{NiO}_3$  mixed oxides and performance for the dry reforming of methane. **Applied Catalysis A: General**. 311: 94–104.
- Linssen, T., K. Cassiers, P. Cool and E.F. Vansant. 2003. Mesoporous templated silicates: an overview of their synthesis, catalytic activation and evaluation of the stability. **Advances in Colloid and Interface Science**. 103: 121–147
- Liu, J, L. Zhang, Q. Yang and C. Li. 2008. Structural control of mesoporous silicas with large nanopores in a mild buffer solution. **Microporous and Mesoporous Materials** 116: 330–338.
- Lu, G.Q. and S. Wang. 1999. Ni-based catalysts for carbon dioxide reforming of methane. **Chemtech**. 29: 37-43.
- Luechinger, M., G. D. Pirngruber, B. Lindlar, P. Laggner and R. Prins. 2005. The effect of the hydrophobicity of aromatic swelling agents on pore size and shape of mesoporous silicas. **Microporous and Mesoporous Materials** 79: 41–52.
- Ma Q., D. Wang, M. Wu, T. Zhao, Y. Yoneyama and N. Tsubak. 2013. Effect of catalytic site position: Nickel nanocatalyst selectively loaded inside or outside carbon nanotubes for methane dry reforming. **Fuel**. 108: 430–438.
- \_\_\_\_\_, Z., T. Kyotani and A. Tomita. 2000. Preparation of a high surface area microporous carbon having the structural regularity of Y zeolite. **Chemical Communications**. 2365–2366.
- Mathur, R.B., S. Chatterjee and B.P. Singh. 2008. Growth of carbon nanotubes on carbon fibre substrates to produce hybrid/phenolic composites with improved mechanical properties. **Composites Science and Technology**. 68: 1608–1615.

- Na-Chiangmai, C., N. Tiengchad, P. Kittisakmontree, O. Mekasuwandumrong, J. Powell and J. Panpranot. 2011. Characteristics and catalytic properties of mesocellular foam silica supported Pd nanoparticles in the liquid-phase selective hydrogenation of phenylacetylene. **Catalysis Letters**. 141: 1149–1155.
- Nagaraja, B.M., D.A. Bulushev, S. Beloshapkin and J.R.H. Ross. 2011. The effect of potassium on the activity and stability of Ni–MgO–ZrO<sub>2</sub> catalysts for the dry reforming of methane to give synthesis gas. **Catalysis Today**. 178: 132–136.
- Nakata, K., A. Fujishima. 2012. TiO<sub>2</sub> photocatalysis: design and applications. **Journal of Photochemistry and Photobiology C: Photochemistry Reviews**. 13: 169–189.
- Navalikhina, M.D., N.E. Kavalerskaya, E.S. Lokteva, A.A. Peristy, E.V. Golubina, and V.V. Lunin. 2012. Selective hydrogenation of phenylacetylene on ni and ni–pd catalysts modified with heteropoly compounds of the keggin type. **Russian Journal of Physical Chemistry A**. 86: 1800–1807.
- Nhut, J.M., L. Pesant, J.P. Tessonnier, G. Wine, J. Guille, C. Pham-Huu and M.J. Ledoux. 2003. Mesoporous carbon nanotubes for use as support in catalysis and as nanosized reactors for one-dimensional inorganic material synthesis. **Applied Catalysis A: General**. 254: 345–363.
- Nishihara H., Q.H. Yang, P.X. Hou, M. Unno, S. Yamauchi, R. Saito, J.I. Paredes, A. Martinez-Alonso, J.M.D. Tascond, Y. Sato, M. Terauchia and T. Kyotani. 2009. A possible buckybowll-like structure of zeolite templated carbon. **Carbon**. 47: 1220-1230.

- Perez-Cabero, M., I. Rodriguez-Ramos and A. Guerrero-Ruiz. 2003. Characterization of carbon nanotubes and carbon nanofibers prepared by catalytic decomposition of acetylene in a fluidized bed reactor. **Journal of Catalysis**. 215: 305–316.
- Prasad, H., D., S.Y. Park, H. Ji, H.R. Kim, J.W. Son, B.-K. Kim, H.W. Lee, J.H. Lee. 2012. Effect of steam content on nickel nano-particle sintering and methane reforming activity of Ni–CZO anode cermets for internal reforming SOFCs. **Applied Catalysis A: General**. 411– 412: 160– 169.
- Ramesh, P., T. Okazaki, R. Taniguchi, J. Kimura, T. Sugai, K. Sato, Y. Ozeki and H. Shinohara. 2005. Selective Chemical Vapor Deposition Synthesis of Double-Wall Carbon Nanotubes on Mesoporous Silica. **Journal of Physical Chemistry B** 109: 1141-1147.
- Relvas, J., R. Andrade, F.G. Freire, F. Lemos, P. Araujo, M.J. Pinho, C.P. Nunes and F.R. Ribeiro. 2008. Liquid Phase hydrogenation of nitrobenzene over an industrial Ni/SiO<sub>2</sub> supported catalyst. **Catalysis Today**. 133–135: 828–835.
- Richardson, J.T., R. Scates and M.V. Twigg. 2003. X-ray diffraction study of nickel oxide reduction by hydrogen. **Applied Catalysis A: General**. 246: 137–150.
- Rodriguez, N.M., A. Chambers and R.T.K. Baker. 1995. Catalytic Engineering of Carbon Nanostructures. **Langmuir**. 11: 3862-3866.
- Romero, A., A. Garrido, A. Nieto-Marquez, A.R. de la Osa, A. de Lucas and J.L. Valverde. 2007. The influence of operating conditions on the growth of carbon nanofibers on carbon nanofiber-supported nickel catalysts. **Applied Catalysis A: General** 319: 246–258.

- Royal society of chemistry, 2003. Surfactants: the ubiquitous amphiphiles,  
Source: <http://www.rsc.org/chemistryworld/issues/2003/july/amphiphiles.asp>.
- San-Jose-Alonso, D., J. Juan-Juan, M.J. Illan-Gomez and M.C. Roman-Martinez.  
2009. Ni, Co and bimetallic Ni–Co catalysts for the dry reforming of methane.  
**Applied Catalysis A: General**. 371: 54–59.
- Sano, N., S. Yamamoto and H. Tamon. 2014. Cr as a key factor for direct synthesis of  
multi-walled carbon nanotubes on industrial alloys. **Chemical Engineering  
Journal**. 242: 278–284.
- Scheibe, B., E. Borowiak-Palen and R.J. Kalenczuk. 2010. Oxidation and reduction of  
multiwalled carbon nanotubes — preparation and characterization. **Materials  
Characterization**. 61: 185-191.
- Schmidt-Winkel, P., W.W. Lukens, D. Zhao, P. Yang, B.F. Chmelka and G.D.  
Stucky. 1999. Mesocellular Siliceous Foams with Uniformly Sized Cells and  
Windows. **Journal of the American Chemical Society**. 121: 254-255.
- Selvam, P., S.K. Bhatia and C.G. Sonwane. 2001. Recent advances in processing and  
characterization of periodic mesoporous MCM-41 silicate molecular sieves.  
**Industrial Engineering Chemistry Research**. 40: 3237-3261.
- Singh, U.K. and M.A. Vannice. 2001. Kinetics of liquid-phase hydrogenation  
reactions over supported metal catalysts — a review. **Applied Catalysis A:  
General**. 213: 1–24.
- Sivalingam, G., K. Nagaveni, M.S. Hegde and G. Madras. 2003. Photocatalytic  
degradation of various dyes by combustion synthesized nano anatase TiO<sub>2</sub>.  
**Applied Catalysis B: Environmental**. 45: 23–38.

- Sousa, H.S.A., A.N. da Silva, A.J.R. Castro, A. Campos, J.M. Filho and A.C. Oliveir. 2012. Mesoporous catalysts for dry reforming of methane: Correlation between structure and deactivation behavior of Ni-containing catalysts. **International Journal of Hydrogen Energy**. 37: 12281-12291.
- Takeguchi, T., S.N. Furukawa, M. Inoue and K. Eguchi. 2003. Autothermal reforming of methane over Ni catalysts supported over CaO–CeO<sub>2</sub>–ZrO<sub>2</sub> solid solution. **Applied Catalysis A: General**. 240: 223–233.
- Tavasoli, A., M. Trépanier, R. M. M. Abbaslou, A. K. Dalai, N. Abatzoglou. 2009. Fischer–Tropsch synthesis on mono- and bimetallic Co and Fe catalysts supported on carbon nanotubes. **Fuel Processing Technology**. 90: 1486–1494.
- Teo, K.B.K., C. Singh, M. Chhowalla and W.I. Milne. 2003. Catalytic synthesis of carbon nanotubes and nanofibers. **Encyclopedia of Nanoscience and Nanotechnology**. X: 1-22.
- Tessonnier, J.P., L. Pesant, G. Ehret, M.J. Ledoux and C. Pham-Huu. 2005. Pd nanoparticles introduced inside multi-walled carbon nanotubes for selective hydrogenation of cinnamaldehyde into hydrocinnamaldehyde. **Applied Catalysis A: General**. 288: 203–210.
- Thiruvengkatahari, R., S. Vigneswaran and I.S. Moon. 2008. A review on UV/TiO<sub>2</sub> photocatalytic oxidation process. **Korean Journal of Chemical Engineering**. 25: 64-72.
- Umoren S. A., U. J. Etim and A. U. Israel. 2013. Adsorption of methylene blue from industrial effluent using poly (vinyl alcohol). **Journal of Materials and Environmental Science**. 4: 75-86.

Vila, M., J. L. Hueso, M. Manzano, I. Izquierdo-Barba, A. de Andes, J. Sanchez-Marcos, C. Prietoc and M. Vallet-Regi. 2009. Carbon nanotubes—mesoporous silica composites as controllable biomaterials. **Journal of Materials Chemistry** 19: 7745–7752.

Wan, Y. and D. Zhao. 2007. On the controllable soft-templating approach to mesoporous silicates. **Chemical review**. 107: 2821- 2860

Wang, J., Z. You, Q. Zhang, W. Deng and Y. Wang. 2013. Synthesis of lower olefins by hydrogenation of carbon dioxide over supported iron catalysts. **Catalysis Today** 215: 186– 193.

\_\_\_\_\_, N., W. Chu, T. Zhang and X.S. Zhao. 2012. Synthesis, characterization and catalytic performances of Ce-SBA-15 supported nickel catalysts for methane dry reforming to hydrogen and syngas. **International Journal of Hydrogen Energy**. 37: 19-30.

\_\_\_\_\_, S., G.Q. M. Lu, and G.J. Millar. 1996. Carbon dioxide reforming of methane to produce synthesis gas over metal-supported catalysts : state of the art. **Energy & Fuels**. 10: 896–904.

Weerachawanasak, P., P. Prasertdam, M. Arai, J. Panpranot. 2008. A comparative study of strong metal–support interaction and catalytic behavior of Pd catalysts supported on micron- and nano-sized TiO<sub>2</sub> in liquid-phase selective hydrogenation of phenylacetylene. **Journal of Molecular Catalysis A: Chemical** 279: 133–139.

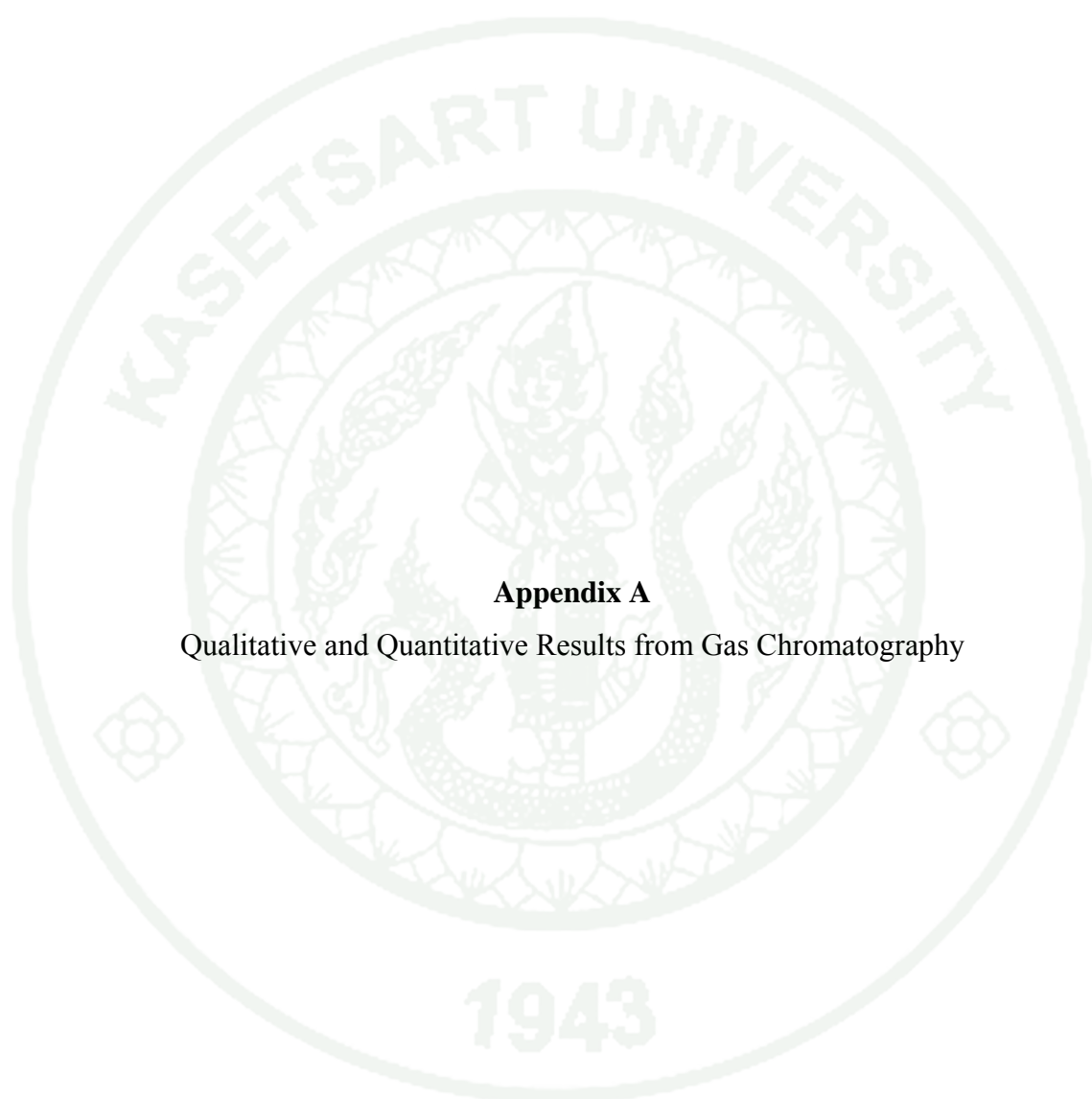
Wikipedia, the free encyclopedia. 2007. Micelle. source:  
[http://en.wikipedia.org/wiki/File:Micelle\\_scheme-en.svg](http://en.wikipedia.org/wiki/File:Micelle_scheme-en.svg),

- Wilhite, B.A., M.J. McCready and A. Varma. 2002. kinetics of phenylacetylene hydrogenation over Pt/ $\gamma$ -Al<sub>2</sub>O<sub>3</sub> catalyst. **Industrial & Engineering Chemistry Research**. 41: 3345-3350.
- Wu, C.H. and J.M. Chern. 2006. Kinetics of photocatalytic decomposition of methylene blue. **Industrial & Engineering Chemistry Research**. 45: 6450-6457.
- Xu, Y.J., Y. Zhuang and X. Fu. 2010. New insight for enhanced photocatalytic activity of tio<sub>2</sub> by doping carbon nanotubes: a case study on degradation of benzene and methyl orange. **The Journal of Physical Chemistry C**. 114: 2669–2676.
- Yao, J. and C. Wang. 2010. Decolorization of methylene blue with TiO<sub>2</sub> sol via UV irradiation photocatalytic degradation. **International Journal of Photoenerg.** 1-6.
- Yu, Y., J.C. Yu, C.Y. Chan, Y.K. Che, J.C. Zhao, L. Ding, W.K. Ge and P.K. Wong. 2005. Enhancement of adsorption and photocatalytic activity of TiO<sub>2</sub> by using carbon nanotubes for the treatment of azo dye, **Applied Catalysis B: Environmental**. 61: 1–11.
- Zeng, C., C. Wang , F. Wang, Y. Zhang and L. Zhang. 2012. A novel vapor–liquid segmented flow based on solvent partial vaporization in microstructured reactor for continuous synthesis of nickel nanoparticles. **Chemical Engineering Journal** 204–206 : 48–53.
- Zhang, M., Y. Wu, X. Feng, X. He, L. Chen and Y. Zhang, 2010, Fabrication of mesoporous silica-coated CNTs and application in size-selective protein separation, **Journal of Materials Chemistry**: 20, 5835–5842.

- Zhang, Y., L. Zhao, J. Li, H. Zhang, L. Zheng, S. Cao and C. Li. 2008. Template enhanced activity of lipase accommodated in siliceous mesocellular foams. **Biochemical and Biophysical Research Communications**. 372: 650–655.
- \_\_\_\_\_, Y., Z.R. Tang, X. Fu and Y.J. Xu. 2010. TiO<sub>2</sub> graphene nanocomposites for gas-phase photocatalytic degradation of volatile aromatic pollutant: is tio<sub>2</sub> graphene truly different from other TiO<sub>2</sub> carbon composite materials. **ACS NANO**. 4: 7303-7314.
- Zhao, D., G. Sheng, C. Chen and X. Wang. 2012. Enhanced photocatalytic degradation of methylene blue under visible irradiation on graphene@TiO<sub>2</sub> dyade structure. **Applied Catalysis B: Environmental** 111– 112: 303– 308.
- \_\_\_\_\_, J. Sun, Q. Li and G.D. Stucky. 2000. Morphological control of highly ordered mesoporous silica SBA-15. **Chemistry of Material**. 12: 275-279.
- \_\_\_\_\_, H., Q. Zhu, Y. Gao, P. Zhai, D. Ma. 2013. Iron oxide nanoparticles supported on pyrolytic graphene oxide as model catalysts for Fischer Tropsch synthesis. **Applied Catalysis A: General**. 456: 233– 239.
- Zholobenko, V.L., A.Y. Khodakov, M.I. Clerc , D. Durand and I. Grillo. 2008. Initial stages of SBA-15 synthesis: An overview. **Advances in Colloid and Interface Science** 142: 67–74.
- Zhu, X., P. Huo, Y.P. Zhang, D.G. Cheng and C.J. Liu. 2008. Structure and reactivity of plasma treated Ni/Al<sub>2</sub>O<sub>3</sub> catalyst for CO<sub>2</sub> reforming of methane. **Applied Catalysis B: Environmental**. 81: 132–140.



**APPENDICES**

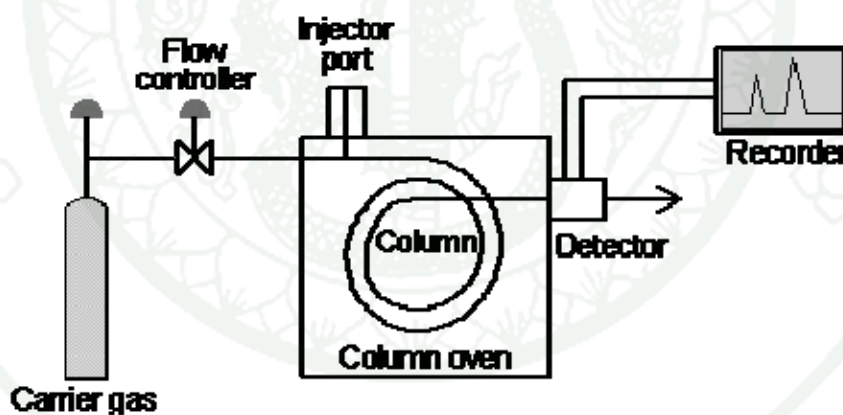


**Appendix A**

Qualitative and Quantitative Results from Gas Chromatography

### Quantitative and Qualitative Results from Gas Chromatography

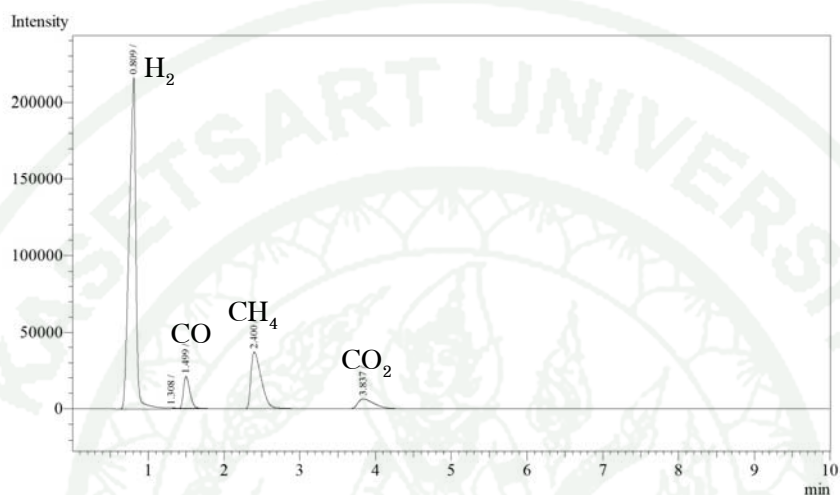
Gas chromatography was performed in a specially designed instrument. The major instrumental components consisted of a flowing mobile phase, an injector port, a separation column containing the stationary phase, a detector, and a data recording system as shown in Appendix Figure A1. Certain amount of gaseous mixture, 0.5 mL in this research, was injected into gas chromatograph at the injector port and was volatilized in a hot injection chamber before it was transported to the head of the chromatographic column. Then, a flow of inert carrier gas (as a mobile phase) swept the injected mixture through a heated column which contained the stationary phase. The gaseous sample moved along the packing column whereas its component gas moved with different flow rates and thus separated into pure component. Before each component exited the instrument, it passed through a detector. The detector sent an electronic signal to the recorder and the analyzed results were printed out.



**Appendix Figure A1** Schematic diagram of gas chromatograph.

In this work, the quantitative and qualitative data of product composition was obtained from 2 types of gas chromatography including TCD-GC as mention in the experimental chapter. Before analysis, the condition of operation was set and kept on running for about an hour to stabilize the based line. Certain volume of sample mixture (0.5 mL in this case) was injected into the injection port by gas syringe. After the mixture of sample gas was analyzed, the qualitative and quantitative data were

interpreted from the peak area obtained from the recorder. The component of injected gas mixture can be identified by using the value of retention time data compared with the retention time received from injected standard gas. The chromatogram of standard gases used in this research was shown as following figures:



**Appendix Figure A2** Chromatogram of standard gases for H<sub>2</sub>, CO, CH<sub>4</sub> and CO<sub>2</sub>.

The quantitative analysis of gas samples were obtained from the calibration curves where the correlation between the amount of injected gas sample (mole) and the peak area of gas chromatograms were proposed. The correlation between these parameters (mole and area) was analyzed by a linear regression equation. All the calibration curves for each single standard gas and liquid used in this research were shown in Appendix Table A1.

**Appendix Table A1** Equation of calibration curves for standard gas

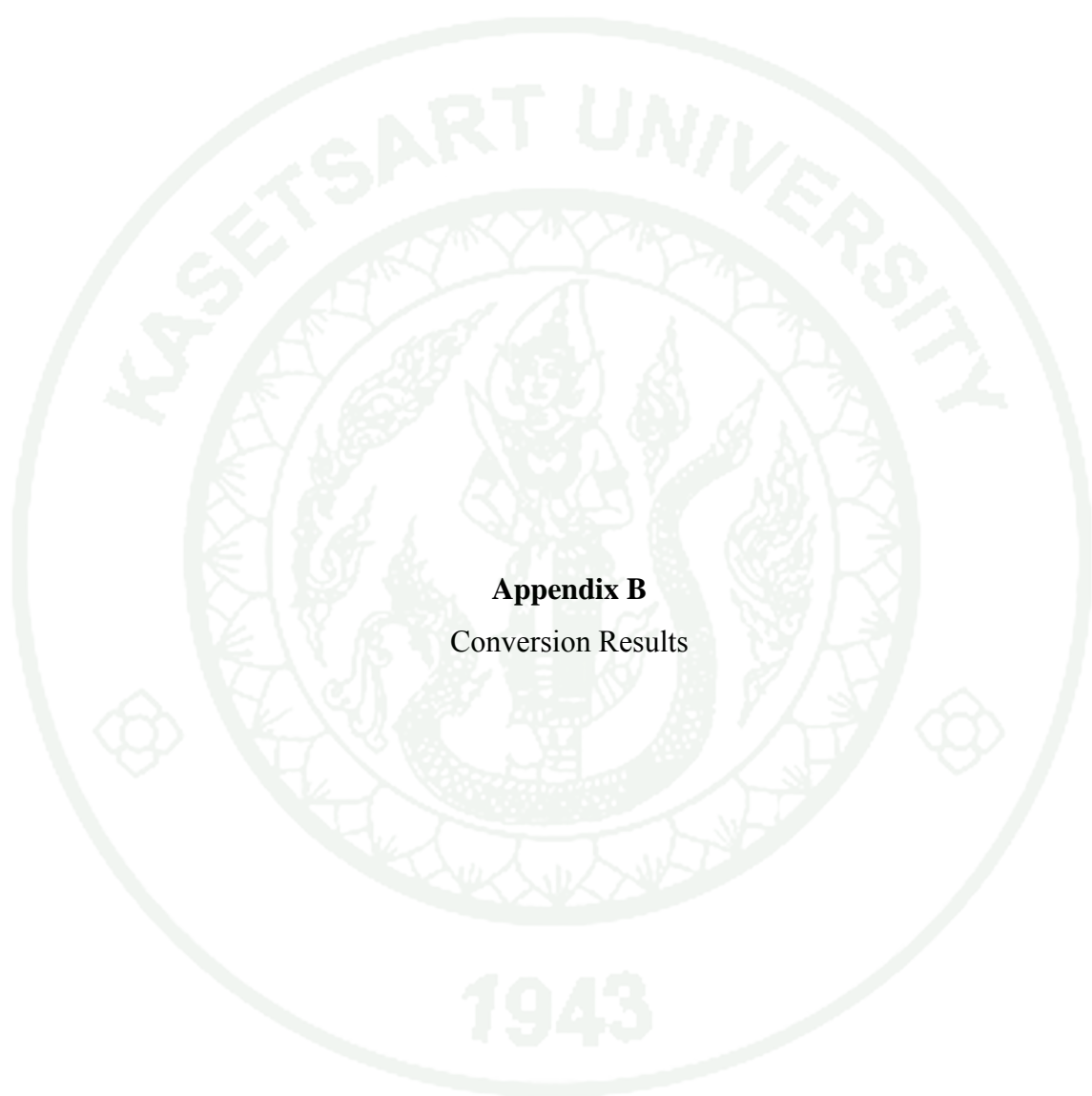
Substance	Equation	R <sup>2</sup>
H <sub>2</sub>	mol = 5.0 x 10 <sup>-12</sup> x area	0.993
CO	mol = 5.0 x 10 <sup>-11</sup> x area	0.999
CH <sub>4</sub>	mol = 2.0 x 10 <sup>-11</sup> x area	0.999
CO <sub>2</sub>	mol = 7.0 x 10 <sup>-11</sup> x area	0.999

The calculation for the amount of each component in a standard-gas mixture can be calculated as follows:

$$\text{Amount of component}_i \text{ (mol)} = \frac{V_i \times T}{100 \times 22,400} \quad (\text{A1})$$

where  $V_i$  = % volume of component<sub>i</sub> (cm<sup>3</sup>/cm<sup>3</sup>)

T = volume of standard gases mixture (mL)



**Appendix B**  
Conversion Results

### Conversion Results

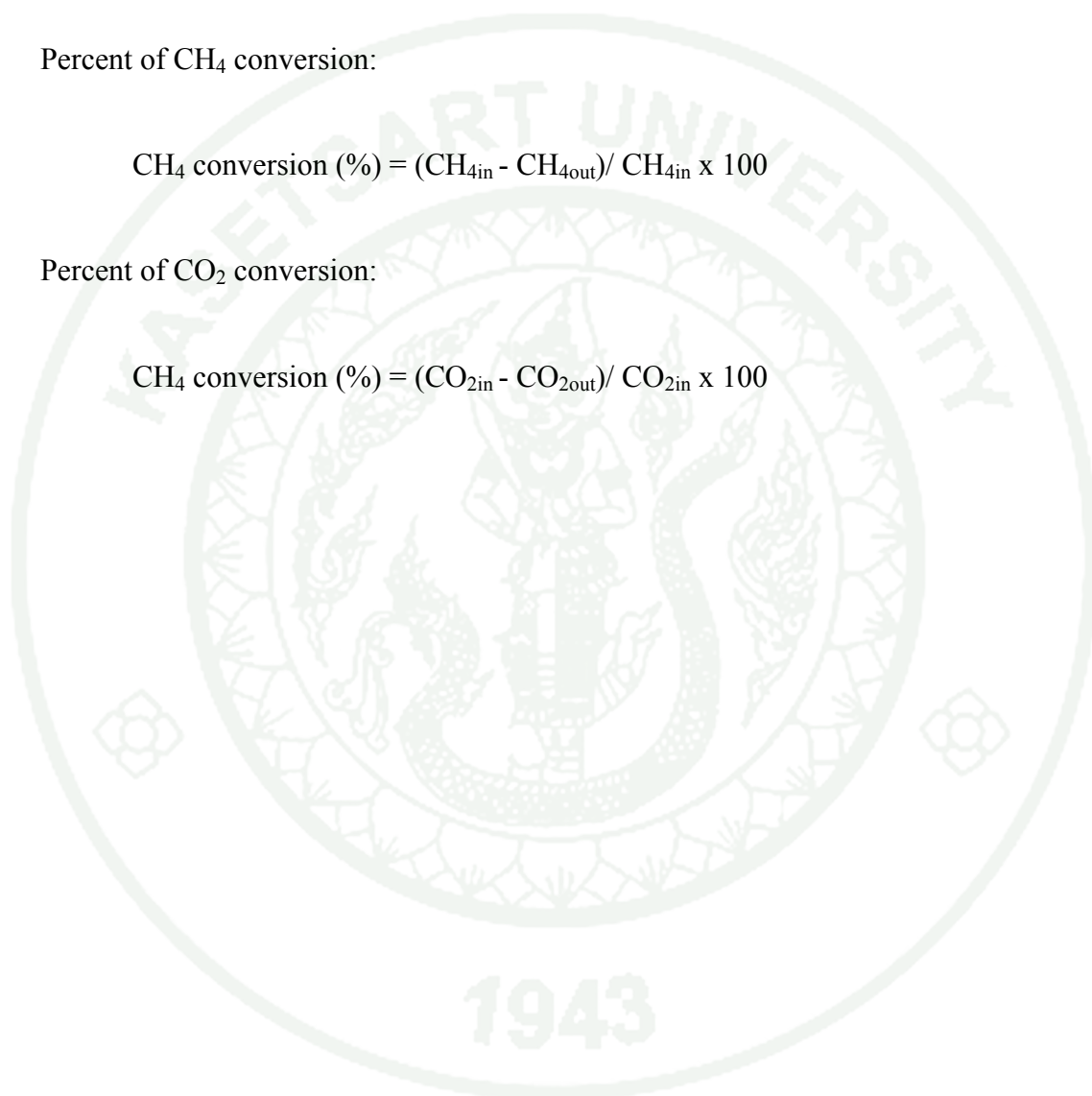
The calculation for the conversion of carbon dioxide and methane to hydrogen and carbon monoxide products in dry reforming reaction are shown as follows:

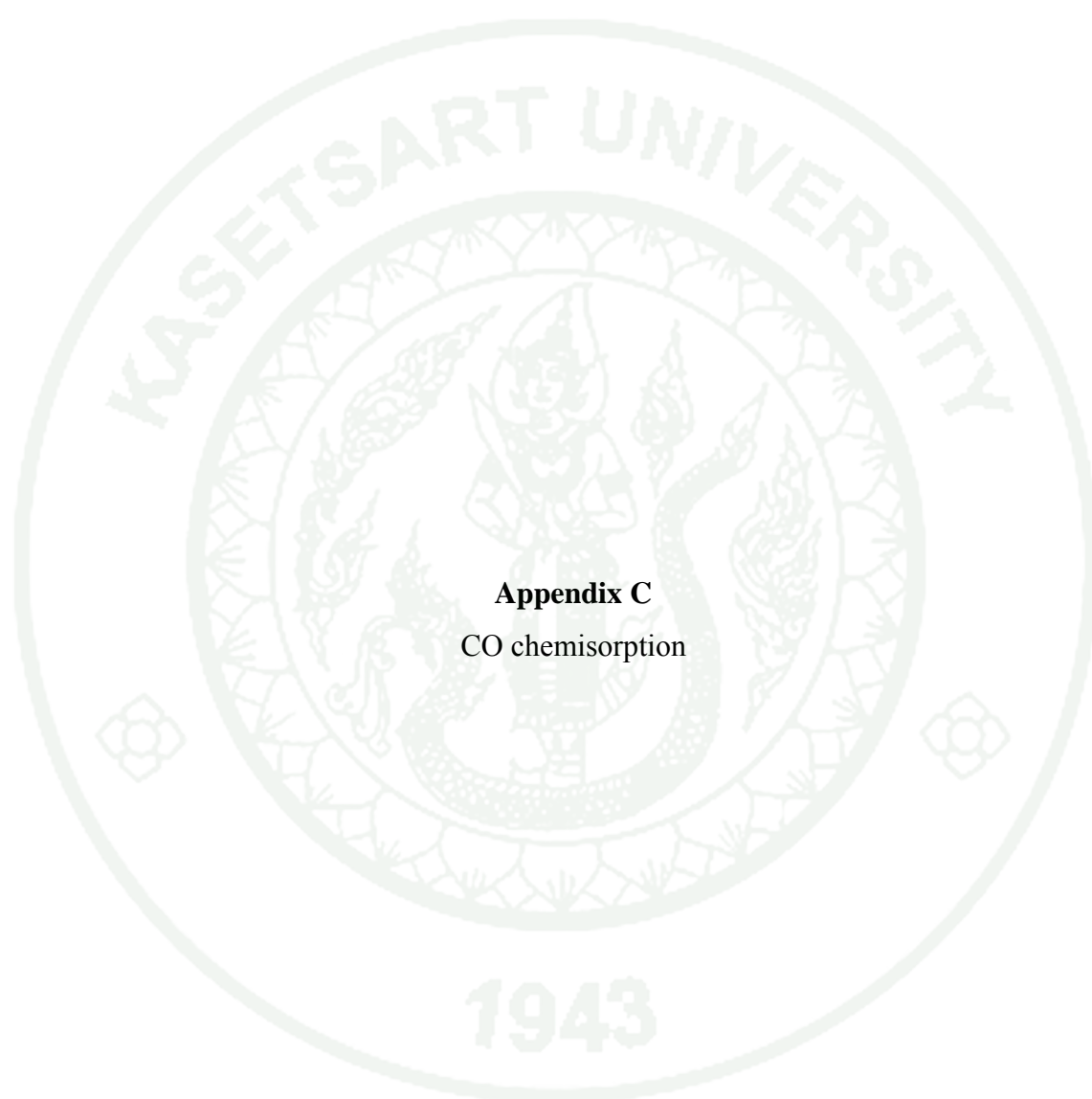
Percent of CH<sub>4</sub> conversion:

$$\text{CH}_4 \text{ conversion (\%)} = (\text{CH}_{4\text{in}} - \text{CH}_{4\text{out}}) / \text{CH}_{4\text{in}} \times 100$$

Percent of CO<sub>2</sub> conversion:

$$\text{CO}_2 \text{ conversion (\%)} = (\text{CO}_{2\text{in}} - \text{CO}_{2\text{out}}) / \text{CO}_{2\text{in}} \times 100$$

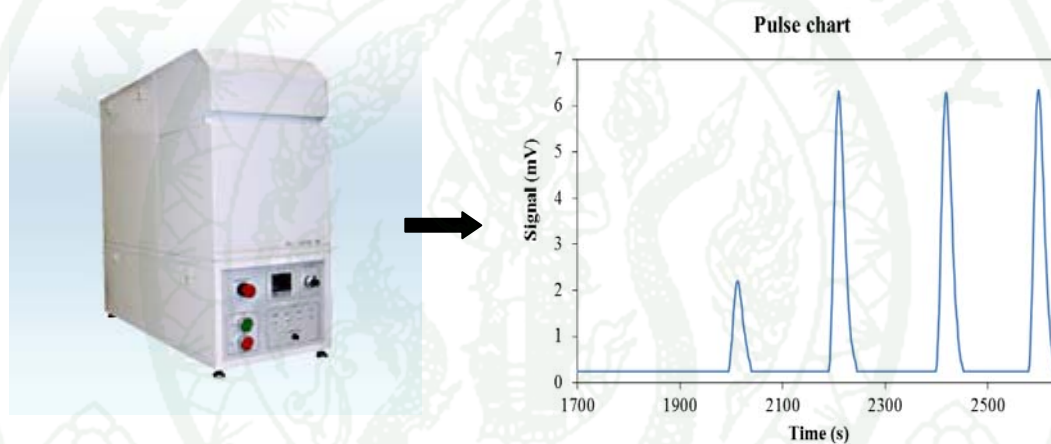




**Appendix C**  
CO chemisorption

### CO chemisorption

CO chemisorption was used to analyze the number of active nickel site by using BEL-METAL-1 equipment, as shown in Figure A3. For measurement method, catalyst was firstly reduced with hydrogen gas at 500°C for 1 h after that the feed gas was switched to helium gas and temperature was cooled down to 50°C. CO gas was pulsed under temperature of 50°C and the amount of CO adsorbed was analyzed by using thermal conductivity detector. For the active nickel calculation, the amount of CO adsorbed was evaluated by using the stoichiometric factor of CO and Ni of 2.



**Appendix Figure C1** CO chemisorption analysis by BEL-METAL-1 equipment.

## CIRRICULUM VITAE

**NAME:** Ms. Waleeporn Donphai

**DATE OF BIRTH:** May 20, 1986

**BIRTH PLACE:** Samutsakhon, Thailand

<b>EDUCATION:</b>	<b><u>YEAR</u></b>	<b><u>INSTITUTE</u></b>	<b><u>DEGREE</u></b>
	2008	Kasetsart Univ.	B.Eng. (Chemical Eng.) 1 <sup>st</sup> Class honor
	2014	Kasetsart Univ.	D.Eng. (Chemical Eng.)

**POSITION/TITLE** : -

**WORK PLACE** : Faculty of Engineering, Kasetsart University

**SCHOLARSHIP/ AWARDS** : Royal Golden Jubilee Ph.D. Scholarship  
from Thailand Research Fund (TRF)  
2009 – 2014

: The best presentation award of session  
from “the 3<sup>rd</sup> International Thai  
Chemical Engineering and Applied  
Chemistry Conference”, October, 2013

### International Publications

1. **W. Donphai**, K. Faungnawakij, M. Chareonpanich, J. Limtrakul, *Effect of Ni-CNTs/Mesocellular silica composite catalysts on carbon dioxide reforming of methane*, Appl. Catal., A. 475 (2014) 16.

2. T. Witoon, T. Permsirivanich, **W. Donphai**, A. Jaree, M. Chareonpanich, *CO<sub>2</sub> hydrogenation to methanol over Cu/ZnO nanocatalysts prepared via a chitosan-assisted co-precipitation method*, Fuel Process. Technol. 116 (2013) 72.

### **International Conferences**

1. **W. Donphai**, M. Chareonpanich, *Catalytic Performance of Ni/Carbon Nanotube-Mesoporous Silica Composites for Dry Reforming Reaction*. The 3<sup>rd</sup> Research Symposium on Petrochemical and Materials Technology & The 18<sup>th</sup> PPC Symposium on Petroleum, Petrochemicals and Polymer, Bangkok, Thailand, April 24, 2012,

2. **W. Donphai**, D. Yamahana, M. Chareonpanich, T. Kamegawa, H. Yamashita, *Enhanced Photocatalytic Performances of Graphene Coated TiO<sub>2</sub> Nanoparticles Loaded on Mesoporous Silica*, International Symposium on Zeolites and MicroPorous Crystals (ZMPC 2012), Hiroshima, Japan, July 28 – August 1, 2012.

3. **W. Donphai**, D. Yamahana, M. Chareonpanich, T. Kamegawa, H. Yamashita, *Photocatalytic Performance of Graphene Coated TiO<sub>2</sub> Nanoparticles on MCM-41 in the Degradation of 2-propanol*, 8<sup>th</sup> Handai Nanoscience and Nanotechnology International Symposium - Nanoscience and Nanotechnology for Energy Harvesting and Saving-, Osaka, Japan, December 10-11, 2012.

4. **W. Donphai**, M. Chareonpanich *Effect of Carbon Nanotubes Composite Catalyst on Dry Reforming Reaction*, The 3<sup>rd</sup> TIChE International Conference 2013, Khon Kaen, Thailand, October 17-18, 2013.